

Dynamics of the Antarctic ice sheet with
coupled ice shelves
南極氷床変動における棚氷の影響

Tatsuru Sato

PhD Dissertation

Division of Earth System Science
Graduate School of Environmental Science
Hokkaido University

May 15, 2012

Contents

Abstract	iii
Acknowledgements	v
1 Introduction	1
1.1 The Antarctic ice sheet	1
1.2 Ice shelves	2
1.3 Global temperature and sea level change	4
1.4 Changes in the Antarctic ice sheet and ice shelves	6
1.5 Ice sheet model SICOPOLIS	8
1.6 Purpose and tasks of the study	9
2 Theory	24
2.1 Dynamics of large ice bodies	24
2.2 Constitutive equations	24
2.3 Stress balance equations in general coordinates	26
2.4 Large-scale ice sheet dynamics	28
2.5 Hydrostatic approximation	28
2.6 Shallow shelf approximation	31
2.6.1 Formulation in orthogonal curvilinear coordinates	31
2.6.2 Boundary conditions at the ice surface	31
2.6.3 Boundary conditions at the ice base	32
2.6.4 Vertical integration	32
2.7 Shallow ice approximation	35
2.8 Temperature evolution of ice	36
2.9 Boundary conditions	36
2.9.1 Basal sliding	36
2.9.2 Calving front	37
2.9.3 Surface temperature and mass balance	38
2.9.4 Basal temperature and sub-marine mass balance	39
2.10 Topographic evolution	39

2.10.1	Ice thickness equation	39
2.10.2	Ice surface equation	40
3	Numerical methods	46
3.1	Ice sheet model SICOPOLIS	46
3.2	Details of the numerical grid	46
3.3	Coupling of the ice shelf model to the ice sheet model	48
3.4	Shallow shelf dynamic equations	48
3.4.1	Field equations	48
3.4.2	Calving front conditions	49
3.4.3	Grounding zone	50
3.5	Temperature evolution	52
3.6	Topography evolution	52
3.6.1	Ice surface equation	52
3.6.2	Ice thickness equation	53
4	Numerical tests	57
4.1	Ice shelf ramp	57
4.2	Shelfy stream experiments	58
5	SeaRISE experiments	63
5.1	SeaRISE	63
5.2	Application of the model to the SeaRISE set-up	63
5.3	Paleoclimatic spin-up	64
5.4	Sensitivities of the ice volume to different datasets	65
5.5	Future climate experiments	66
5.6	Sensitivities on varied sub-ice-shelf melting rates	67
5.7	Results of whole set of SeaRISE experiments	69
5.8	Relaxation of the initial shock	70
6	Discussion	90
6.1	Comparison to the present-day ice sheet	90
6.2	The dynamics of ice sheet and ice shelves	91
6.3	Grounding line migration	92
6.4	Calving	94
7	Summary	101
	Bibliography	103

Abstract

Antarctica is Earth's southernmost continent, situated almost entirely south of the Antarctic Circle. Except for some coastal regions and high mountains, most of the continent is covered by ice that constitutes the Antarctic ice sheet. The Antarctic ice sheet is the largest land ice mass on the present-day Earth. According to the Fourth Assessment Report of the United Nations Intergovernmental Panel on Climate Change (IPCC AR4), the total volume of the ice sheet amounts to approximately $25 \times 10^6 \text{ km}^3$ or 56.6 m SLE (meters of sea level equivalent).

Ice shelves are floating ice bodies that are attached to the margins of an ice sheet. Half of the coastline of the whole Antarctic ice sheet and almost the entire West Antarctic ice sheet are surrounded by ice shelves. Most of the ice flow towards the coast is discharged through them. Recent observations have led to strong concerns that ice-dynamical processes (loss of buttressing from ice shelves, speed-up of ice streams and outlet glaciers) may boost the mass loss and thus lead to an additional contribution to sea level rise. The importance of understanding these processes to assess future sea level change was explicitly recognized in the IPCC AR4.

SICOPOLIS is a dynamic/thermodynamic ice sheet model which has been applied to large ice sheets such as the Greenland, Antarctic, Laurentide and Fennoscandian ice sheets. Although it was applied to the Antarctic ice sheet, special treatment of ice shelf dynamics has not been included so far. In this study, ice shelf dynamics is considered and coupled with the ice sheet model. The model is applied to the Antarctic ice sheet to study instabilities of the ice sheet related to ice sheet/ice shelf interactions.

Shallow shelf approximation is applied for the ice shelf model. The performance of the model is tested by using an analytical solution for a two-dimensional ice shelf ramp. The result shows that the model can reproduce the analytical solution with high accuracy. The ice shelf model is then coupled to the ice sheet model SICOPOLIS and applied to the Antarctic ice sheet. Input data are adopted from the SeaRISE project, an international community effort to estimate the contribution of ice sheets to future sea level

rise in the next 100s of years. In order to obtain a suitable present-day configuration of the Antarctic ice sheet, it is desirable to carry out a paleoclimatic spin-up over at least a full glacial cycle until the present. The paleoclimatic spin-up is conducted with a fixed-topography approach (the geometry is kept fixed over time, thus not allowed to evolve), while the model is forced by past temperature and accumulation changes estimated by proxies from the Vostok ice core record.

Future climate experiments over 500 years are conducted by using the result of the paleoclimatic spin-up as initial condition. Three types of sensitivity experiments (surface climate, sub-ice-shelf melt rate and basal sliding) are conducted to investigate the key elements for the evolution of the Antarctic ice sheet in a warming climate. Results show that the grounded ice sheet volume reacts most strongly to changes in sub-ice-shelf melt rates. It also decreases with increased basal sliding, although the range is not as large as for sub-ice-shelf melt. The smallest influence is that of direct climate forcing by surface temperature and precipitation. Combination of all the components causes the largest decrease of the ice sheet. The range of grounded ice volume change across all experiments is \sim 1.3 m SLE after 100 years and \sim 3.3 m SLE after 500 years. These results show that the contribution of changes of the Antarctic ice sheet to global sea level during the next 100 years can be larger than projected by the IPCC AR4.

Acknowledgements

I would like to express my gratitude to my supervisor Ralf Greve who supported my study during the doctor course. I also thank Takeo Hondoh, Takayuki Shiraiwa, Shin Sugiyama and Yoshinori Iizuka, who helped me not only during the doctor course, but also during the previous master course. Nina Kirchner and her colleagues supported me during my visit at Stockholm University. Hakime Seddik helped me to use the Linux server in the laboratory. I thank Thorben Dunse and Fuyuki Saito for many fruitful discussions. Thomas Gölles helped me to correct the thesis. I appreciate David Holland's invitation to the NYU Abu Dhabi workshop in March 2012. I would like to thank the students and former students in our group: Toshimitsu Sakurai, Shun Tsutaki, Daisuke Nishimura, Akira Tsuchimoto, Takehiro Fukuda, Takeshi Yoshizawa, Kenta Tone, Ikumi Oyabu, Daiki Sakakibara, Mikako Nakata, Ayaka Okamoto, Satoshi Matsuno and Masahiro Minowa. Language editing was done by Andrew Davis of English Experience Language Services (Jena, Germany). Ayako Abe, Keiichiro Ohshima and Takayuki Shiraiwa kindly agreed to be examiners. Finally, I owe a big thanks to my family.

This study was supported by a Grant-in-Aid for Scientific Research A (No. 22244058) from the Japan Society for the Promotion of Science JSPS, and by an exchange grant for a research visit from the Scandinavia-Japan Sasakawa Foundation.

Chapter 1

Introduction

1.1 The Antarctic ice sheet

Antarctica is a continent lying in the Antarctic region. The climate is very cold throughout the region; mean annual temperature is lower than the melting point of ice [Comiso, 2000]. Most of the continent is covered by ice, except for some coastal regions and high mountains. This ice covering is called the Antarctic ice sheet (Fig. 1.1).

The Antarctic ice sheet is by far the largest land ice mass on Earth. The total area of the ice sheet is $12.3 \times 10^6 \text{ km}^2$. Its total ice volume is $24.7 \times 10^6 \text{ km}^3$ [Solomon et al., 2007] and it contains about 90% of the ice and 70% of the fresh water on Earth. It is approximately 56.6 m SLE (meters of sea level equivalent), i.e., it would produce a sea level rise of about 55 m if it melted completely. Ice shelves are among the components of the ice sheet.

The Antarctic ice sheet is divided into two regions by the Transantarctic Mountains (Fig. 1.1). One is the East Antarctic ice sheet (EAIS). Most of the EAIS is located east of the Greenwich meridian. The other is the West Antarctic ice sheet (WAIS). Most of the WAIS is located west of the Greenwich meridian. The EAIS is larger in area than the WAIS. The ice there is also thicker and has a greater mass than that of the WAIS. Despite its considerable thickness, the base of the EAIS lies mostly above sea level. Many ice cores are drilled in the EAIS since it contains old ice, particularly in inland regions.

Since most of the WAIS lies on bedrock below sea level, it is called a marine ice sheet. The bed lies sufficiently below sea level for ice shelves to be formed often around the margins (Fig. 1.2). This condition may make the WAIS more unstable than the EAIS, because a small retreat of its margins can destabilize most of the WAIS. This then leads to rapid disintegration of

large regions of ice.

The mass balance of the ice sheet is driven by accumulation and ice flow. The Antarctic ice sheet is considered a desert in terms of accumulation rates. The annual accumulation rate is hundreds of millimeters along the coast and tens of millimeters around the dome. Although accumulation rates are low, the low velocity of the inland ice maintains its large volume.

Although the surface is cold, the base of the ice sheet is relatively warm and melts in some regions due to geothermal heat and strain heating of ice. Such melt water lubricates the ice sheet and allows basal sliding. This process produces fast flowing channels in the ice sheet called ice streams. They are the key component of the Antarctic ice sheet's ice mass transport. Although outlet glaciers and ice streams comprise only 13 of the Antarctic ice sheet margins, they may drain as much as 90% of the accumulation in the interior [Morgan et al., 1982].

1.2 Ice shelves

The thickness of the ice sheet declines towards the coast. Where it becomes thin enough, it starts floating because the density of ice is less than that of sea water. Ice shelves are thus formed. There are large areas of such floating ice attached to glaciers or to the ice sheet (Fig. 1.3). The boundary between the floating ice shelf and grounded ice, where the ice starts floating, is called the grounding line or grounding zone. Ice is lost from the ice shelf to the ocean by melting under the shelf and iceberg calving at the front of the ice shelf. The boundary of the ice shelf and the ocean is called the calving front.

Ice shelves surround much of Antarctica. They are also formed in the Arctic in some fjords and bays on the Greenland and Ellesmere Island coasts. Alpine glaciers which terminate in a fjord can have a floating tongue which is similar to an ice shelf. A total of 44% of the Antarctic coastline has ice shelves attached. The total area is $1.5 \times 10^6 \text{ km}^2$ [Solomon et al., 2007]. Most of the WAIS is surrounded by ice shelves [Cuffey and Paterson, 2010]. Through these shelves 80% of the ice flow discharges towards the coastline.

The Ross Ice Shelf is the largest shelf with an area of 472,960 km^2 , which is larger than Japan (377,944 km^2) and twice the area of Honshu island. The shelf is about 800 km across. Its thickness varies from over 1000 m around the grounding line to about 250 m at the calving front. Typical velocities are a few hundred meters per year, increasing to more than 1 km/a at the front [Rignot et al., 2011a].

The second largest is the Ronne-Filchner ice shelf. Its area is 422,420 km^2 , which is almost as large as the Ross ice shelf.

Other large ice shelves are Amery ($62,620 \text{ km}^2$), Larsen C ($48,600 \text{ km}^2$), Riiser-Larsen ($48,180 \text{ km}^2$), Fimbul ($41,060 \text{ km}^2$) and Shackleton ($33,820 \text{ km}^2$) (see Fig. 1.1). Most of the large ice shelves are located in West Antarctica.

Ice shelves are nourished by ice flow from the ice sheet, snow accumulating on their surface, and ice accumulating on their base as sea water freezes there. There is typically an input velocity of hundreds of metres per year at the grounding region. It can be several thousand meters per year at the calving front [Doake, 2001].

Shelves lose mass through ablation processes, iceberg calving and melting at the base. The basal mass balance is controlled by the circulation of the sea below the ice shelf. The melt rate is often high near both the grounding line and the ice front [Joughin and Padman, 2003]. Sea water sometimes freezes in the central part and this is called marine ice. Grounding over an appreciable area produces a dome-shaped ice rise with its own radial flow pattern. Less extensive grounding results in surface irregularities called ice ripples, which move with the shelf.

The essential characteristics of an ice shelf are the dynamics of the ice body, grounding line dynamics, calving, and basal mass balance. Basal friction does not act on floating ice as it does on grounded ice due to the fairly low dynamic friction at the ice-water boundary. The flow of grounded ice sheets is dominated by vertical shear stresses, while ice shelf flow is dominated by longitudinal stretching and lateral shearing. An ice shelf behaves like a large membrane which spreads by horizontal stretching, while vertical shearing is unimportant [Schoof, 2007b]. Calving and the basal mass balance are important processes for the overall mass balance of the ice sheet because they control the mass loss.

The grounding line divides the dynamics of the ice shelves from those of the grounded ice. Grounding line dynamics affect the evolution of both. The horizontal extent of the transition zone is the distance over which longitudinal stresses from the ice shelf propagate into the ice sheet. A slight retreat in the grounding line position will lead to an increase in ice thickness and hence ice discharge at the grounding line. This represents a positive feedback as an increase in ice discharge leads to further shrinkage of the ice sheet and hence grounding line retreat. This then leads to a further increase in ice discharge.

The back force (the buttressing effect) is the total force transmitted upstream by forces, other than the pressure of sea water at the ice front, that oppose the spreading of the ice shelf. The drag exerted by the side walls and ice rise are examples of such forces.

The collapse of the Larsen ice shelves has been an impressive phenomenon of recent years. On the Antarctic Peninsula, ice shelves have lost $\sim 300 \text{ km}^2$ in a year. Larsen A ice shelf ($1,600 \text{ km}^2$) broke away in 1995 and Larsen B

ice shelf ($3,500 \text{ km}^2$) in 2002. Such collapses may occur in other areas under future global warming conditions.

By using geological proxy data, Scherer et al. [1998] conjectured that the upstream part of the Ross Ice Shelf collapsed at least once in the Pleistocene. The collapse could have occurred during past interglacial periods. Thus, ice shelf dynamics has probably played an important role in ice sheet evolution during glacial-interglacial cycles.

1.3 Global temperature and sea level change

It is a major topic of discussion that the Earth's surface climate is changing. One cause of change is considered to be human activities, such as burning fossil fuels and land management practices leading to as deforestation. The effects have become evident in recent decades. In consequence, people have started to recognize the importance of scientific and social studies related to this environmental problem.

The Intergovernmental Panel on Climate Change (IPCC) is the leading international community for the assessment of climate change. It was established by the United Nations Environment Programme (UNEP) with the World Meteorological Organization (WMO) to provide the world with a clear scientific view of the current state of knowledge on climate change and its potential environmental and socio-economic impacts.

Researchers have made progress in understanding the climate change mechanism in space and in time through improvements and extensions of numerous datasets and data analyses (Fig. 1.4). Increasingly comprehensive observations are available for glaciers and snow cover going back to the 1960s, and for sea level and ice sheets over about the last 10 years, although data coverage is still limited. The IPCC AR4 (fourth assessment report) shows unequivocally that the climate has warmed over the last 100 years and is still warming. Observations show an increase in global average air and ocean temperatures, widespread melting of snow and ice, and rising mean sea level [Solomon et al., 2007].

Future climate change can also be estimated by climate model results. Many scenarios are considered when estimating the likely range of future warming. The important consequence is that global warming is inevitable even if the concentrations of all greenhouse gases and aerosols are kept constant at the levels of 2000 (Fig. 1.5). It is predicted that a further warming of about 0.1°C per decade is to be expected even this stabilization is achieved. The following scenarios have been considered:

- A1: characterized by rapid economic growth. Global population reaches

9 billion in 2050 and then gradually declines. International interactions are extensive. There are several types of experiments; A1F1 emphasizes fossil fuels, A1B has a balanced emphasis on all energy sources, and in A1T non-fossil energy sources dominate.

- A2: inter-regional interactions are limited and regions are self-reliant. Population increases continuously.
- B1: the world is more integrated and more ecologically friendly. Economic growth and population trends are the same as in A1.
- B2: the world is more divided than in A2, but more ecologically friendly than in B1. The population increases continuously but more slowly than in A2.

There are variations between experiments but all scenarios show an upward trend. Six scenarios have been used to estimate the global average sea level rise by the end of the 21st century (Fig. 1.6). Thermal expansion contributes 70-75% to the best estimate for each scenario. Glacier and ice sheet melting account for the rest.

In some parts of West Antarctica, large accelerations of ice flow have recently occurred which may have been caused by thinning of ice shelves due to ocean warming. The limited understanding of such processes was explicitly spelled out in IPCC AR4: “Dynamical processes related to ice flow not included in current models but suggested by recent observations could increase the vulnerability of the ice sheets to warming, increasing future sea level rise. Understanding of these processes is limited and there is no consensus on their magnitude.”

Although this has not been formally attributed to anthropogenic climate change due to greenhouse gases, it suggests that future warming could cause faster mass loss and greater sea level rise. Quantitative projections of this effect cannot be made with confidence. If recently observed increases in ice discharge rates from the Greenland and Antarctic Ice Sheets were to increase linearly with global average temperature change, they would add 0.1 to 0.2 m to the upper bound of sea level rise. Understanding of these effects is, as yet, too limited to assess their likelihood or to give a good estimate.

1.4 Changes in the Antarctic ice sheet and ice shelves

The typical scales of the ice sheet are

$$\begin{aligned}\text{typical horizontal extent } [L] &= 1000 \text{ km;} \\ \text{typical horizontal velocity } [U] &= 10 - 100 \text{ m/a;} \\ \text{typical time scale } [t] = [L]/[U] &= 10^4 - 10^5 \text{ a.}\end{aligned}\quad (1.1)$$

Since the time scale of an ice sheet is quite long, it has long hysteresis and changes slowly. Ice cores drilled at Dome C and Dome Fuji in the EAIS show eight glacial cycles [Augustin et al., 2004, Goto-Azuma, 2008]. The temperatures of past environments can be determined from measurements on ice cores taken from boreholes. These measurements suggest that the Antarctic ice sheets have not changed significantly in 100-1000 years. However, this view is now changing.

The mass balance of Antarctica and its changes have only recently become known. The observational record of Antarctic glaciers is short and limited because humans have seldom visited Antarctic glaciers. But the advent of satellite missions has recently revolutionized our knowledge of ice dynamics in Antarctica (Fig. 1.7). The observations suggest the current mass balance of the ice sheet is most likely negative, with an accelerating trend [Rignot et al., 2011b] (Fig. 1.8). Owing to the very low surface temperatures, the ice sheet is not very susceptible to surface melting even under moderate global warming scenarios. However, recent observations have led to strong concerns that dynamic ice processes (loss of buttressing from ice shelves, speed-up of ice streams and outlet glaciers) may boost mass loss and thus make an additional contribution to sea level rise.

Recent observations [e.g., Joughin et al., 2003] have led to strong concern about ice-dynamic processes. One of the most impressive phenomena affecting ice shelves in recent years is the collapse of the Larsen ice shelves. Very small changes in the ice shelves can have large effects on regions of ice upstream.

Ice shelves are among the most active parts of the ice sheet system. They interact with the inland ice sheet, glaciers and ice streams which flow into them, and with the sea into which they eventually melt, either directly or as icebergs. The typical timescale of an ice shelf is shorter than that of an ice

sheet:

$$\begin{aligned} \text{typical horizontal extent } [L] &= 100 \text{ km;} \\ \text{typical horizontal velocity } [U] &= 100 - 1000 \text{ m/a;} \\ \text{typical time scale } [t] = [L]/[U] &= 100 - 1000 \text{ a.} \end{aligned} \quad (1.2)$$

Ice shelves therefore change more rapidly than ice sheets and they also affect the upstream inland ice.

Rignot [2006] summarized the effect of dynamic changes in ice sheet margins. The surface velocity of glaciers around the Larsen ice shelf has changed considerably (Fig. 1.9). The glaciers have accelerated markedly and left bits of glacier ice hanging on cliff walls 40 m above the new glacier surface after the collapse of Larsen A in 1995 [De Angelis and Skvarca, 2003]. Drygalski Glacier flowed three times faster in 2000 than before the collapse [Rott et al., 2002]. Glacier acceleration continued for more than 10 years after the removal of the ice shelf [Rignot, 2006]. Following the collapse of the Larsen B ice shelf, Hektoria/Green/Evans flowed eight times as fast, and Crane and Jorum twice as fast as they had done before [Scambos et al., 2004].

Pine Island Glacier (Fig. 1.10) is an important drainage of the West Antarctic ice sheet. Its grounding line is retreating rapidly, at 1000 m/a. The ice shelf below the Pine Island glacier has the highest rates of bottom melting in Antarctica. These are are 58 ± 8 m/a near the grounding line and 24 ± 4 m/a on average for the whole ice shelf [Rignot, 2006]. This is two orders of magnitude greater than the melting underneath the Ross and Ronne ice shelves. This suggests that thermal forcing from the ocean has a great influence on the ice shelf mass budget [Jenkins et al., 1997]. Interaction between oceans and ice shelf is therefore considered to be the cause of grounding line retreat. The glacier is accelerating and this acceleration is sufficient to explain the observed thinning [Rignot et al., 2002]. The estimated velocity field and changes from the 1970s to the present are shown in Fig. 1.11. Glacier velocity increased 38% from 1974-2005. The acceleration is detected not only at the grounding line but also more than 100 km upstream. Changes of flow in ice shelves and ice streams were also found in East Antarctica. All ice sheet margins have been changing their flow in recent decades.

The transition zone between grounded and floating ice divides the ice shelf and the ice sheet. In most cases, ice streams are formed beneath ice shelves and flow into them. The discontinuity between the dynamics of the ice sheet and those of the ice shelf in ice sheet models causes a problem in representing its dynamics [Pattyn et al., 2006]. A suitable treatment of the transition zone is important for the dynamics of the coupled system, and for

marine ice sheet dynamics in particular [Weertman, 1994, Schoof, 2007a].

The boundary layer theory [Schoof, 2007a] is applied to the grounding zone for discussing the role of grounding line dynamics in marine ice sheet evolution. The boundary layer theory states that ice flux through the grounding line in a two-dimensional sheet-shelf system increases sharply with ice thickness at the grounding line. This result is then applied to the large-scale dynamics of a marine ice sheet.

The results are that steady grounding lines cannot be stable on reverse bed slopes [Vieli and Payne, 2005]. They can also undergo hysteresis when material parameters (such as ice viscosity or basal sliding) or external forcing (accumulation or sea level) vary. The hysteresis mechanism, which is a unique characteristic of the marine ice sheet, is driven by outflow of ice through the grounding line and requires overdeepening. It is also suggested that this behaviour can, in principle explain the retreat of the WAIS following the last glacial maximum, and may play a role in the dynamics of Heinrich events [Schoof, 2007a], which are the quasi-periodic episodes of massive ice discharge from the Laurentide ice sheet [Heinrich, 1988].

1.5 Ice sheet model SICOPOLIS

Ice sheet models use quantitative methods to simulate the evolution, dynamics and thermodynamics of ice sheets. The gravity-driven activity of ice sheets is controlled by two main variables: the strength of the ice sheet base and the temperature. Glacier flow is controlled by internal deformation of ice and by basal sliding. In an ice sheet model, the momentum balance is calculated to estimate velocities of ice with continuum mechanics. Ice sheet evolution is simulated using calculated velocities and the mass balance at boundaries. Jenssen [1977] constructed a three-dimensional ice sheet model and applied it to the Greenland ice sheet (Fig. 1.12). The glacial-interglacial evolution of the Antarctic ice sheet with coupled ice shelves was simulated by [Huybrechts, 1990]. Some ice sheet models have been constructed more recently [e.g., Payne, 1999, Ritz et al., 2001, Saito et al., 2003, Bueler and Brown, 2009]. Pollard and DeConto [2009] simulated five million years of evolution of the ice sheet. Although most ice sheet models use the finite difference method due to its computational efficiency, some ice sheet models use the finite element method [Seddik et al., 2012, Larour et al., 2012]. Such finite element models use higher order (less approximation) or full stokes field equations. However, it takes a lot of computational effort to compute the entire ice sheet in higher order dynamics.

SICOPOLIS (<http://sicopolis.greveweb.net/>) is a three-dimensional dy-

namic/thermodynamic ice sheet model. It can be used to simulate the evolution of large ice sheets. It was originally created as part of the doctoral thesis of Greve [1995] in a version for the Greenland Ice Sheet. The model solves the thermomechanically coupled field equations: the equations of mass, momentum and energy, along with the constitutive equation, Glen's flow law. Boundary conditions for the free surface and the bed are also included. Isostatic displacement of the bed due to ice loss is also calculated for an ice sheet. It includes a detailed treatment of basal temperate layers. Within the temperate layers, water content is calculated, and its influence on the ice viscosity is taken into account [Greve, 1997b]. The model has been applied to large ice sheets such as the Greenland, Antarctic, Laurentide and Fennoscandian ice sheets [Greve, 1997a, Forsström and Greve, 2004] (Fig. 1.13).

Greve [1997a] applied the model to the Greenland ice sheet. This model was applied here to obtain the steady state under present climate conditions with different parameters. Transient simulations were also conducted. Past glacial experiment and future climate runs were carried out.

Calov et al. [1998] applied the model to the Antarctic ice sheet. The results are presented of a transient paleoclimatic simulation which covers two entire glacial and interglacial cycles, with special emphasis on Dronning Maud Land, to study ice coring regions and proposed possible drilling sites by using depth-age relationships derived from the model. Although it has been applied to the Antarctic ice sheet, special treatment of ice shelf dynamics has not yet been included.

1.6 Purpose and tasks of the study

To study Antarctic ice sheet dynamics and their changes, a model of ice shelf dynamics was constructed and coupled to the ice sheet model SICOPOLIS. Ice shelf dynamics are considered and coupled with the ice sheet model.

First, an ice shelf model was made without the coupled ice sheet model. The model's performance was then checked. It was then coupled to the ice sheet model. Not only differences in the dynamics, but also differences of flow regimes and stresses working in the ice shelves cause differences in heat flow and ice thickness evolution. Future evolution of the ice sheet was estimated using contributions from this project and newly-derived ice sheet data. Sea-level Response to Ice Sheet Evolution (SeaRISE) is a community-organized effort to estimate the upper bound of ice sheet contributions to sea level over the next few centuries. The coupled model is applied to the Antarctic ice sheet using the forcings given by the project.

As stated before, the ice sheet has changed significantly during glacial-

interglacial climate cycles. Modeling the paleo-ice sheet allows comparison of past and present ice sheet conditions. Paleoclimatic records such as ice core records help in understanding past ice sheet and climatic conditions. Past ice sheet evolution was simulated using information gained from such paleoclimatic records. How the Antarctic ice sheet will change in the future is an important question relating to future global warming. The mass balance of Antarctica and its changes are not very clear even today. One reason for this is the uncertainty arising from ice shelf dynamics. The effects of the Antarctic ice sheet was studied in cooperation with SeaRISE.

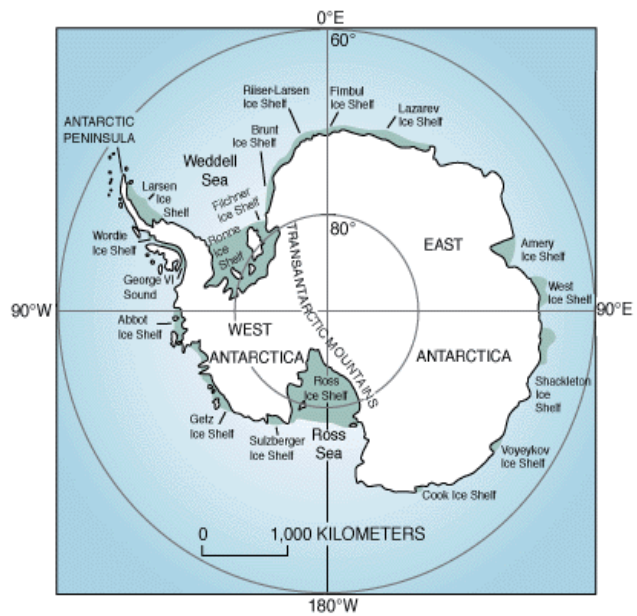


Figure 1.1: A map of the Antarctic ice sheet with ice shelves [Williams et al., 2005].

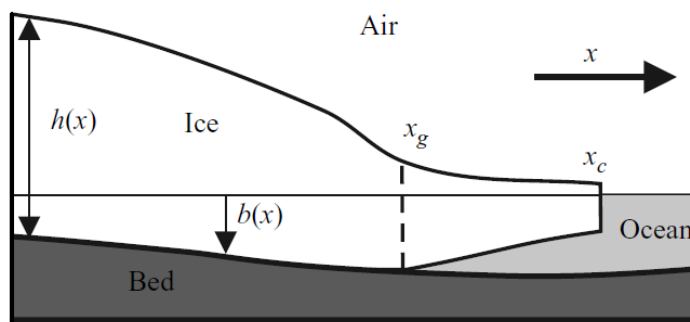


Figure 1.2: Typical conditions of the marine ice sheet with ice shelves (modified from Schoof [2007b]). The horizontal arrow is the direction of ice flow. x_g is the grounding line and x_c is the calving front. Although ice thickness $h(x)$ is greater than floating shelves, ice base elevation $b(x)$ is still lower than sea level.

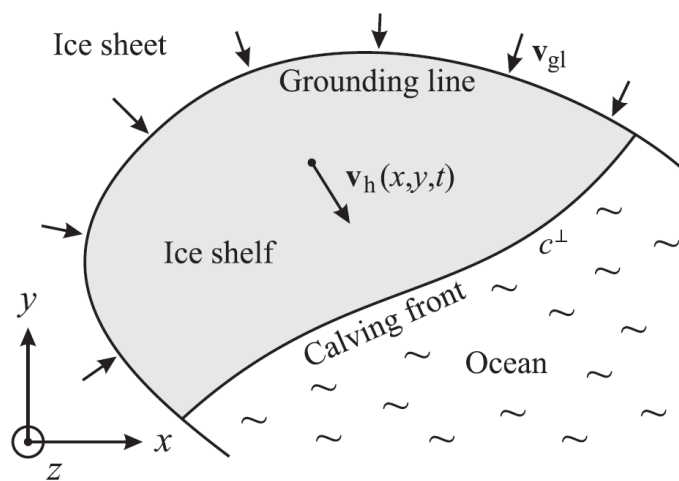


Figure 1.3: Ice shelf geometry in the horizontal map plane [Greve and Blatter, 2009]. Incoming flow comes from the upstream ice sheet. The boundary of the ice shelf and ice sheet is the grounding line. Iceberg calving occurs in front of the ice shelf then ice disperses in the sea. The boundary of the ice shelf and the sea is the calving front.

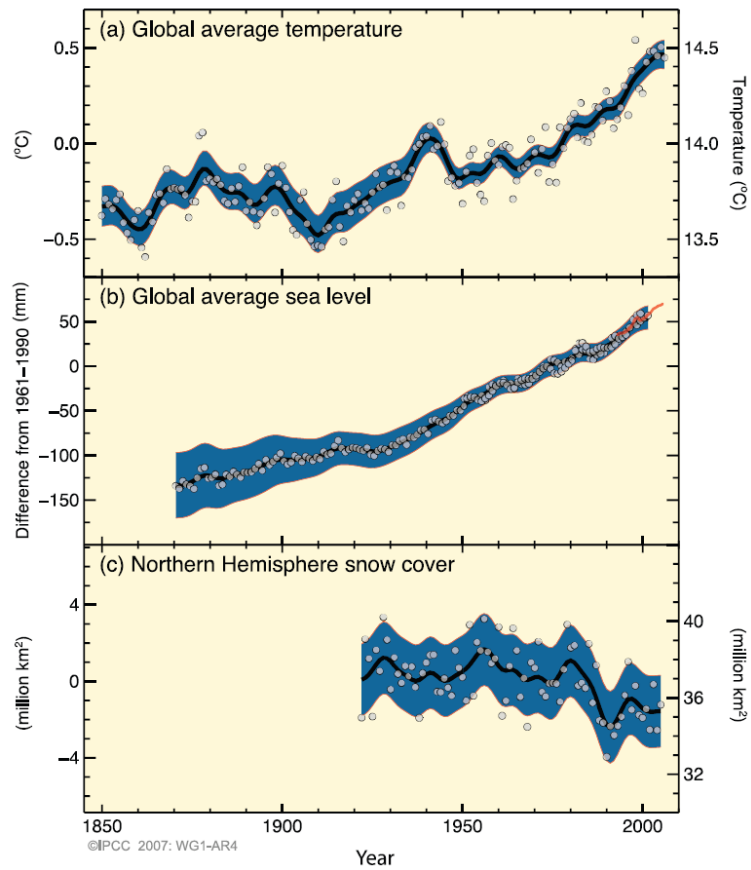


Figure 1.4: Observed changes for March-April in (a) global average surface temperature, (b) global average sea level from tide gauge (blue) and satellite (red) data and (c) Northern Hemisphere snow cover for [Solomon et al., 2007]. All these changes are relative to the corresponding averages for the period 1961-1990. Smoothed curves represent decadal average values. White circles show yearly values. The shaded areas are the uncertainty intervals estimated from a comprehensive analysis of known uncertainties (a and b) and from the time series (c).

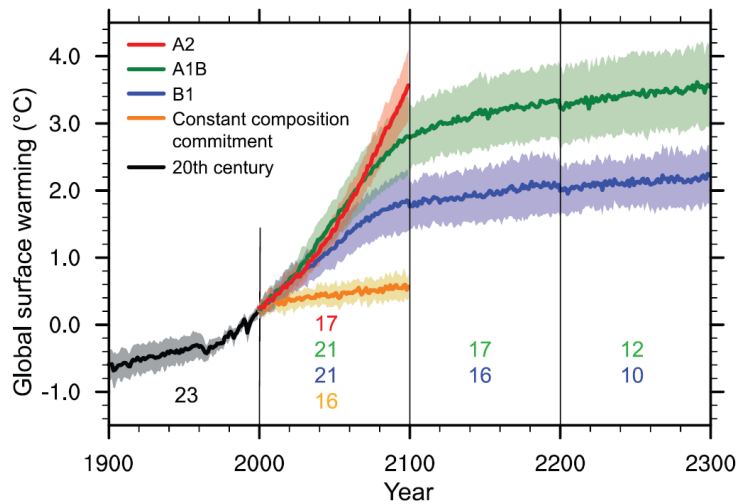


Figure 1.5: Multi-model means of surface warming (compared to the 1980–1999 base period) for each of the scenarios A2 (red), A1B (green) and B1 (blue), shown as continuations of the 20th-century simulation [Solomon et al., 2007]. The A1B and B1 scenarios are continued beyond the year 2100 with forcing kept constant. An additional experiment, in which the forcing is kept at the 2000 level is also shown (orange). Shading means $\pm 1\sigma$ of the multi-model means.

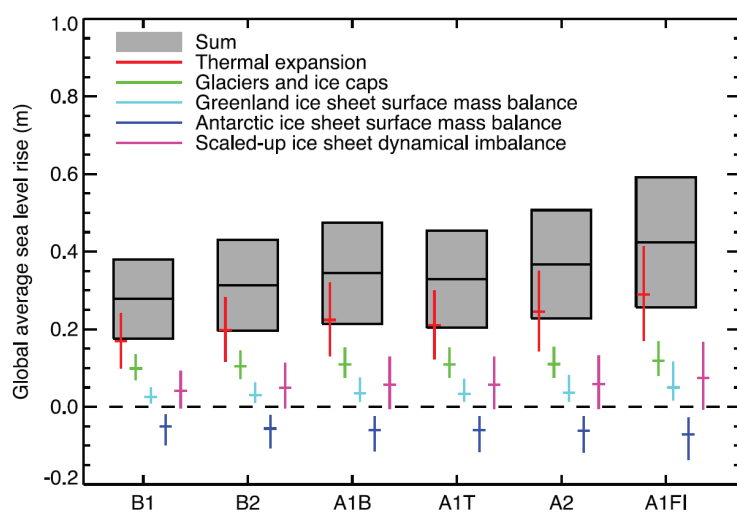


Figure 1.6: Projected global average sea level rise and its components in 2090 to 2099 (relative to 1980-1999) for the six scenarios [Solomon et al., 2007].

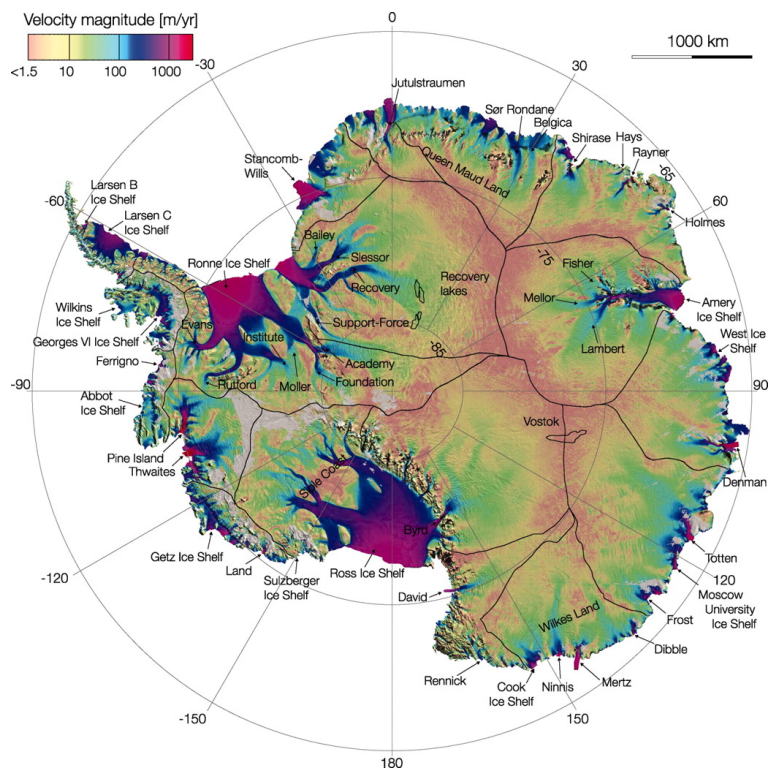


Figure 1.7: The velocity field of the Antarctic ice sheet [Rignot et al., 2011a]. It is derived from ALOS PALSAR, Envisat ASAR, RADARSAT-2 and ERS-1/2 satellite radar interferometry. Thick black lines delineate major ice divides. Thin black lines outline subglacial lakes discussed in the text.

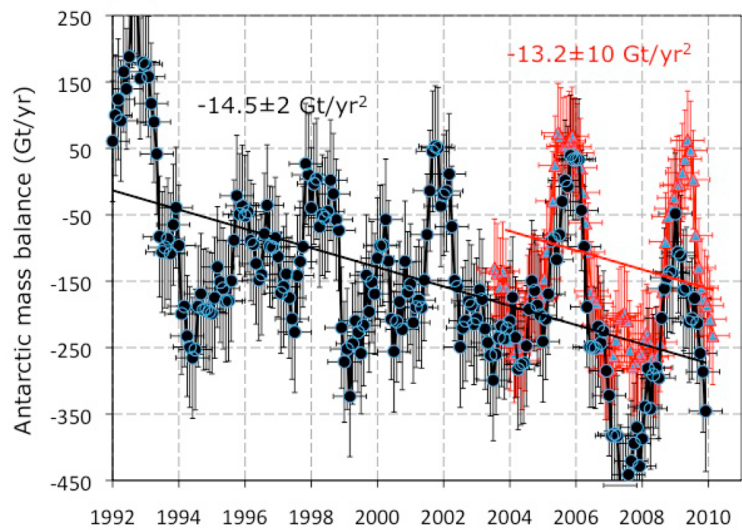


Figure 1.8: Total of the Antarctic ice sheet mass balance, dM/dt , between 1992 and 2009 in Gt/yr. The black circle is derived from the mass budget method (MBM). The red triangle is derived from GRACE time-variable gravity. The error bar and the trend (black (MBM) and red lines (GRACE)) are also shown [Rignot et al., 2011b].

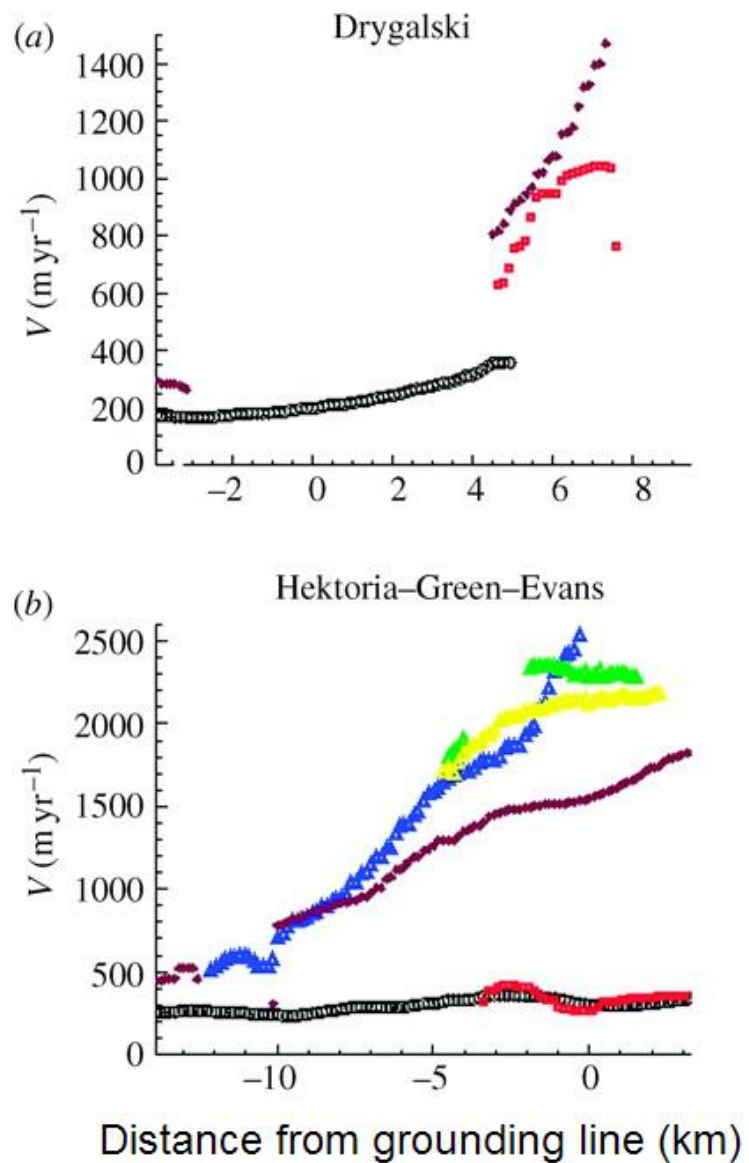


Figure 1.9: Glacier acceleration after the collapse of Larsen A and B for (a) Drygalski, (b) Hektoria/Green/Evanst [Rignot, 2006]. Black square is 1996, red square is 2000, blue triangle is 2003, yellow triangle is 2003, green triangle is 2003 and purple diamond is 2005.

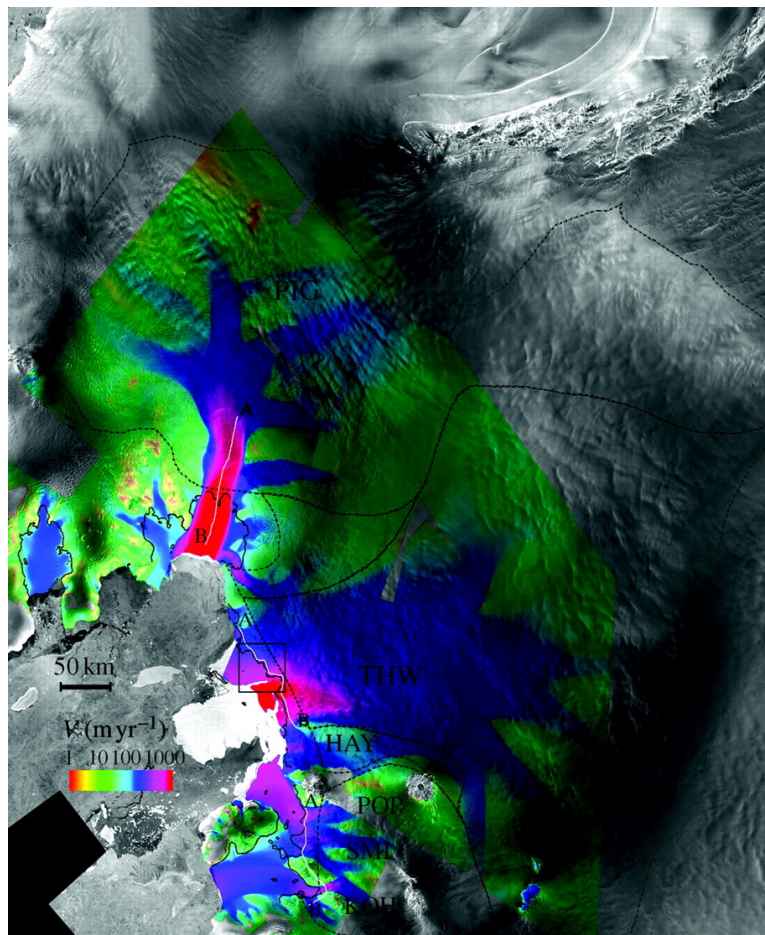


Figure 1.10: The velocity field of Pine Island bay on the WAIS [Rignot, 2006]. It is derived from ERS-1/2 1996 interferometry, overlaid on a RADARSAT-1 map of radar brightness. The grounding line is thin black.

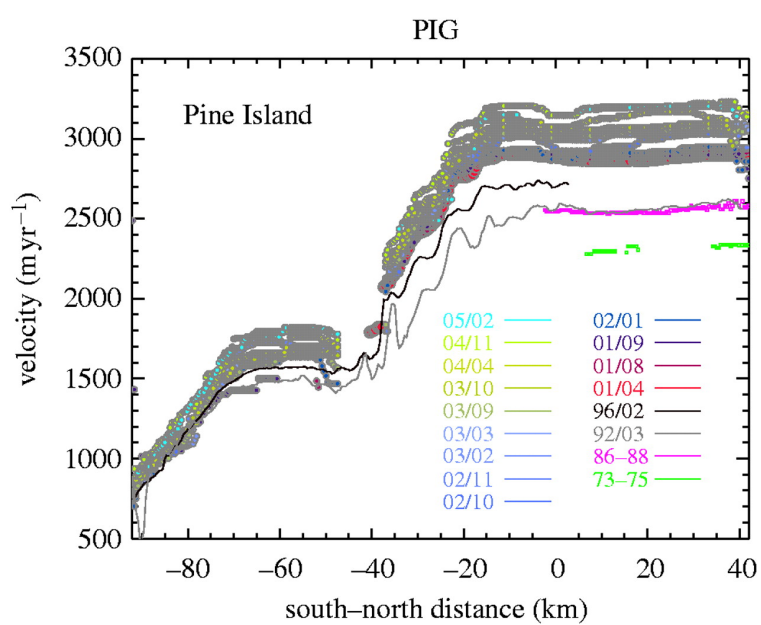


Figure 1.11: Acceleration of the Pine Island glacier from 1974, 1987, 1992, 1996 (ERS-1/2) and 2001-2005 (RADARSAT-1) versus distance along the glacier flow line [Rignot, 2006].

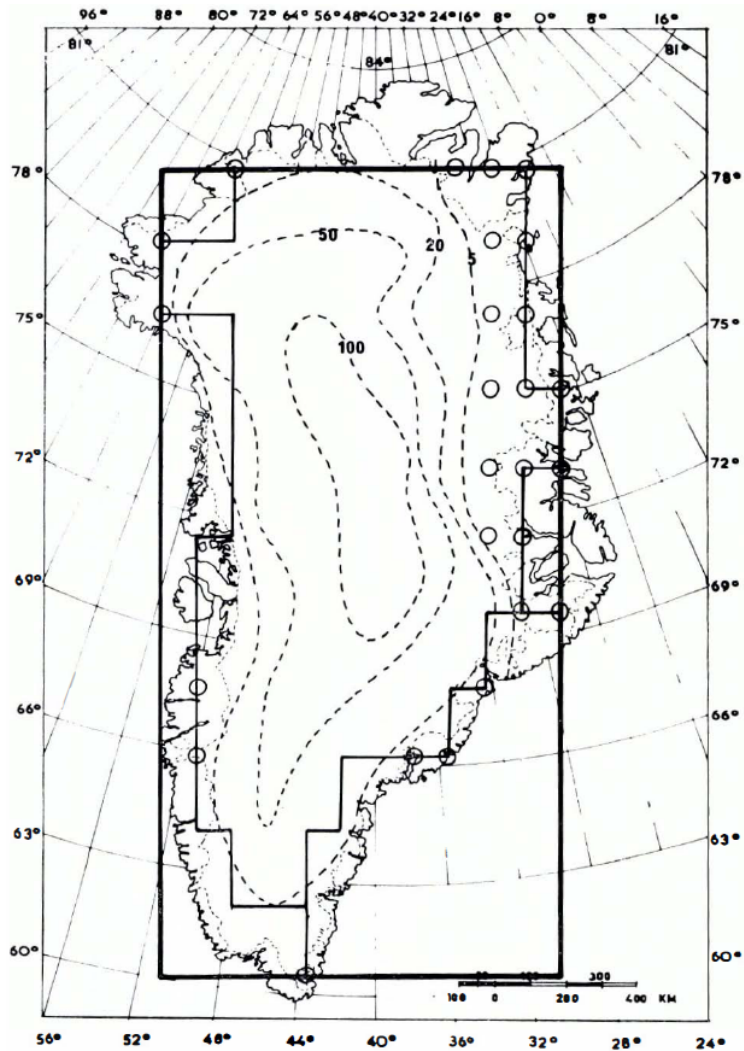


Figure 1.12: The domains of the ice sheet model (black line) and a maximum time step (year) for the simulation. The horizontal grid spacing is 100 km for west-east and 200 km for north-south. [Jenssen, 1977].

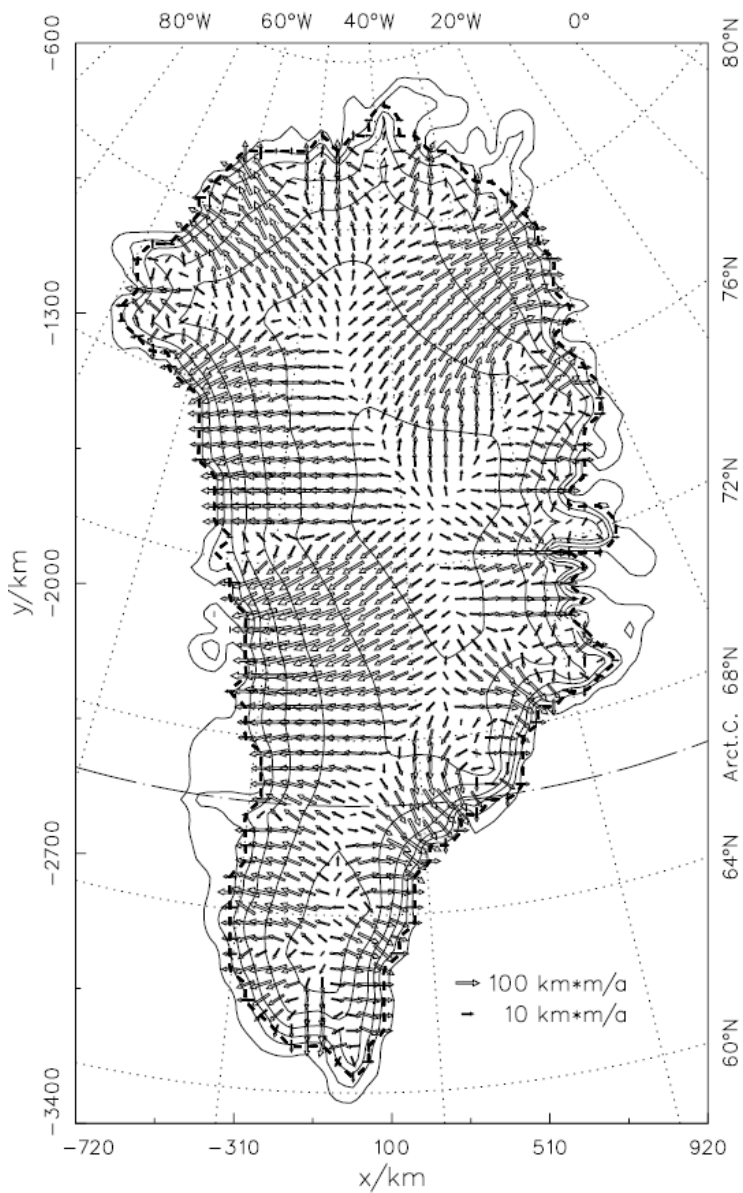


Figure 1.13: Examples of the application of the ice sheet model SICOPOLIS to (a) the steady state velocity of Greenland ice sheet for the present climate [Greve, 1997a].

Chapter 2

Theory

2.1 Dynamics of large ice bodies

The typical geometry (cross-section) of an ice sheet consists of a grounded ice sheet with a floating ice shelf attached (Fig. 2.1) (The ice shelf will be treated, as well as its interactions with the atmosphere (snowfall, melting), the lithosphere (geothermal heat flux, isostasy) and the ocean (melting and calving)).

Ice flow is slow enough for the acceleration term in Newton's Second Law to be neglected. This means that a glacier is in static equilibrium even when it is moving. The forces working in a glacier and an ice sheet are in balance.

Gravity pulls a glacier vertically downward. The resultant driving forces mainly depends on the slope of the ice surface. Consider an ice body with thickness H and surface slope α . The driving force, τ_d , is

$$\tau_d = \rho g H \sin \alpha, \quad (2.1)$$

where g is the gravitational constant, ρ is the density of ice; which is considered as the constant in this study. The largest forces resisting this stress are the basal shear stresses, τ_b . Other components are the side wall effects (τ_w , the side drag) and stretching and compression ice (τ_L , the longitudinal drag). Therefore, the total momentum balance is

$$\tau_d = \tau_b + \tau_w + \tau_L. \quad (2.2)$$

This is the force balance acting in an ice sheet.

2.2 Constitutive equations

Ice crystals have lattice defects. This is because the system has higher entropy with defects than without. Dislocations, a type of defect movement,

causes the deformation of ice crystals (Fig. 2.2). There is a relationship between dislocation theory and the constitutive equation [e.g., Gudmundsson, 2007]. Consider a crystal with height h , width w , and thickness l . Burger's vector of a dislocation is b . When n dislocations with length l , moved a distance x in the crystal, the shearing deformation e of the crystal is

$$e = \frac{nb}{h} \frac{x}{w}. \quad (2.3)$$

Dislocation density ρ is defined as the sum of dislocations in a unit cell. Since a dislocation is a line defect, its density is

$$\frac{nl}{hwl} = \frac{n}{hw}. \quad (2.4)$$

with the result that the time differentiation of the shear deformation equation is

$$\dot{e} = \rho b \dot{x} = \rho b v. \quad (2.5)$$

Dislocation density ρ is inversely proportional to the square of dislocation distance d ,

$$\rho \propto d^{-2}. \quad (2.6)$$

d is related to internal stress σ by Hooke's law,

$$\sigma \propto \frac{\mu b}{d}, \quad (2.7)$$

where μ is the rigidity modulus.

Those two equations imply the Bailey-Hirsch relationship

$$\sigma \propto \frac{\sigma^2}{\mu^2 b^2}. \quad (2.8)$$

because dislocation velocity is proportional to the stress,

$$v = C\sigma. \quad (2.9)$$

With (7), (8) and (4), the strain rates are proportional to the third power of the internal stress,

$$\dot{e} = C\sigma^3. \quad (2.10)$$

The constitutive equation for a viscous material is

$$\dot{e} = \frac{1}{2\eta(T, p, \sigma_e)}. \quad (2.11)$$

The inverse viscosity is called fluidity, and its dependence on the temperature T, the pressure p and the absolute value of σ_e can be factorized as

$$\frac{1}{\eta(T, p, |\tau|)} = 2A(T, p)f(\sigma_e) = 2A(T, p)\sigma_e^{n-1} \quad (2.12)$$

where A(T,p) is called the rate factor and $f(|\tau|)$ is the creep function. This equation and equation (9) give Glen's flow law,

$$\dot{\epsilon} = A(T, p)\sigma_e^2. \quad (2.13)$$

Glen's flow law yields an infinite viscosity when the effective stress approaches zero. This is not a problem physically because the strain rate is small when the effective stress is small. It therefore contributes little to large scale flow. However, depending on the mathematical solution procedure, the infinite viscosity limit may introduce a singularity in the equations for the velocity field if the effective stress is very small, which occurs at ice divides and ice margins. In order to avoid this problem, a regularization has been proposed in which the power law is replaced by a polynomial relationship,

$$f(\sigma_e) = \sigma_e^{n-1} + \sigma_0^{n-1}, \quad (2.14)$$

where the residual stress σ_0 is a small positive constant. This is the “regularized Glen's flow law” and viscosity is then

$$\eta(T', \sigma_e) = \frac{1}{2A(T, p)(\sigma_e^{n-1} + \sigma_0^{n-1})}, \quad (2.15)$$

which has finite viscosity at the limit $\sigma_e \rightarrow 0$,

$$\eta_{\sigma_e \rightarrow 0} = \frac{1}{2A(T, p)\sigma_0^{n-1}}. \quad (2.16)$$

2.3 Stress balance equations in general coordinates

The general coordinate invariance is one of the important principles of general relativity. The classical field theory gives

$$G^{ij} + \Lambda g^{ij} = \frac{8\pi G}{c^4}T^{ij}, \quad (2.17)$$

where G^{ij} is the Einstein tensor, Λ is the cosmological constant, g^{ij} is the metric tensor, G is Newton's gravitational constant, c is speed of light in a

vacuum, and T^{ij} is the stress energy momentum tensor. It uses Einstein's convention (sum over the coordinates, $i = 1$ to 4). It is also possible to understand Navier Stokes and Stokes equations as a form of the classical field theory, the field equation. The energy and momentum balance equation is

$$T^{ij}_{;j} = 0. \quad (2.18)$$

(This equation is valid in a local system. It is also necessary to consider a term for the energy momentum caused by gravity [Landau and Lifshitz, 1980].) The space components ($i = 1$ to 3) of the energy momentum tensor represent stresses. Note that $_;$ means the covariant derivative, $_$ is the ordinary derivative and Γ is the Christoffel symbol. How the energy momentum tensor should be formulated depends on the problem. In a viscous fluid in Cartesian coordinates, T^{ij} is

$$T^{ij} = -pg^{ij} + \eta(\rho + p)u^i u^j + \tau^{ij}. \quad (2.19)$$

The form of τ^{ij} in the dissipative system is given by the second law of thermodynamics [cf. Landau and Lifshitz, 1987]. In Cartesian coordinates,

$$t^{ij} = -\eta \left(\frac{\partial u^i}{\partial x^j} + \frac{\partial u^j}{\partial x^i} + u_j u^l \frac{\partial u^i}{\partial x^l} \right) - \left(\zeta - \frac{2}{3}\eta \right) \frac{\partial u^l}{\partial x^l} (g^{ij} + u^i u^k). \quad (2.20)$$

In a perfect fluid,

$$T^{ij} = (\rho + p)u^i u^j + g^{ij}p, \quad (2.21)$$

where ρ means the mass energy density and p the pressure. The zero component is the mass balance,

$$T^{0j}_{,j} = \frac{1}{c} \left(\frac{\partial \rho}{\partial t} + \rho u^j_{,j} \right). \quad (2.22)$$

This provides the mass and energy balance.

Since an ice sheet is relatively slow, it is possible to neglect the acceleration term of momentum balance. This produces Stokes equation which, in general coordinates, can be formulated as

$$t^{ij}_{,j} = t^{ij}_{,j} + \Gamma^i_{kj} t^{kj} + \Gamma^j_{kj} t^{ik} = f^j \delta^i_j, \quad (2.23)$$

where $f^j \delta^i_j$ is the external force. In this study, the external force is gravity. The stress balance in large-scale ice sheet dynamics is discussed in this section. The constitutive equation for the general ice sheet model is shown in the figure. The figure is shown in this section. The external gravitational force vector is

$$f^i = g^{ij} f_j = (0, 0, \rho G). \quad (2.24)$$

2.4 Large-scale ice sheet dynamics

In most parts of a large ice sheet, the flow regime is essentially simple, bed-parallel shear. The geometry of real ice sheets is such that they are shallow, i.e. the typical horizontal length scale exceeds the typical ice-thickness scale by several orders of magnitude. The slopes of the free surface and the ice base are small. The typical thickness of the ice sheet is $[H] = 1000\text{ m}$, Therefore, the typical scale of the surface slope is

$$\frac{[H]}{[L]} = \frac{10^3}{10^6} = 10^{-3}. \quad (2.25)$$

Under this condition, the normal stress deviations t_{xx}^D , t_{yy}^D and t_{zz}^D are negligible compared to vertical shear stresses,

$$\frac{t_{xx}^D}{t_{xz}^D} = \frac{[\eta] \frac{[v]}{[L]}}{[\eta] \frac{[v]}{[H]}} = \frac{[H]}{[L]} = 10^{-3}. \quad (2.26)$$

Since the shape of the Earth or a planet in general is close to a sphere, the atmospheric and ocean general circulation models consider the effect of the curvature. One way to treat the effect is to apply orthogonal curvilinear coordinates. Consider an ice sheet on a planet surface. In most cases, ice thickness is very small compared to the distance from the surface to the core. The difference of the curvature in “the vertical direction”, which is the direction of the gravitational force, is negligible. This allows the use of orthogonal curvilinear coordinates which have a gravitational force in the vertical direction of γ , and two horizontal coordinates which are perpendicular to the vertical direction, α and β . This represents a shallow ice body on a plane which has curvilinear horizontal coordinates.

In orthogonal curvilinear coordinates, the metric tensor only has diagonal elements. As a consequence of the above, the vertical component of the coordinate can be set to $g_3 = 1$. Since the curvature of time is not considered in this situation, it is unnecessary to consider the zero dimension of the metric tensor. Therefore, the metric tensor is

$$g_{ij} = \begin{pmatrix} g_{11} & 0 & 0 \\ 0 & g_{22} & 0 \\ 0 & 0 & 1 \end{pmatrix}$$

2.5 Hydrostatic approximation

The scale of the shear stresses (less than 100 kPa) is smaller than the vertical normal stress (10 MPa). Therefore, the stress balance for the vertical

coordinate can be approximated by

$$\partial_i T^{\gamma i} = \frac{1}{\sqrt{g}} \frac{\partial t^\gamma_\gamma}{\partial \gamma} = \rho G. \quad (2.27)$$

Since atmospheric pressure is negligible compared to the pressure in the ice, the vertical normal stress on the surface, h , is

$$t^\gamma_\gamma|_{\gamma=h} = 0. \quad (2.28)$$

The balance equation in the vertical direction can be integrated from the depth, γ , to the surface, h ,

$$t^\gamma_\gamma = -\rho G(h - \gamma). \quad (2.29)$$

Therefore, the vertical normal stress can be approximated to the hydrostatic pressure in the orthogonal curvilinear coordinate system as in Cartesian coordinates. Pressure is formulated as

$$p = \rho G(h - \gamma) - (t^D)_\alpha^\alpha - (t^D)_\beta^\beta. \quad (2.30)$$

This results in the horizontal normal stress changing to

$$\begin{aligned} t^\alpha_\alpha &= 2(t^D)_\alpha^\alpha + (t^D)_\beta^\beta - \rho G(h - \gamma), \\ t^\beta_\beta &= 2(t^D)_\beta^\beta + (t^D)_\alpha^\alpha - \rho G(h - \gamma). \end{aligned} \quad (2.31)$$

Then the horizontal stress balance equations are expressed as

$$2 \frac{\partial(t^D)_\alpha^\alpha}{\partial \alpha} + \frac{\partial(t^D)_\beta^\beta}{\partial \alpha} + \frac{\partial t^\beta_\alpha}{\partial \beta} + \frac{\partial t^\gamma_\alpha}{\partial \gamma} + \frac{1}{2g_2} \frac{\partial g_2}{\partial \alpha} ((t^D)_\alpha^\alpha - (t^D)_\beta^\beta) \quad (2.32)$$

$$+ \frac{1}{2g_2} \frac{\partial g_1}{\partial \alpha} t^\alpha_\beta + \frac{1}{2g_2} \frac{\partial g_2}{\partial \beta} t^\beta_\alpha = \rho G \frac{\partial(h - \gamma)}{\partial \alpha}, \quad (2.33)$$

$$2 \frac{\partial(t^D)_\beta^\beta}{\partial \beta} + \frac{\partial(t^D)_\alpha^\alpha}{\partial \beta} + \frac{\partial t^\alpha_\beta}{\partial \alpha} + \frac{\partial t^\gamma_\beta}{\partial \gamma} + \frac{1}{2g_1} \frac{\partial g_1}{\partial \beta} ((t^D)_\beta^\beta - (t^D)_\alpha^\alpha) \quad (2.34)$$

$$+ \frac{1}{2g_1} \frac{\partial g_2}{\partial \beta} t^\beta_\alpha + \frac{1}{2g_1} \frac{\partial g_1}{\partial \alpha} t^\alpha_\beta = \rho G \frac{\partial(h - \gamma)}{\partial \beta}. \quad (2.35)$$

This is the first order hydrostatic approximation of the stress balance in this coordinate system. The vertical velocity is estimated with the incompressible mass balance equation,

$$T^{0j}_{;j} = 0. \quad (2.36)$$

On the viscous ice

$$(t^D)^{ij} = 2\eta D^{ij}. \quad (2.37)$$

The relationship of strain rates to velocities is

$$D^i_j = \frac{1}{2}(u^i_{;j} + g_{kj}g^{il}u^k_{;l}). \quad (2.38)$$

It is also possible to apply further approximations. The horizontal difference between the vertical velocities is negligible [Greve and Blatter, 2009],

$$u^\gamma_{;\alpha} = 0, \quad u^\gamma_{;\beta} = 0. \quad (2.39)$$

Finally, the stress balance equation is

$$2\frac{\partial(t^D)^\alpha_\alpha}{\partial\alpha} + \frac{\partial(t^D)^\beta_\beta}{\partial\alpha} + \frac{\partial t^\beta_\alpha}{\partial\beta} + \frac{\partial t^\gamma_\alpha}{\partial\gamma} + \frac{1}{2g_2}\frac{\partial g_2}{\partial\alpha}((t^D)^\alpha_\alpha - (t^D)^\beta_\beta) \quad (2.40)$$

$$+ \frac{1}{2g_2}\frac{\partial g_1}{\partial\alpha}t^\alpha_\beta + \frac{1}{2g_2}\frac{\partial g_2}{\partial\beta}t^\beta_\alpha = \rho G\frac{\partial(h - \gamma)}{\partial\alpha}, \quad (2.41)$$

$$2\frac{\partial(t^D)^\beta_\beta}{\partial\beta} + \frac{\partial(t^D)^\alpha_\alpha}{\partial\beta} + \frac{\partial t^\alpha_\beta}{\partial\alpha} + \frac{\partial t^\gamma_\beta}{\partial\gamma} + \frac{1}{2g_1}\frac{\partial g_1}{\partial\beta}((t^D)^\beta_\beta - (t^D)^\alpha_\alpha) \quad (2.42)$$

$$+ \frac{1}{2g_1}\frac{\partial g_2}{\partial\beta}t^\beta_\alpha + \frac{1}{2g_1}\frac{\partial g_1}{\partial\alpha}t^\alpha_\beta = \rho G\frac{\partial(h - \gamma)}{\partial\beta}. \quad (2.43)$$

which is the first order approximation. It is important to set the vertical axis to set the direction of gravitational force. Otherwise, the hydrostatic approximation (first order approximation) does not work as in the Cartesian coordinates. The reason is that in that case the gravitational force vectors are not zero in the horizontal coordinates. If the distance is not very great, $t_{\gamma\gamma}$ is larger than the other part of the stress balance. Although the gravitational term in the horizontal coordinate needs to be considered, the concept of the hydrostatic approximation may not be compromised if the vertical normal stress is sufficiently large. However, if the horizontal distance is not negligible, the validity of the theory itself is damaged. In other words, the first order approximation loses its validity when the space is sufficiently large and Cartesian coordinates alone are used. It is therefore undesirable to use Cartesian coordinates in this type of approximation for continental or global scale conditions. An alternative strategy is to consider the directions of the gravitational force in the force balance. In this case, it is preferable to estimate the ratio of shear stress to normal stress and the gravitational term in horizontal directions to check validity.

2.6 Shallow shelf approximation

2.6.1 Formulation in orthogonal curvilinear coordinates

Since there is no basal drag beneath ice shelves, there is no basal shear stress. The effects of the side wall force and longitudinal resistant force are components of the total local force balance,

$$\tau_d = \tau_w + \tau_L. \quad (2.44)$$

The difference from Eq. (2.2) is that it does not have τ_b . Forces acting at the shelf edges and sides influence the flow even at locations far from these boundaries since the local basal drag is negligible. To construct meaningful analyses of shelf dynamics, the force balance relationship needs to be integrated over the distance from a point in the shelf to the calving front.

The typical situation is that of plug flow, whereby the horizontal velocities are essentially constant over depth (Fig. 2.4). Naturally, in the immediate vicinity of the grounding line, a transitional state between these two limits will develop. Mathematically, the regime of plug flow can be defined by

$$\begin{aligned} \frac{\partial u^\alpha}{\partial \gamma} &\approx 0, \\ \frac{\partial u^\beta}{\partial \gamma} &\approx 0. \end{aligned} \quad (2.45)$$

In other words, horizontal velocities depend only on the horizontal coordinates and on time,

$$u^\alpha = u^\alpha(\alpha, \beta, t), \quad u^\beta = u^\beta(\alpha, \beta, t). \quad (2.46)$$

In orthogonal curvilinear coordinates, basal friction is negligible as in Cartesian coordinates. Moreover, the direction of the gravitational force is parallel to the vertical direction, the horizontal velocities do not depend on the vertical direction. Mathematically speaking, the Jacobian is 1 since $g_3 = 1$. It is therefore possible to apply the shallow shelf approximation, the vertically integrated stress balance, in orthogonal curvilinear coordinates.

2.6.2 Boundary conditions at the ice surface

The surface function, F_s , is defined as

$$F_s(\alpha, \beta, t) = \gamma - h(\alpha, \beta, t) = 0. \quad (2.47)$$

The normalized vector gradient is

$$n_i = \frac{F_{s;i}}{|F_{s;i}|} = \frac{1}{N_s} \left(-\frac{\partial h}{\partial \alpha}, -\frac{\partial h}{\partial \beta}, 1 \right), \quad (2.48)$$

where N_s is

$$N_s = |F_{s;i}|. \quad (2.49)$$

The stress free condition is

$$t^j_i g_j = 0. \quad (2.50)$$

2.6.3 Boundary conditions at the ice base

The momentum jump condition is

$$(t_{sea}^j)_i g_j - t^j_i g_j + g_{ij} \rho a_b [u^j] = 0, \quad (2.51)$$

where

$$\begin{aligned} (t_{sea}^j)_i g_j &= -p_{sea} g_i + (\tau_{sea})_i^j g_j \\ &= -\rho G(\gamma_{sl} - b) g_i + C_{wi} \rho_{sw} |u_{sea}|^2 (g_\tau)_i, \end{aligned} \quad (2.52)$$

where $(g_\tau)_i$ is the tangent vector. Since the shear stress from ocean currents is negligible, this equation changes to

$$t^j_i g_j = \rho G(\gamma_{sl} - b) g_i. \quad (2.53)$$

2.6.4 Vertical integration

This characteristic of ice shelf dynamics can be described well by the shallow shelf approximation. Since an ice shelf has no basal friction, the vertical shear stress is negligible. Therefore, horizontal velocities do not depend on the vertical coordinate. To make use of this property, the momentum balance equations are integrated over depth. In the orthogonal curvilinear coordinates with shallow conditions, it is possible to treat vertical integration

as the Cartesian coordinate. The vertically integrated momentum balance is

$$\begin{aligned}
& 2 \frac{\partial N^\alpha_\alpha}{\partial \alpha} + \frac{\partial N^\beta_\beta}{\partial \alpha} + \frac{\partial N^\beta_\alpha}{\partial \beta} + \frac{\partial N^\gamma_\alpha}{\partial \gamma} + \frac{1}{2g_2} \frac{\partial g_2}{\partial \alpha} (N^\alpha_\alpha - N^\beta_\beta) \\
& + \frac{1}{2g_2} \left(\frac{\partial g_1}{\partial \alpha} N^\alpha_\beta + \frac{\partial g_2}{\partial \beta} N^\beta_\alpha \right) - 2(t^D)_\alpha^\alpha|_{\gamma=h} \frac{\partial h}{\partial \alpha} + 2(t^D)_\alpha^\alpha|_{\gamma=b} \frac{\partial b}{\partial \alpha} \\
& - t^\beta_\alpha|_{\gamma=h} \frac{\partial h}{\partial \beta} + t^\beta_\alpha|_{\gamma=b} \frac{\partial b}{\partial \beta} - (t^D)_\beta^\beta|_{\gamma=h} \frac{\partial h}{\partial \alpha} - (t^D)_\beta^\beta|_{\gamma=b} \frac{\partial b}{\partial \alpha} \\
& + t^\gamma_\alpha|_{\gamma=h} - t^\gamma_\alpha|_{\gamma=b} = \rho G \frac{\partial(h - \gamma)}{\partial \alpha}, \quad (2.54) \\
& 2 \frac{\partial N^\beta_\beta}{\partial \beta} + \frac{\partial N^\alpha_\alpha}{\partial \beta} + \frac{\partial N^\alpha_\beta}{\partial \alpha} + \frac{\partial N^\alpha_\beta}{\partial \alpha} + \frac{1}{2g_1} \frac{\partial g_1}{\partial \beta} (N^\beta_\beta - N^\alpha_\alpha) \\
& + \frac{1}{2g_1} \left(\frac{\partial g_2}{\partial \beta} N^\beta_\alpha + \frac{\partial g_1}{\partial \alpha} N^\alpha_\beta \right) - 2(t^D)_\beta^\beta|_{\gamma=h} \frac{\partial h}{\partial \beta} + 2(t^D)_\beta^\beta|_{\gamma=b} \frac{\partial b}{\partial \beta} \\
& - t^\alpha_\beta|_{\gamma=h} \frac{\partial h}{\partial \alpha} + t^\alpha_\beta|_{\gamma=b} \frac{\partial b}{\partial \alpha} - (t^D)_\alpha^\alpha|_{\gamma=h} \frac{\partial h}{\partial \beta} - (t^D)_\alpha^\alpha|_{\gamma=b} \frac{\partial b}{\partial \beta} \\
& + t^\gamma_\beta|_{\gamma=h} - t^\gamma_\beta|_{\gamma=b} = \rho G \frac{\partial(h - \gamma)}{\partial \beta}
\end{aligned}$$

The membrane stress N , is defined as

$$N^{ij} = \int_b^h (t^D)_j^i d\gamma. \quad (2.55)$$

The boundary condition on the surface and the base can be considered as in the Cartesian coordinate. The surface condition is

$$\begin{aligned}
& -2(t^D)_\alpha^\alpha|_{\gamma=h} \frac{\partial h}{\partial \alpha} - (t^D)_\beta^\beta|_{\gamma=h} \frac{\partial h}{\partial \alpha} - t^\beta_\alpha|_{\gamma=h} \frac{\partial h}{\partial \beta} + t^\gamma_\alpha|_{\gamma=h} = 0, \\
& -2(t^D)_\beta^\beta|_{\gamma=h} \frac{\partial h}{\partial \beta} - (t^D)_\beta^\beta|_{\gamma=h} \frac{\partial h}{\partial \beta} - t^\beta_\alpha|_{\gamma=h} \frac{\partial h}{\partial \alpha} + t^\gamma_\beta|_{\gamma=h} = 0, \quad (2.56) \\
& t^\gamma_\gamma|_{\gamma=h} = 0.
\end{aligned}$$

The boundary condition on the ice base is

$$\begin{aligned}
& -2(t^D)_\alpha^\alpha|_{\gamma=b} \frac{\partial b}{\partial \alpha} - (t^D)_\beta^\beta|_{\gamma=b} \frac{\partial b}{\partial \alpha} - t^\beta_\alpha|_{\gamma=b} \frac{\partial b}{\partial \beta} + t^\gamma_\alpha|_{\gamma=b} \\
& = \frac{\rho_{sw}G}{g_1} (\gamma_{sl} - b) \frac{\partial b}{\partial \alpha}, \\
& -2(t^D)_\beta^\beta|_{\gamma=b} \frac{\partial b}{\partial \beta} - (t^D)_\beta^\beta|_{\gamma=b} \frac{\partial b}{\partial \beta} - t^\beta_\alpha|_{\gamma=b} \frac{\partial b}{\partial \alpha} + t^\gamma_\beta|_{\gamma=b} \\
& = \frac{\rho_{sw}G}{g_2} (\gamma_{sl} - b) \frac{\partial b}{\partial \beta}, \quad (2.57) \\
& t^\gamma_\gamma|_{\gamma=b} = \rho_{sw}G(\gamma - b).
\end{aligned}$$

It is possible to replace $\rho_{sw}G(\gamma_{sl} - b)$ to ρGH by using the hydrostatic condition,

$$\rho H = \rho_{sw}(\gamma_{sl} - b). \quad (2.58)$$

Thus, the boundary condition at the ice base is

$$\begin{aligned} -2(t^D)^\alpha_\alpha|_{\gamma=b} \frac{\partial b}{\partial \alpha} - (t^D)^\beta_\beta|_{\gamma=b} \frac{\partial b}{\partial \alpha} - t^\beta_\alpha|_{\gamma=b} \frac{\partial b}{\partial \beta} + t^\gamma_\alpha|_{\gamma=b} &= 0, \\ -2(t^D)^\beta_\beta|_{\gamma=b} \frac{\partial b}{\partial \beta} - (t^D)^\beta_\beta|_{\gamma=b} \frac{\partial b}{\partial \beta} - t^\beta_\alpha|_{\gamma=b} \frac{\partial b}{\partial \alpha} + t^\gamma_\beta|_{\gamma=b} &= 0, \\ t^\gamma_\gamma|_{\gamma=b} &= \rho H. \end{aligned} \quad (2.59)$$

With the condition of 2.56 and 2.59, 2.54 becomes

$$2 \frac{\partial N^\alpha_\alpha}{\partial \alpha} + \frac{\partial N^\beta_\beta}{\partial \alpha} + \frac{\partial N^\beta_\alpha}{\partial \beta} + \frac{\partial N^\gamma_\alpha}{\partial \gamma} + \frac{1}{2g_2} \frac{\partial g_2}{\partial \alpha} (N^\alpha_\alpha - N^\beta_\beta) \quad (2.60)$$

$$+ \frac{1}{2g_2} \frac{\partial g_1}{\partial \alpha} t^\alpha_\beta + \frac{1}{2g_2} \frac{\partial g_2}{\partial \beta} t^\beta_\alpha = \rho G \frac{\partial(h - \gamma)}{\partial \alpha}, \quad (2.61)$$

$$2 \frac{\partial N^\beta_\beta}{\partial \beta} + \frac{\partial N^\alpha_\alpha}{\partial \beta} + \frac{\partial N^\alpha_\beta}{\partial \alpha} + \frac{\partial N^\alpha_\beta}{\partial \alpha} + \frac{1}{2g_1} \frac{\partial g_1}{\partial \beta} (N^\beta_\beta - N^\alpha_\alpha) \quad (2.62)$$

$$+ \frac{1}{2g_1} \frac{\partial g_2}{\partial \beta} t^\beta_\alpha + \frac{1}{2g_1} \frac{\partial g_1}{\partial \alpha} t^\alpha_\beta = \rho G \frac{\partial(h - \gamma)}{\partial \beta}. \quad (2.63)$$

The constitutive equation for viscous ice when vertically integrated is

$$N^i_j = 2\bar{\eta} D^i_j, \quad (2.64)$$

where η is the vertically integrated viscosity,

$$\bar{\eta} = \int_b^h \eta d\gamma = \frac{1}{2} d_e^{-(1-1/n)} \int_b^h B(T') d\gamma, \quad (2.65)$$

and D is the strain rate tensor,

$$D^i_j = \frac{1}{2} (u^i_{;j} + g_{kj} g^{il} u^k_{;l}). \quad (2.66)$$

The momentum balance equation in Cartesian coordinates is

$$\begin{aligned} 4 \frac{\partial}{\partial x} \left(\bar{\eta} \frac{\partial v_x}{\partial x} \right) + 2 \frac{\partial}{\partial x} \left(\bar{\eta} \frac{\partial v_y}{\partial y} \right) + \frac{\partial}{\partial y} \left(\bar{\eta} \left(\frac{\partial v_x}{\partial y} + \frac{\partial v_y}{\partial x} \right) \right) &= \rho g H \frac{\partial h}{\partial x}, \\ 4 \frac{\partial}{\partial y} \left(\bar{\eta} \frac{\partial v_y}{\partial y} \right) + 2 \frac{\partial}{\partial y} \left(\bar{\eta} \frac{\partial v_x}{\partial x} \right) + \frac{\partial}{\partial x} \left(\bar{\eta} \left(\frac{\partial v_x}{\partial y} + \frac{\partial v_y}{\partial x} \right) \right) &= \rho g H \frac{\partial h}{\partial y}. \end{aligned} \quad (2.67)$$

This is called shallow shelf approximation [Greve and Blatter, 2009].

The vertical velocity is

$$\begin{aligned} v_z &= v_z|_{z=z_{sl}} - \int_{z_{sl}}^z \left(\frac{\partial v_x}{\partial x} + \frac{\partial v_y}{\partial y} \right) . \\ &= v_z|_{z=z_{sl}} - (z - z_{sl}) \left(\frac{\partial v_x}{\partial x} + \frac{\partial v_y}{\partial y} \right) . \end{aligned} \quad (2.68)$$

The difference between this and the shallow ice approximation is the different reference horizons. The reference for ice shelves is sea level but for ice sheets it is the base of the ice sheet. Moreover, precise integration is unnecessary because horizontal velocities do not depend on the vertical direction.

2.7 Shallow ice approximation

The driving force balances basal shear stresses in most parts of a large ice sheet

$$\tau_d = \tau_b. \quad (2.69)$$

The local stress balance does not depend on non-local effects, wall drag and longitudinal drag. This is a characteristic of large ice sheets.

The total hydrostatic pressure approximates to

$$p = \rho g H = \rho g (h - z). \quad (2.70)$$

and the horizontal components of the momentum balance simplify to

$$\begin{aligned} \frac{\partial t_{xz}}{\partial x} &= \frac{\partial p}{\partial x} = \rho g \frac{\partial h}{\partial x}, \\ \frac{\partial t_{yz}}{\partial y} &= \frac{\partial p}{\partial y} = \rho g \frac{\partial h}{\partial y}. \end{aligned} \quad (2.71)$$

Giving the shallow ice approximation [Greve and Blatter, 2009].

With Glen's flow law and the above concept, the horizontal velocities are

$$\begin{aligned} v_x &= v_{bx} - 2(\rho g)^3 |\nabla h|^2 \frac{\partial h}{\partial x} \int_b^z A(T, p) (h - \bar{z})^3 d\bar{z}, \\ v_y &= v_{by} - 2(\rho g)^3 |\nabla h|^2 \frac{\partial h}{\partial y} \int_b^z A(T, p) (h - \bar{z})^3 d\bar{z}. \end{aligned} \quad (2.72)$$

The vertical velocity can be computed by integrating the continuity equation from $z = b$ to z ,

$$v_z = v_z|_{z=b} - \int_b^z \left(\frac{\partial v_x}{\partial x} + \frac{\partial v_y}{\partial y} \right) . \quad (2.73)$$

2.8 Temperature evolution of ice

Because viscosity depends on temperature, a thermo-mechanically coupled problem applies, so complete formulation requires an evolution equation for the temperature field. The heat equation in orthogonal curvilinear coordinates is

$$\rho c \partial_i T = \frac{\partial}{\partial x^i} \frac{1}{\sqrt{g}} \left(\kappa \sqrt{g} g_{ij} \frac{\partial T}{\partial x^j} \right) + 4\eta d_e^2. \quad (2.74)$$

Note that ∂_i means sum over four vectors and d_e is the invariant. Since horizontal diffusion is smaller than other parts,

$$\rho c \left(\frac{\partial T}{\partial t} + \frac{u^\alpha}{g_1} \frac{\partial T}{\partial \alpha} + \frac{u^\beta}{g_2} \frac{\partial T}{\partial \beta} + u^\gamma \frac{\partial T}{\partial \gamma} \right) = \frac{1}{\sqrt{g}} \left(\frac{\partial}{\partial \gamma} \left(\kappa \sqrt{g} \frac{\partial T}{\partial \gamma} \right) \right) + 4\eta d_e^2 \quad (2.75)$$

[Greve and Blatter, 2009], where c is specific heat and κ is heat conductivity. Since the ice temperature must not exceed the pressure melting point, the solution of the equation is subject to the secondary condition $T < T_m$.

2.9 Boundary conditions

Ice sheets and glaciers do not only change centrally. Changes at their boundaries are also important processes, including basal sliding, accumulation and ablation, and calving front processes. These processes are summarized here.

2.9.1 Basal sliding

There are three components for ice sheet and glacier motion. These are plastic deformation of the ice, sliding of ice over its bed, and deformation of the bed itself. The basal motion of the ice consists of sliding of ice and deformation of the bed. They are the important components of ice flow. The bed can deform significantly only if it consists of sediments saturated with water at a pressure close to that exerted by the overlying ice. Sliding is expected where the basal ice is close to its melting point. Sliding and bed deformation are not mutually exclusive, displacement can occur at the interface between ice and a deforming bed. Indeed, this interface may be hard to define when the basal ice contains a lot of debris.

The basal processes under glaciers are still under discussion due to the difficulties of measuring them. Therefore, improving understanding of them is one of the current major problems in glacier physics. Some theories on these basal processes have been elaborated based on the available, but limited,

data and on physical considerations. The “sliding law” is the relationship between basal velocity, shear and normal stresses, and water pressure and the characteristics of the glacier’s bed. It is an important boundary condition for the analysis of flow in glaciers.

Two mechanisms are considered for ice flow over a rough, hard bed (Weertman, 1957). Ice can move over bed obstacles by the same process of creep deformation which gives rise to ice flux when there is no sliding. Alternatively, it can melt upstream of a bed obstacle due to increased pressure at that point. If refreezing is ignored and the ice is everywhere in contact with the bed, Fowler’s sliding law is

$$u_b = C_b \tau_b^n, \quad (2.76)$$

where u_b is the basal velocity and τ_b is basal shear stress. The constant, C_b , depends on the geometry of bed roughness and n is the exponent of Glen’s flow law.

Since hydrostatic pressure and water pressure affect basal flow, a theory was elaborated incorporating these components (e.g., Hindmarsh and Le Meur 2001). The basal sliding law used in this study is the sub-melt sliding law

$$u_b = C_b e^{T'_b \gamma} \frac{\tau_b^p}{N_b^q}. \quad (2.77)$$

The sliding law has been modified to allow for sub-melt sliding by adding the coefficient $\gamma = 1^\circ C$. T'_b is the temperature relative to pressure melting, p and q are exponents; $p = 3$ and $q = 2$ are used in this study. There are two options for the effective pressure N . One is

$$N = \rho g H, \quad (2.78)$$

where H is local ice thickness. This option considers only hydrostatic pressure of ice. Another is

$$N = \rho g H - p_w. \quad (2.79)$$

This option considers the reduction of the effective pressure through water pressure.

2.9.2 Calving front

The calving front of an ice shelf faces the ocean. Therefore, it is affected by the ocean’s hydrostatic pressure (Fig. 2.5). The hydrostatic pressure distribution of sea water provides a dynamic boundary condition for the calving front and this is

$$(t|_{cf})_i^j g_j = -p_{sw} g_i, \quad (2.80)$$

where p_{sw} is

$$\begin{aligned} p_{sw} &= 0, & \text{for } \gamma > \gamma_{sw} \\ &= \rho_{sw}G(\gamma_{sw} - \gamma) & \text{for } \gamma \leq \gamma_{sw} \end{aligned} \quad (2.81)$$

With the hydrostatic approximation and vertical integration, this gives

$$\begin{aligned} (2N^\alpha_\alpha + N^\beta_\beta)_{cf}g_\alpha + N^\beta_\alpha|_{cf}g_\beta &= \rho(1 - \frac{\rho}{\rho_{sw}})\frac{GH^2}{2}g_\alpha, \\ (2N^\beta_\beta + N^\alpha_\alpha)_{cf}g_\beta + N^\alpha_\beta|_{cf}g_\alpha &= \rho(1 - \frac{\rho}{\rho_{sw}})\frac{GH^2}{2}g_\beta. \end{aligned} \quad (2.82)$$

The calving front condition with Cartesian coordinates is

$$\begin{aligned} 4\bar{\eta}\frac{\partial v_x}{\partial x}|_{cf}n_x + 2\bar{\eta}\frac{\partial v_y}{\partial y}|_{cf}n_x + \bar{\eta}\left(\frac{\partial v_x}{\partial y} + \frac{\partial v_y}{\partial x}\right)_{cf}n_y &= \frac{\rho}{\rho_{sw}}(\rho_{sw} - \rho)\frac{gH^2}{2}n_x, \\ 4\bar{\eta}\frac{\partial v_y}{\partial y}|_{cf}n_y + 2\bar{\eta}\frac{\partial v_x}{\partial x}|_{cf}n_y + \bar{\eta}\left(\frac{\partial v_x}{\partial y} + \frac{\partial v_y}{\partial x}\right)_{cf}n_x &= \frac{\rho}{\rho_{sw}}(\rho_{sw} - \rho)\frac{gH^2}{2}n_y. \end{aligned} \quad (2.83)$$

The evolution of the calving front is the other condition. Nye's calving formulation is sometimes used in glacier models. But it may not apply to ice shelves. Although several applications of the dynamic calving law have been proposed (e.g., Alley et al. 2008), it is still under construction. Because of the lack of a better criterion, it has been assumed in some modelling studies that the ice shelf ends at the place where the ice thickness reaches a certain value, such as 250 m (Paterson 1994).

2.9.3 Surface temperature and mass balance

For temperature evolution, a further thermodynamic boundary condition must be given. This can be done simply by specifying the surface temperature T_s ,

$$T = T_s. \quad (2.84)$$

Since the temperature of ice cannot exceed its melting point, a finite temperature below melting point is applied.

Surface mass balance, a_s is given as an input from the atmosphere. If the surface temperature is above melting point, melting is considered.

2.9.4 Basal temperature and sub-marine mass balance

The base of an ice shelf rests in water by definition. At the interface between liquid water and solid ice, it should be on the pressure melting point of the ocean water. The basal temperature at the ice shelf base, T_b , is given as

$$T_b = T_m - 2^\circ\text{C}. \quad (2.85)$$

The mean melting point depression of sea water, 2°C , is applied. This is applied for the ice base as the boundary condition for temperature.

Sub-ice-shelf melting, m_m , is parameterized by a method inherited from the GRISLI model (Ritz et al., 2001),

$$m_m = \begin{cases} (m_m)_{\text{gl}} & \text{in the vicinity of the grounding line,} \\ (m_m)_{\text{cs}} & \text{over the continental shelf, } z_l > -1600 \text{ m,} \\ (m_m)_{\text{ao}} & \text{over the abyssal ocean, } z_l \leq -1600 \text{ m.} \end{cases} \quad (2.86)$$

Standard values were used for the three parameters $M_{\text{gl}} = 1 \text{ m ice equiv. a}^{-1}$, $M_{\text{cs}} = 0.1 \text{ m ice equiv. a}^{-1}$ and $M_{\text{ao}} = 10 \text{ m ice equiv. a}^{-1}$.

2.10 Topographic evolution

Ice sheet changes its shape by accumulation, ablation at the base and the surface, and by ice flux. The vertical integral of the continuity equation then gives the height function of the ice sheet. Two different approaches are introduced here; the ice surface equation and the ice thickness equation.

2.10.1 Ice thickness equation

The ice thickness equation is

$$\frac{\partial H}{\partial t} = \nabla \cdot \mathbf{Q} + a_s - a_b, \quad (2.87)$$

where \mathbf{Q} is the horizontal ice flux (the vertical integral of horizontal velocity), a_s is surface mass balance and a_b is basal mass balance.

Since the horizontal velocity is vertically constant at the ice shelf, the flux is

$$Q_x = u^\alpha H, \quad Q_y = u^\beta H. \quad (2.88)$$

Therefore, the ice thickness equation is

$$\frac{\partial H}{\partial t} = -H u^i_{,i} + a_s - a_b, \quad (2.89)$$

$$= \frac{H}{\sqrt{g}} \left(\frac{\partial \sqrt{g} u^\alpha}{\partial \alpha} + \frac{\partial \sqrt{g} u^\beta}{\partial \beta} \right) + a_s - a_b. \quad (2.90)$$

2.10.2 Ice surface equation

The ice thickness equation can be modified,

$$\begin{aligned}\frac{\partial H}{\partial t} &= -\text{div}Q + a_s - a_b, \\ \frac{d(h - b)}{dt} &= \text{div}Q + a_s - a_b,\end{aligned}\quad (2.91)$$

where h is the ice surface and b is the ice base. The elevation of the ice base is equal to the elevation of the lithospheric surface below the ice sheet. This is not the case for ice shelves because these float on the ocean. However, if sea level z_{sl} and ice surface are known, it is possible to estimate the elevation of the ice base using the floating condition

$$b = -\frac{\rho}{\rho_{sw} - \rho} h + \frac{\rho_{sw}}{\rho_{sw} - \rho} z_{sl}. \quad (2.92)$$

Therefore, the ice surface evolution equation in ice shelves is

$$\frac{\partial h}{\partial t} = -(1 - \frac{\rho}{\rho_{sw}}) \nabla \cdot \mathbf{Q} + \frac{\partial z_{sl}}{\partial t} + (1 - \frac{\rho}{\rho_{sw}})(a_s - a_b). \quad (2.93)$$

If the horizontal difference of the sea level is neglected,

$$\frac{\partial h}{\partial t} = -(1 - \frac{\rho}{\rho_{sw}}) \nabla \cdot \mathbf{Q} + (1 - \frac{\rho}{\rho_{sw}})(a_s - a_b) + \frac{\partial z_{sl}}{\partial t}. \quad (2.94)$$

Note that $\nabla \cdot \mathbf{Q} = \nabla \cdot \mathbf{v}(h - b)$ when the sea level is horizontally constant. There is a problem around the grounding line when using the ice surface evolution equation. This is because, although it is valid for ice shelves, it is not clear whether the ice at the transition zone should be treated as ice sheet or ice shelf. It is therefore difficult to choose the correct calculation of mass balance around grounding lines.

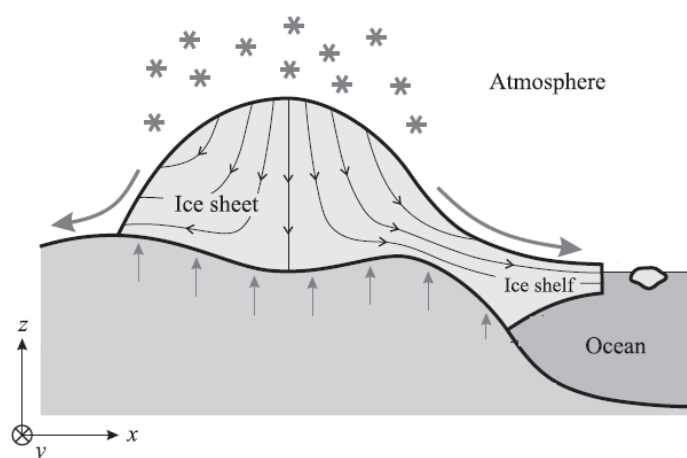


Figure 2.1: The typical state of an ice sheet. Arrows show driving forces and flow of ice, and the resisting force working on the bedrock [Greve and Blatter, 2009].

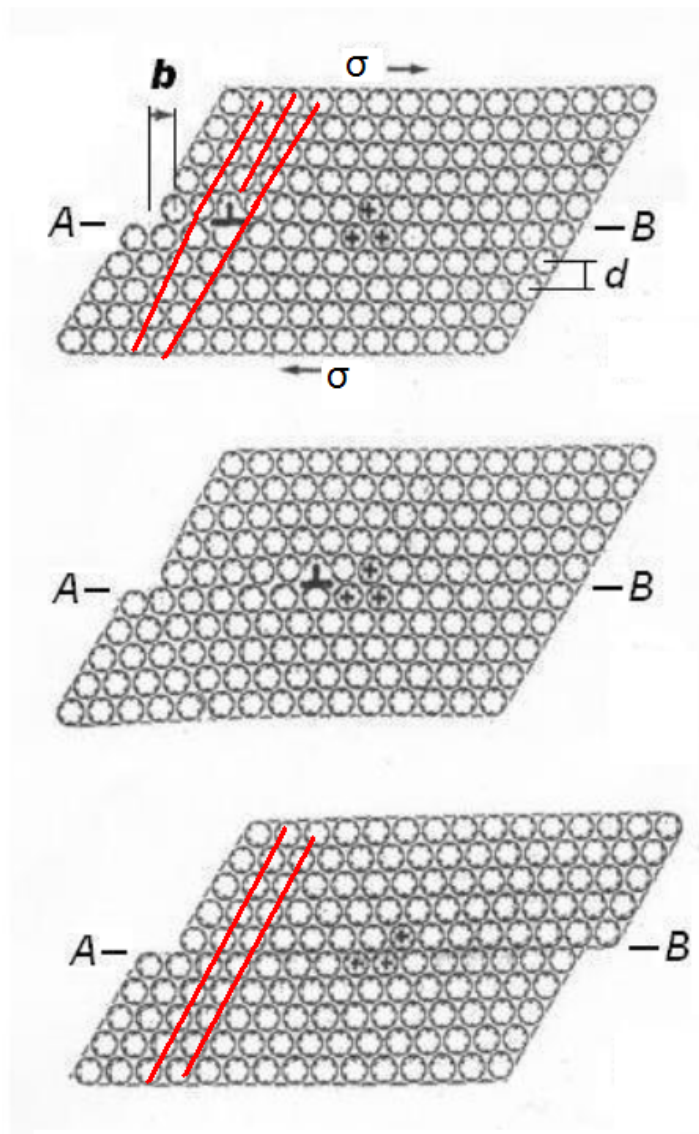


Figure 2.2: The sliding motion of the ice sheet. Where b is Burger's vector. d is the distance. σ is the internal force. The defect moves through the A-B line. The three red lines become two straight lines, then molecular movements [modified from Hondoh, 2000].

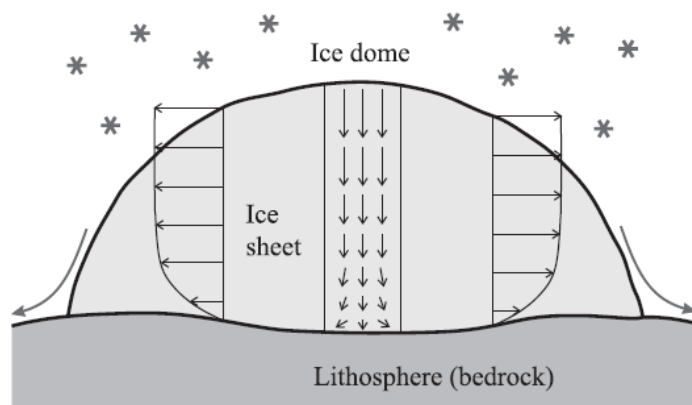


Figure 2.3: Flow regimes in an ice sheet. Simple, bed-parallel shear flow prevails except in the ice dome and margins [Greve and Blatter, 2009].

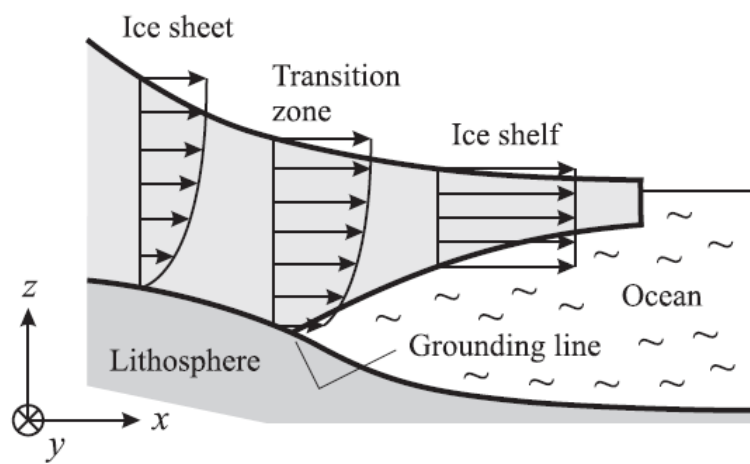


Figure 2.4: Flow regime at the ice sheet to ice shelf transition. In the grounded ice sheet shear flow prevails, whereas in the floating ice shelf, plug flow is present [Greve and Blatter, 2009].

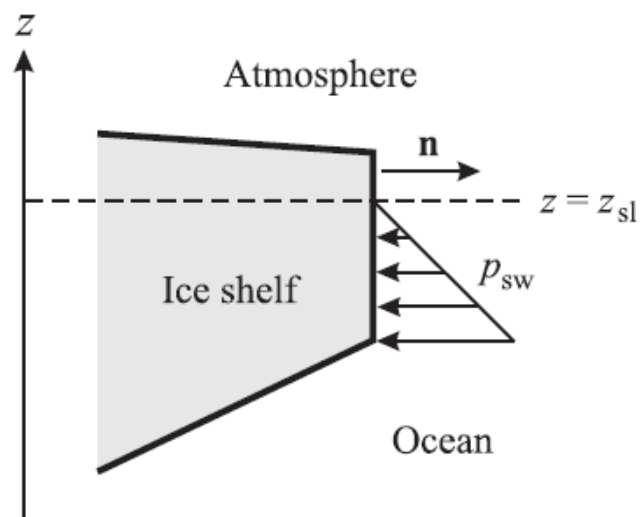


Figure 2.5: The condition of the calving front. Hydrostatic pressure acts below sea level [Greve and Blatter, 2009].

Chapter 3

Numerical methods

3.1 Ice sheet model SICOPOLIS

The ice sheet model SICOPOLIS is a 3D dynamic-thermodynamic ice sheet model constructed by Greve [1995]. The purpose of the model is to simulate large-scale ice sheet evolution with thermodynamical coupling of the ice sheet and the lithosphere. The components of the model are the dynamics of ice and of the lithosphere, the atmospheric (temperature and accumulation rates) and the oceanological boundary conditions (mean sea level and sub-ice-shelf melt) (Fig. 3.1).

A shallow ice approximation with a Weertman-type sliding law is used for the dynamics. There are several options for the constitutive equation and Glen's flow law is one of them. It is also possible to use a polythermal approach. Isostatic displacement is also applied to the lithosphere dynamics. The thermodynamics of the ice and of the lithosphere are coupled. The finite difference scheme with the Arakawa C grid [Arakawa and Lamb, 1977] is used for the field equations (Fig. 3.2). Scalar variables such as ice thickness and temperature are on the grid point and the velocities are on the staggered grid point. For the vertical layers, a sigma coordinate system, with coordinates normalized by local thickness, is applied.

3.2 Details of the numerical grid

The surface slope is a significant factor affecting ice flow. If the discretizations are done in a straightforward way, the exact positions of the ice surface are missed. Ice flow can then be over- or underestimated. Sigma coordinates are applied to the ice sheet model to represent precisely the positions of the ice surface and ice base (Fig. 3.3). A terrain-following coordinate transformation

is applied which maps the local ice thickness on to unity,

$$\xi = x,$$

$$\varphi = y,$$

$$\zeta = \frac{z - b(x, y, t)}{H(x, y, t)} \quad (3.1)$$

$$\tau = t. \quad (3.2)$$

The (x, y, z, t) coordinate system is mapped to (ξ, φ, ζ, t) coordinates. This transformation, often referred to as the sigma transformation, maps the ice surface $h = h(x, y, t)$ to $\zeta = 1$ and the ice base $b = b(x, y, t)$ to $\zeta = 0$. In the transformed domain, a regular, rectangular grid with spacings $\delta\xi$, $\delta\varphi$ and $\sigma\zeta$ can easily be defined, such that the uppermost layer of grid points matches the ice surface and the lowermost layer the ice base. It is not enough just to transform the coordinates as it is also necessary to transform the field equations,

$$\begin{aligned} \frac{\partial}{\partial x} &= \frac{\partial}{\partial \xi} + \frac{\partial \zeta}{\partial x} \frac{\partial}{\partial \zeta} \\ \frac{\partial}{\partial y} &= \frac{\partial}{\partial \varphi} + \frac{\partial \zeta}{\partial y} \frac{\partial}{\partial \zeta} \\ \frac{\partial}{\partial z} &= \frac{\partial \zeta}{\partial z} \frac{\partial}{\partial \zeta}, \\ \frac{\partial}{\partial t} &= \frac{\partial}{\partial \tau} + \frac{\partial \zeta}{\partial t} \frac{\partial}{\partial \zeta}. \end{aligned} \quad (3.3)$$

The respective derivatives are not the same.

Another treatment of the grid condition is also applied to the model. It is called the Arakawa C grid a type of staggered grid system into which numerical values can be inserted (Fig. 3.2). Scalar field variables are defined on the regular grid (ice thickness, temperature, lithosphere surface, ice surface and so on), but velocities are inserted at the mid-point of the two grid points. First, we define the regular grid:

$$\begin{aligned} \xi_i &= \xi_0 + i\Delta xi, \\ \eta_j &= \eta_0 + j\Delta y, \\ (\zeta_c)_{k_c} &= k_c/k_{c,max}, \\ (\zeta_t)_{k_t} &= k_t/k_{t,max}, \\ (\zeta_r)_{k_r} &= k_r/k_{r,max}, \\ t^n &= t^0 + n\Delta t, \end{aligned} \quad (3.4)$$

$$(3.5)$$

The velocity components v_x , v_y and v_z are inserted at the mid-point between two points on each axis.

3.3 Coupling of the ice shelf model to the ice sheet model

It is necessary to couple the ice shelf model with the ice sheet model to understand the dynamics of the ice sheet while taking the ice shelves into consideration. The ice shelf dynamics model is as follows:

Three different time steps are applied to the ice sheet model. The longest time step, Δt_l , is used in the dynamics of the lithosphere. The second, longer, step is used in the temperature evolution equation. The shortest time step is taken for the ice thickness equation.

3.4 Shallow shelf dynamic equations

The shallow shelf approximation is discretized with the staggered Arakawa C grid. The basic idea is the discretization with respect to the staggered grid point $(i + 1/2, j)$.

3.4.1 Field equations

If the staggered grid point $(i + 1/2, j)$ has two ice shelf neighbours, (i, j) and $(i + 1, j)$, then it is considered to be an ice shelf. The shallow shelf equation

for v_x is discretized to

$$\begin{aligned}
& \frac{4}{(\Delta x)^2} (\eta_{i+1,j} [(v_x)_{i+3/2,j} - (v_x)_{i+1/2,j}] - \eta_{i,j} [(v_x)_{i+1/2,j} - (v_x)_{i-1/2,j}]) \\
& + \frac{2}{\Delta x \Delta y} (\eta_{i+1,j} [(v_y)_{i+1,j+1/2} - (v_y)_{i+1,j-1/2}] - \eta_{i,j} [(v_y)_{i,j+1/2} - (v_y)_{i,j-1/2}]) \\
& + \frac{1}{\Delta x \Delta y} (\eta_{i+1/2,j+1/2} [(v_y)_{i+1,j+1/2} - (v_y)_{i,j+1/2}] \\
& \quad - \eta_{i+1/2,h-1/2} [(v_y)_{i+1,j-1/2} - (v_y)_{i,j-1/2}]) \\
& + \frac{1}{(\Delta y)^2} (\eta_{i+1/2,j+1/2} [(v_x)_{i+1/2,j} - (v_x)_{i+1/2,j}] \\
& \quad - \eta_{i+1/2,j-1/2} [(v_x)_{i+1/2,j} - (v_x)_{i+1/2,j-1}]) \\
& = \frac{\rho g}{\Delta x} H_{i+1/2,j} (h_{i+1,j} - h_{i,j}). \tag{3.6}
\end{aligned}$$

Which is applied for v_y when both neighbors of the staggered grid point $(i, j + 1/2)$, (i, j) and $(i, j + 1)$, are ice shelves,

$$\begin{aligned}
& \frac{4}{\Delta y^2} (\eta_{i,j+1} [(v_y)_{i,j+3/2} - (v_y)_{i,j+1/2}] - \eta_{i,j} [(v_y)_{i,j+1/2} - (v_y)_{i,j-1/2}]) \\
& + \frac{2}{\Delta x \Delta y} (\eta_{i,j+1} [(v_x)_{i+1/2,j+1} - (v_x)_{i-1/2,j+1}] - \eta_{i,j} [(v_y)_{i+1/2,j} - (v_y)_{i-1/2,j}]) \\
& + \frac{1}{\Delta x \Delta y} (\eta_{i+1/2,j+1/2} [(v_x)_{i+1/2,j+1} - (v_x)_{i+1/2,j}] \\
& \quad - \eta_{i-1/2,h+1/2} [(v_x)_{i-1/2,j+1} - (v_x)_{i-1/2,j}]) \\
& + \frac{1}{\Delta x^2} (\eta_{i+1/2,j+1/2} [(v_y)_{i,j+1/2} - (v_y)_{i+1/2,j}] \\
& \quad - \eta_{i-1/2,j+1/2} [(v_y)_{i,j+1/2} - (v_y)_{i-1,j+1/2}]) \\
& = \frac{\rho g}{\Delta y} H_{i,j+1/2} (h_{i,j+1} - h_{i,j}). \tag{3.7}
\end{aligned}$$

3.4.2 Calving front conditions

The shallow shelf approximation for the calving front is applied if the grid is on the ice sheet but the next point is the ocean. The calving front condition

is applied,

$$\begin{aligned}
& \frac{4\eta_{i,j}}{\Delta x} [(v_x)_{i+1/2,j} - (v_x)_{i-1/2,j}] + \frac{2\eta_{i,j}}{\Delta x} [(v_y)_{i,j+1/2} - (v_y)_{i,j-1/2}] \\
& \quad = \frac{\rho g}{2\rho_{sw}} (\rho_{sw} - \rho) H_{i,j}^2. \\
& \frac{4\eta_{i,j}}{\Delta y} [(v_y)_{i,j+1/2} - (v_y)_{i,j-1/2}] + \frac{2\eta_{i,j}}{\Delta x} [(v_x)_{i+1/2,j} - (v_x)_{i-1/2,j}] \\
& \quad = \frac{\rho g}{2\rho_{sw}} (\rho_{sw} - \rho) H_{i,j}^2. \quad (3.8)
\end{aligned}$$

It is presumed that ice fills the whole of a grid and does not leak; the calving front is perpendicular to each axis.

3.4.3 Grounding zone

Since the ice sheet model uses a staggered grid (Arakawa C grid), there is no ice thickness information at the points where velocity is defined. There are several possible ways of treating this condition.

One way is for the mid point of the ice sheet and ice shelf to be treated as an ice shelf. However, this causes a large ice flux into the sea because the velocity calculated for ice shelves is greater than that calculated for ice sheets. Moreover, because the slope for the ice sheet is steeper than for the ice shelf, the velocity simulated with the shallow shelf approximation becomes large. The rate of grounding line migration then increases. An alternative is for the point to be treated as an ice sheet. It saves ice shelves from the flux above but the rate of grounding line migration can be too slow. The third possible way of treating this condition is to check the conditions of the middle point. The floating conditions of the staggered grid are linearly estimated by using neighboring ice thickness data,

$$\begin{aligned}
H_{i+1/2,j} &= \frac{H_{i+1,j} + H_{i,j}}{2}, \\
H_{i,j+1/2} &= \frac{H_{i,j+1} + H_{i,j}}{2}. \quad (3.9)
\end{aligned}$$

If the estimated ice thickness is lower than the floating thickness, then it is treated as an ice shelf. Otherwise, it is treated as an ice sheet. Then, one point further downstream on the grid is the ice shelf.

Pollard and DeConto [2009] compared the simulated flux of the middle point with the flux estimated from 2D boundary layer theory. If the flux estimated by the boundary layer theory is larger than the flux calculated by the large scale ice shelf model, the solution of boundary layer theory is

applied to that point. Otherwise, the boundary layer flux is imposed on the point one step downstream. Such treatment can improve the fit around the grounding zone.

It is difficult to define the basal mass balance at the grounding line, the grid next to an ice shelf. Although the grounding line point is not floating, it is affected by the sea since it is next to an ice shelf. The simple way to determine melt rates is just to use the ocean-induced melting when the base of the ice is lower than sea level,

$$a_b = m_m. \quad (3.10)$$

It is a good approximation when ocean-induced mass balance is dominant.

In another way, the basal mass balance depends on the number of ice shelf domains next to the grounding line,

$$r_g = \frac{N_{gr}}{N_{all}}, \quad (3.11)$$

where r_g is the ratio of the grounded grid number, N_{gr} , to the total of grids next to the grounding line, N_{all} . The total basal mass balance is

$$a_b = r_g m_m + (1 - r_g) m_g, \quad (3.12)$$

where m_g is melt rate when the point is grounded, estimated by the geothermal flux and strain heating of ice.

There is another option which depends on depth. In reality, the grounding line itself meets the floating condition. However, the numerical grounding line point can be deeper or shallower than the ice sheet. If the elevation of its base is not deep enough to satisfy the floating condition, the effect of the ocean is limited. The ocean-induced basal mass balance is determined by its depth relative to the floating condition;

- when the ice base is above sea level,

$$a_b = m_g, \quad (3.13)$$

- when the base is below sea level,

$$b_{gl} = m_m \left(\frac{H}{z_{sl} - b} \frac{\rho_{sw}}{\rho} \right) + m_g \left(1 - \frac{H}{z_{sl} - b} \frac{\rho_{sw}}{\rho} \right). \quad (3.14)$$

3.5 Temperature evolution

The temperature evolution equation is not very different from that used for the ice sheet. The differences are the strain heating and the basal boundary condition.

The strain heating term is calculated where viscosity is calculated. Therefore, the value is implemented for the temperature evolution equation. For the basal boundary condition, a temperature two degrees above the melting point is applied as the boundary condition.

3.6 Topography evolution

The margin of the glacier changes through flow and accumulation. There are several ways to manage ice sheet topography evolution. One of the traditional ways is the ice surface equation and another is the ice thickness equation.

3.6.1 Ice surface equation

The ice surface evolution equation was applied initially. However, it may not conserve mass balance in the vicinity of the grounding lines. The neighbor of a grid point at the grounding line is on the ice shelf. The ice surface equation for the ice sheet is used for the grid and the equation for the ice shelf is applied to the neighbors. But it is not known whether the grid will still be ice sheet or ice shelf in the next time step.

The ice surface equation is

$$\begin{aligned} \frac{h_{i,j}^{n+1} - h_{i,j}^n}{\Delta t} = & - \left(v_x \frac{\partial h}{\partial x} \right)_{up} - \left(v_y \frac{\partial h}{\partial y} \right)_{up} \\ & - H_{i,j}^n \frac{(v_x)_{i+1/2,j} - (v_x)_{i-1/2,j}}{\Delta x} \\ & - H_{i,j}^n \frac{(v_y)_{i,j+1/2} - (v_y)_{i,j-1/2}}{\Delta y} \\ & + a_s - a_b + \frac{b_{i,j}^{n+1} - b_{i,j}^n}{\Delta t}. \end{aligned} \quad (3.15)$$

where the upstream term for the staggered grid has two parts. One example for the x direction is

$$\left(v_x \frac{\partial h}{\partial x} \right)_{up} = - \left((v_x)_{i+1/2,j} \frac{h_{i+1,j} - h_{i,j}}{\Delta x} \right)_{up} + \left((v_x)_{i-1/2,j} \frac{h_{i,j} - h_{i-1,j}}{\Delta x} \right)_{up}. \quad (3.16)$$

Then, the right hand side is

$$\left((v_x)_{i+1/2,j} \frac{h_{i+1,j} - h_{i,j}}{\Delta x} \right)_{up} = \begin{cases} (v_x)_{i+1/2,j} \frac{h_{i+1,j} - h_{i,j}}{\Delta x} & \text{if } (v_x)_{i+1/2,j} < 0, \\ 0. & \text{if } (v_x)_{i+1/2,j} \geq 0. \end{cases} \quad (3.17)$$

$$\left((v_x)_{i-1/2,j} \frac{h_{i,j} - h_{i-1,j}}{\Delta x} \right)_{up} = \begin{cases} (v_x)_{i-1/2,j} \frac{h_{i,j} - h_{i-1,j}}{\Delta x} & \text{if } (v_x)_{i-1/2,j} \geq 0, \\ 0 & \text{if } (v_x)_{i-1/2,j} < 0. \end{cases} \quad (3.18)$$

3.6.2 Ice thickness equation

As stated above, the ice thickness equation is good for estimating mass conservation. Therefore, attempts have been made to apply it to ice shelves as well. The ice thickness equation is

$$\begin{aligned} \frac{H_{i,j}^{n+1} - H_{i,j}^n}{\Delta t} = & - \left(v_x \frac{\partial H}{\partial x} \right)_{up} - \left(v_y \frac{\partial H}{\partial y} \right)_{up} \\ & - H_{i,j}^n \frac{(v_x)_{i+1/2,j} - (v_x)_{i-1/2,j}}{\Delta x} \\ & - H_{i,j}^n \frac{(v_y)_{i,j+1/2} - (v_y)_{i,j-1/2}}{\Delta y} + a_s - a_b. \end{aligned} \quad (3.19)$$

The upstream term is the same as the ice surface equation.

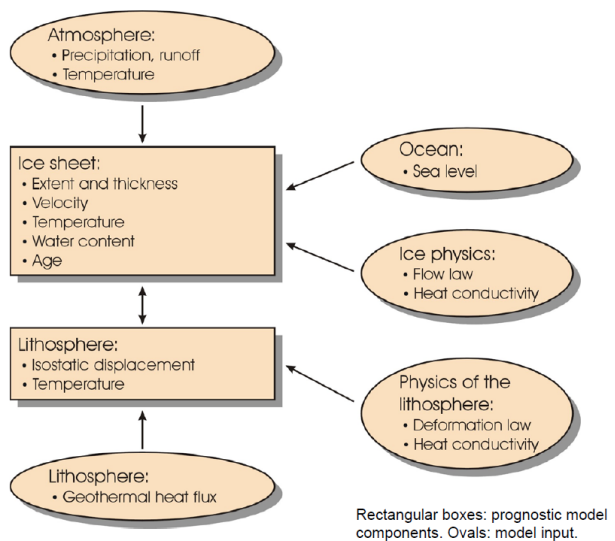


Figure 3.1: Components of the ice sheet model, SICOPOLIS.

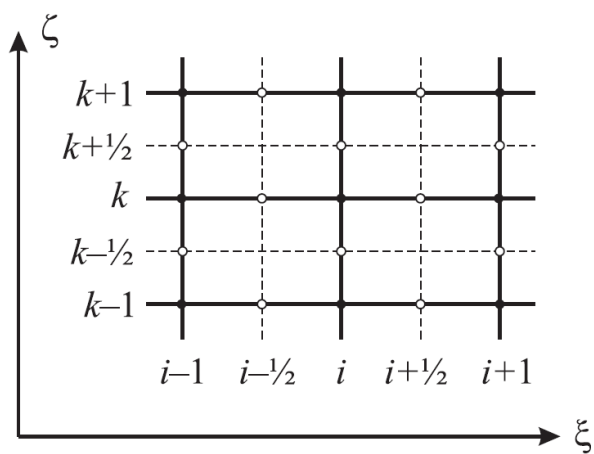


Figure 3.2: The Arakawa C grid is a numerical grid system defined by Arakawa and Lamb [1977].

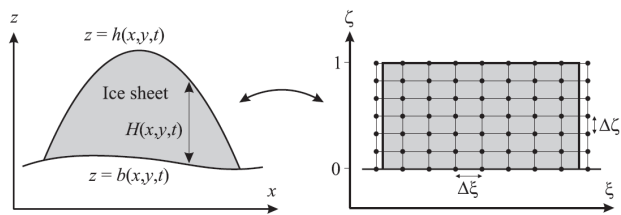


Figure 3.3: The sigma coordinate system of the ice sheet [Greve and Blatter, 2009].

Chapter 4

Numerical tests

4.1 Ice shelf ramp

The performance of the shallow shelf model was tested for the case of an ice shelf ramp for which an analytical solution exists [Greve and Blatter, 2009]. The analytical solution is given in two-dimensional flow in the $x - z$ plane, where x is the direction of flow and z is positive upward (Fig. 4.1). The length of the shelf is L . The grounding line lies at $x = 0$, the calving front lies at $x = L$. Ice thickness declines linearly from $H = H_{gl}$ at the grounding line to $H = H_{cf}$ at the calving front,

$$H = H_{gl} - \frac{H_{gl} - H_{cf}}{L}x. \quad (4.1)$$

With the floating condition, the ice surface and the ice base are given by

$$h = \frac{\rho_{sw} - \rho}{\rho_{sw}} H, b = -\frac{\rho}{\rho_{sw}} H. \quad (4.2)$$

The rate factor of the constitutive equation is a constant, $A(T, p) = A = const.$ The analytical solution for the ice shelf ramp is

$$v_x(x) = v_{gl} + \left(\frac{\rho g}{4}\right)^n A \int_0^x H^n(x) dx, \quad (4.3)$$

where n is the exponent of Glen's flow law.

Since the ice shelf model has both x - y horizontal dimensions, the direction needs to be set perpendicular to the flow (y direction). In the ice shelf ramp experiment, ice thickness is constant through y direction, i.e. $(\partial H / \partial y = 0)$ and the width was set wide enough to eliminate the effect of the side wall. Finally, it has a rectangular domain with x (the flow direction) and y (the

transverse direction). The solution through the central flow line will be the same as the original two-dimensional setting. Mean sea level is $z = z_{sl} = 0$. Incoming ice flow velocity at the grounding line is $\mathbf{v}_{gl} = v_{gl}\mathbf{e}_x$, i.e., the incoming ice flux of the shelf is $v_x H_{gl}$. The velocity at the side wall ($y = 0$ and $y = y_{max}$) is zero. The ice shelf is set at a steady state, $\partial/\partial t = 0$, for all variables. The input velocity at the grounding line is $v_{gl} = 100 \text{ m/a}$. Ice thickness at the grounding line and the calving front is $H_{gl} = 400 \text{ m}$, $H_{cf} = 200 \text{ m}$. The length of the shelf is $L = 200 \text{ km}$. The rate factor is $A = 4.9 \times 10^{-25} \text{ s}^{-1} \text{ Pa}^{-3}$.

The velocity map of the experiment shows that the field is symmetrical about the central flow line and is fastest at the central flow line, where the effect of the side wall is negligible (Fig. 4.2). The velocity through the central flow line nicely reproduced the analytical solution (Fig. 4.3).

4.2 Shelfy stream experiments

The performance of the shelfy stream model was also tested. The rectangular domain is also used in this test. The length of the ice shelf is $L_{sh} = 100 \text{ km}$ in the x direction. The length of the stream upstream from the ice shelf is $L_{st} = 50 \text{ km}$ (Fig. 4.4a). The ice thickness is $H_{in} = 400 \text{ m}$ at the initial point, $H_{gl} = 300 \text{ m}$ at the grounding line and $H_{cf} = 200 \text{ m}$ at the calving front. The ice thickness profile is

$$\begin{aligned} H(x)_{st} &= H_{in} - x \frac{H_{in} - H_{gl}}{L_{st}} \quad (x \leq 50 \text{ km}) \\ H(x)_{sh} &= H_{gl} - x \frac{H_{gl} - H_{cf}}{L_{sf}} \quad (50 < x \leq 150 \text{ km}). \end{aligned} \quad (4.4)$$

The basal flow law is set the same as Schoof [2007a]. The result indicates that the velocity is relatively fast, more than 1 km/a, even around grounded ice stream areas. The velocity is accelerated to 3 km/a near the calving front.

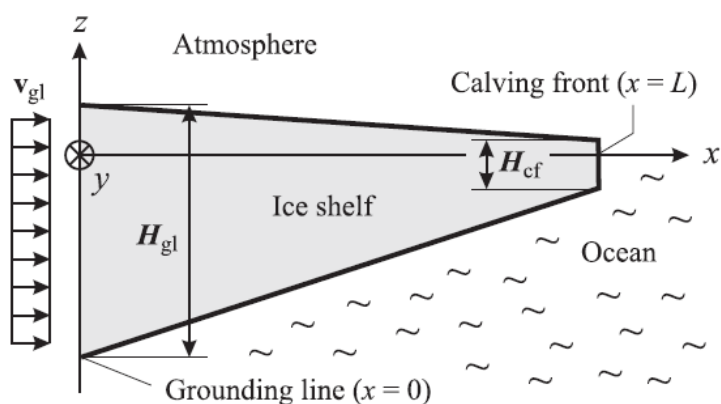


Figure 4.1: The profile of the ice shelf ramp [Greve and Blatter, 2009].

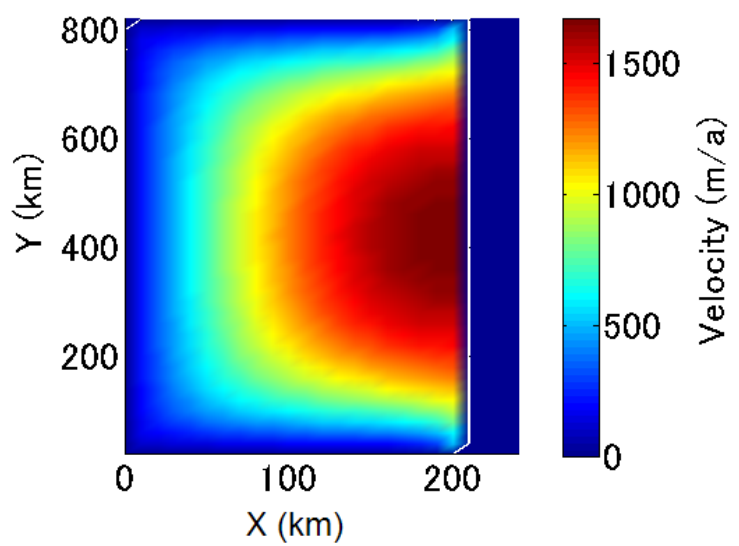


Figure 4.2: The condition of the 3D ice shelf ramp.

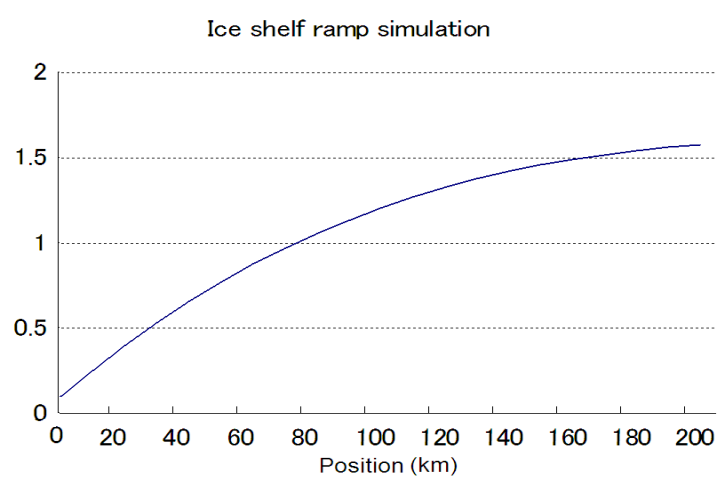


Figure 4.3: The result for the central flow line of the 3D ice shelf ramp.

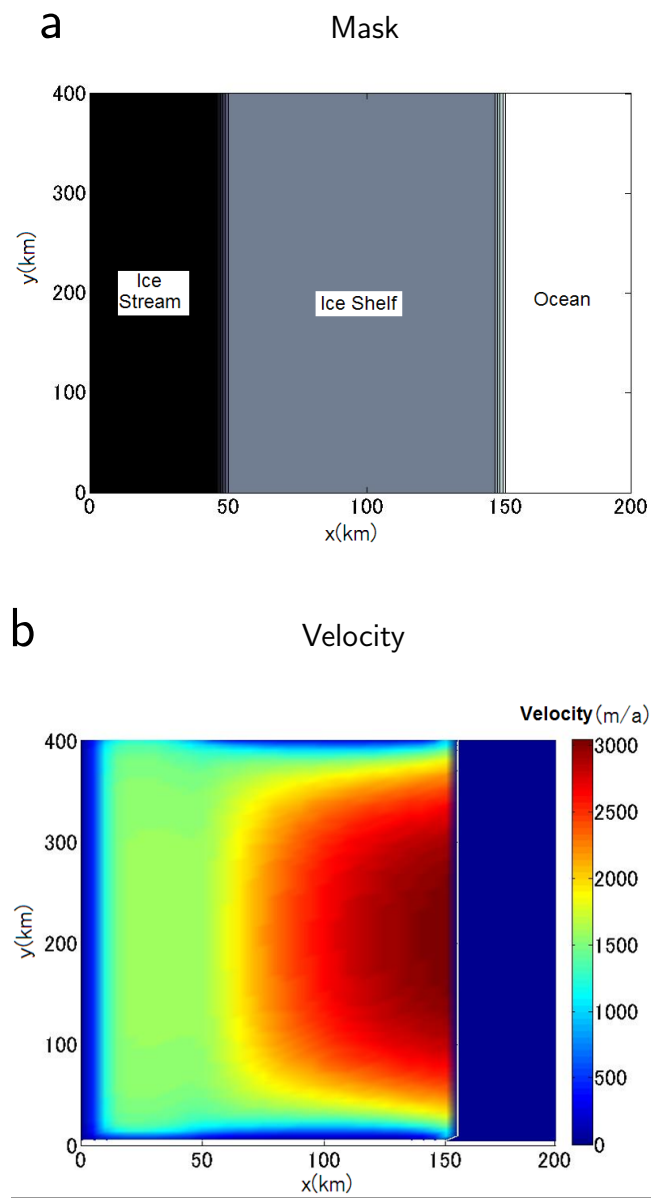


Figure 4.4: The setting of the ice stream region and the ice shelf region and the result of the shelfy stream run.

Chapter 5

SeaRISE experiments

5.1 SeaRISE

As stated in Chapter 1, it is unclear how much ice sheet instabilities contribute to sea level rise. It is therefore necessary to quantify how sensitive ice sheets are to several causes of instability.

Sea-level Response to Ice Sheet Evolution (SeaRISE) is a community-organized effort to estimate the likely range of ice sheet contributions to sea level change over the next few hundred years. Common datasets for the ice sheet study have been developed in the project. The numerical experiments are conducted by using SeaRISE datasets (Fig. 5.1). Several types of experiments are being designed within the project.

5.2 Application of the model to the SeaRISE set-up

After the model is validated, it is coupled to the ice sheet model. The model is applied to the Antarctic ice sheet with the SeaRISE dataset. The geometry of the experiment is developed by the SeaRISE project; ice thickness, the bedrock topography, accumulation rates, ice surface and the mask of floating ice and grounded ice. The parametrization of current surface temperature is taken from Fortuin and Oerlemans [1990],

$$T_{\text{ma}} = \begin{cases} 7.405 - 0.014285 h - 0.180 \phi, & \text{for } h > 1500 \text{ m}, \\ 36.689 - 0.005102 h - 0.725 \phi, & \text{for } 200 \text{ m} < h \leq 1500 \text{ m} \\ 49.642 - 0.943 \phi, & \text{for } h \leq 200 \text{ m}, \end{cases} \quad (5.1)$$

$$T_{\text{ms}} = 16.81 - 0.00692 h - 0.27937 \phi, \quad (5.2)$$

where temperatures are in $^{\circ}\text{C}$, surface elevations in m AMSL and latitudes in $^{\circ}\text{S}$ (counted positive).

The calving criterion thickness is applied in this study. The threshold value is 200 m in some simulations. There are considerable areas of ice shelf that are thinner than this value (Fig. 5.2). The Riiser-Larsen and Shackleton ice shelves, in particular, lose large areas with a larger threshold of 200–250 m than many of the smaller ice shelves. Moreover, using a large value of threshold thickness prevents a new ice shelf grid being made. Therefore, another threshold value, 50 m, was used in most runs.

5.3 Paleoclimatic spin-up

In order to obtain a suitable present-day configuration of the Antarctic ice sheet, it is desirable to carry out a paleoclimatic spin-up over at least a full glacial cycle. The simulated present-day configuration of the ice sheet is used as the initial conditions for simulation of the effects of future climate described below. Initial testing revealed that it is very difficult to reproduce the observed geometry (in particular the distribution of grounded vs. floating ice) by an unconstrained, freely evolving simulation. For this reason, we carried out the spin-up simulation in three steps (Fig. 5.3): (i) an initial relaxation run with freely evolving grounded ice topography over 100 years (starting from the present-day geometry and isothermal conditions at -10°C everywhere) in order to avoid spurious noise in the computed velocity field [Calov, 1994]; (ii) a steady-state run from 250 ka BP to 125 ka BP with the topography kept fixed over time and the climatic forcing kept steady at 125 ka BP conditions; (iii) a transient run from 125 ka BP to today with the topography kept fixed over time in order to enforce a good fit between the simulated and observed present-day topographies [see also Seddik et al., 2012].

The mean annual and mean summer surface temperatures (T_{ma} and T_{ms} , respectively) are decomposed into present-day spatial distributions plus a purely time-dependent anomaly $\Delta T(t)$,

$$\begin{aligned} T_{\text{ma}}(h, \phi, t) &= T_{\text{ma}}^{\text{present}}(h, \phi) + \Delta T(t), \\ T_{\text{ms}}(h, \phi, t) &= T_{\text{ms}}^{\text{present}}(h, \phi) + \Delta T(t), \end{aligned} \quad (5.3)$$

where t is time and ϕ geographical latitude. The time-dependent anomaly $\Delta T(t)$ results from the Vostok deuterium isotope ratio record converted to temperature with the relation of Petit et al. [1999]. Precipitation, surface melting and sea level forcing are irrelevant here due to the fixed topography approach. The paleoclimatic spin-up is conducted with such conditions.

The SeaRISE Antarctica Developmental Data Set provides two different distributions of geothermal heat flux by Shapiro and Ritzwoller [2004] and Fox Maule et al. [2005] (Fig. 5.4). We conducted the spin-up run with both datasets with heat flux values capped at 70 mW m^{-2} following a recommendation from the SeaRISE project.

Although several different resolutions were tried, the results at 20 km resolution are discussed here. The basal temperature results (Fig. 5.5a) are at the pressure melting point in large areas in West Antarctica, while limited temperature base areas are found in East Antarctica, in George V Land, Wilkes Land and several other places near the coast. At the deep ice core sites Vostok, Dome C, Dome F, Kohnen and Byrd, the spin-up run produces basal temperatures of -11.4°C , -11.6°C , -18.4°C , -11.3°C and -2.0°C (pressure melting point), respectively. Except for Byrd, these temperatures are significantly below the pressure melting point, while the observed temperatures all reach the pressure melting point. This discrepancy is probably due to the shortcomings of the Shapiro and Ritzwoller [2004], geothermal heat flux distribution that was applied which gives values in the range of $45-50 \text{ mW m}^{-2}$ at Dome C, Dome F and Vostok. This is probably not sufficient to form a temperate base [Llubes et al., 2006]. Seddik et al. [2011] used a higher geothermal heat flux of 60 mW m^{-2} to produce a realistic borehole temperature in the vicinity of Dome F. Therefore, larger geothermal heat fluxes would be needed to reproduce the melting conditions that have been observed in East Antarctica. By contrast, the base of the West-Antarctic Byrd ice core, which receives a geothermal heat flux of 70 mW m^{-2} in our simulation, reaches the melting point. The basal temperature is high at EAIS in the Fox Maule et al. [2005] spin-up. However, the WAIS is colder in these experiments.

5.4 Sensitivities of the ice volume to different datasets

Since there are two different sets of input data of geothermal heat flux and accumulation rates (Fig. 5.4, Fig. 5.6), it is preferable to estimate the effect of using these different datasets. The sensitivities to the input dataset were estimated. There are four different combinations,

1. Shapiro and Ritzwoller [2004] geothermal heat flux (SR) and Arthern et al. [2006] (AE) accumulation rate
2. SR geothermal heat flux and Van de Berg et al. [2006] (BE) accumulation rate

3. Fox Maule et al. [2005] geothermal heat flux (FE) and AE accumulation rate
4. FE geothermal heat flux and BE accumulation rate.

Two different paleoclimatic spin-ups were carried out to accommodate the two different geothermal flux datasets. The four experiments were conducted from the end of spin-up and calculated over 500 years. Figure 5.7 shows the evolution of the grounded ice volume for the future control run with the two different sets of accumulation data (Section 5.5). In both cases, the ice volume increases by more than 1.5 m SLE over 500 years, and the accumulation data from Van de Berg et al. [2006] produce ~ 35 cm SLE more ice than those from Arthern et al. [2006].

The reason is that the former accumulation rates are relatively larger than the latter, particularly around the margin of ice sheets such as the Antarctic Peninsula and the margins of East Antarctica. By contrast, different geothermal flux settings (Shapiro and Ritzwoller [2004] vs. Fox Maule et al. [2005]) cause only slight changes. It was finally decided to use the SR geothermal flux and AE accumulation rates for the control run.

5.5 Future climate experiments

The results of the paleoclimatic spin-up run for the present are shown in Fig. 5.8. Due to the fixed-topography approach, the surface topography is of course very similar to that observed (not shown). Small differences of the order of tens of meters arise as a consequence of the initial 100-year relaxation. The surface velocity shows the expected distribution with small velocities (< 10 m a $^{-1}$) in the interior, a general speed-up towards the coast and the largest velocities of 1000 m a $^{-1}$ and more for the ice shelves. The simulated velocity patterns nicely reproduce the observed velocity pattern.

The experiment on future climate was started from the end of spin-up (2004) and simulated hundreds of years with varied boundary conditions. For the future climate experiments we used the following set of SeaRISE experiments:

- Experiment C1: constant climate control run; beginning at present (more precisely, 2004-1-1 0:00, corresponding to $t = 0$) and running for 500 a holding the climate steady at present climate values. We carried out this run alternately with the surface accumulation data from Arthern et al. [2006] and Shapiro and Ritzwoller [2004] geothermal flux (as provided in the Antarctica Developmental Data Set by SeaRISE).

- Experiment C2: AR4 climate forcing running for 500 a.
- Experiment C3: 1.5 times AR4 climate forcing running for 500 a.
- Experiment C4: 2.0 times AR4 climate forcing for 500 a.
- Experiment M0: constant climate forcing running for 500 a, AE surface accumulation rates, zero sub-ice-shelf melting rate.
- Experiment M1: constant climate forcing running for 500 a, AE surface accumulation rates, uniform sub-ice-shelf melting rate of $2 \text{ m ice equiv. a}^{-1}$.
- Experiment M2: constant climate forcing running for 500 a, AE surface accumulation rates, uniform sub-ice-shelf melting rate of $20 \text{ m ice equiv. a}^{-1}$.
- Experiment M3: constant climate forcing running for 500 a, AE surface accumulation rates. uniform sub-ice-shelf melting rate of $200 \text{ m ice equiv. a}^{-1}$.
- Experiment S1: the basal sliding velocity is doubled. Constant climate forcing running for 500 a, AE surface accumulation rates.
- Experiment S2: the basal sliding velocity is increased by a factor of 2.5. Constant climate forcing running for 500 a, AE surface accumulation rates.
- Experiment S3: the basal sliding velocity is increased by a factor of 3. Constant climate forcing running for 500 a, AE surface accumulation rates.
- Experiment T1: the basal sliding velocity is doubled. AR4 climate forcing running running for 500 a, AE surface accumulation rates. A uniform sub-ice-shelf melting rate of $20 \text{ m ice equiv. a}^{-1}$.

For all experiments, the geothermal heat flux is that of Shapiro and Ritzwoller [2004], capped at 70 mW m^{-2} (the same as used for the paleoclimatic spin-up, see above).

5.6 Sensitivities on varied sub-ice-shelf melting rates

The model was applied to the diagnostic condition. The resolution is 40 km. The number of nodes is 150×150 for the horizontal directions, and 80 for the

vertical direction. The total number is $150 = 1,800,000$. The ice temperature was set to -10°C . The results show that inland ice volume decreases when basal melt rates increase (see Fig. 5.9). The basal pressure reduction by basal water pressure was neglected. This is caused by the reduction of buttressing from ice shelves, as stated above. On the other hand, if ice shelves disappear, land ice volume subsequently increases. The reason for increased ice volume is changes in boundary conditions. In this simulation, melting around the marine ice margin is not included. After ice shelf removal due to enhanced melting, ocean induced melting disappears from the last grounding line. Therefore, volume loss is smaller than when ice shelves exist. Moreover, velocities in ice shelves are higher than those in the ice sheet since there is no friction under ice shelves. The disappearance of ice shelves reduces the flux of ice away from the land ice. This effect and reduction of buttressing causes the changes in land ice volume.

Another experiment was carried out with melting marine ice margins. The basal pressure reduction by basal water pressure is also included (Fig. 5.10). In this case, ice volume of the M3 experiment is smaller than in M2. But the difference is less than 0.1 mm sea level equivalent in 100 years and less than 0.2 mm sea level equivalent in 500 years. It suggests there is a limitation of ice volume change by ocean induced melting.

The results of simulations of the effect of future climate change of M0-M3 setting in 20 km resolution are shown in Fig. 5.11. As expected, grounded ice volume declines when basal melting rates are higher. However, the effect is strongly non-linear and diminishes with increasing melting rates. This agrees with the findings of Huybrechts and de Wolde [1999] for a similar series of simulations with smaller basal melting rates of 0, 1, 3, 5 and 10 m a^{-1} . The range of ice volume changes across all experiments is $\sim 0.5 \text{ m SLE}$ after 100 years and $\sim 1.5 \text{ m SLE}$ after 500 years. We thus see a significant, but not catastrophic, impact of increased basal melting (up to 200 m a^{-1} !) on ice sheet decay.

The changes in the area of grounded and floating ice are shown in Fig. 5.12. In the control run (basal melting according to Eq. (2.86)), the grounded ice area grows rapidly by $\sim 0.2 \times 10^6 \text{ km}^2$ at the expense of floating ice, and remains relatively constant after that. This increased area of grounded ice also explains the increase in grounded ice volume discussed above. In the extreme run M3 (200 m a^{-1} basal melting), current floating ice disappears almost entirely within a few years. The area of grounded ice remains largely unaffected but, as seen above, the loss of ice shelf buttressing leads to a significant loss of ice volume compared to the control run. In the M2 experiment (20 m a^{-1} basal melting), most of the floating ice disappears within 100 years. However, the remaining area of floating ice stabilizes at $\sim 0.2 \times 10^6 \text{ km}^2$ due

to a balance between inflow from the ice sheet and basal melting.

In general, under the influence of high basal melting, the Ross and Antarctic Peninsula ice shelves decay faster than the Filchner-Ronne and Amery ice shelves. In the M1 experiment (2 m a^{-1} basal melting), the Ross ice shelf loses more than 50% of its area by $t = 250$ a and almost disappears by $t = 500$ a, while the Amery ice shelf does not lose much of its area. The vulnerability of the Ross ice shelf results from the fact that it is surrounded by the Transantarctic Mountains so that the incoming flux from the ice sheet is smaller than for other ice shelves. By contrast, the Amery ice shelf is largely stabilized against increased basal melting by the large inflow from the Lambert Glacier, which is the world's largest glacier. As expected, shrinkage of the WAIS was larger than that of the EAIS due to the bedrock topography (Fig. 5.13).

The grounded ice area is largest in run M0 (no basal melting), while the floating ice area is largest in the control run (basal melting according to Eq. (2.86)). This is related to grounding line migration. Since there is no basal melting in run M0, the grounding lines can advance freely all around the ice sheet, so that grounded ice grows at the expense of floating ice. By contrast, basal melting favours grounding line retreat, so that floating ice grows at the expense of grounded ice. The floating ice area of run M1 (2 m a^{-1} basal melting) is larger than that of the control run during the first ~ 50 years, and larger than that of run M0 (no basal melting) during the first ~ 110 years. However, the retreat of the calving fronts due to basal-melt-induced thinning later outweighs this effect, so that the floating ice area of run M1 is ultimately smaller than that of the control and M0 runs. For runs M2 and M3 ($20 / 200 \text{ m a}^{-1}$ basal melting), basal melting is so large that the loss due to calving rapidly outweighs the gain due to grounding line retreat.

5.7 Results of whole set of SeaRISE experiments

The whole set of experiments was conducted in 10 km resolution. The ice sheet volume is most sensitive to the M-series experiments (Fig. 5.14). The next level of sensitivity is to the S-series experiments. The C-series experiments caused less change than the others. Ice volume decrease is largest in T1. The total ice volume ranges from 1.3 m SLE after 100 years to 3.3 m SLE after 500 years. In the M-series experiment, the difference in ice volume is 0.7 m SLE after 100 years and 2.6 m SLE after 500 years. In the S-series experiment, it is 0.4 m SLE after 100 years and 1.1 m SLE after 500 years.

In the C-series experiment, it is 0.15 m SLE after 100 years and 0.2 m SLE after 500 years.

Ice shelf area is sensitive to basal melting (Fig. 5.15). Since changes caused by the M1-M3 experiments are large, the timing of total ice volume change is the same as for the change in ice shelf area. Ice shelf area reaches a steady state after 10 years (M3) and 70 years (M2). A steady state is not reached within 500 years in the M1 experiment. The ice sheet volume of S2 is larger than S1 in 200-500 years (Fig. 5.16). The grounded ice area of S1 is smaller than the grounded ice sheet area of other experiments. The ice shelf area increased in S1. The reason why ice volume in S1 is smaller than in S2 is that the loss of grounded ice area means loss of land ice regions. Therefore, the total outgoing flux from the ice sheet is larger in S1 than S2. Although grounded ice area decreased in the C-series experiment (Fig. 5.17), enhanced accumulation through surface climate change increased its mass. The area of grounded ice increased after 100 years due to grounding line migration. However, ice volumes of C4 and C3 were smaller than in C1 at 500 years. This was caused by increased surface melting around the ice sheet margins in C3 and C4 compared to C1 experiments.

5.8 Relaxation of the initial shock

There are abrupt changes of ice shelf and ice sheet area in the first steps of simulation, after the fixed topography spin-up (cf. Fig. 5.12). There are several reasons for this effect. Ice sheet evolution is allowed for the first step of the spin-up. Although the grounding line and ice shelf thickness are fixed, a certain amount of ice is dammed around the grounding line during this period. This dammed ice immediately transfers to the grounding zone after topographical evolution is allowed. It causes the abrupt grounding line migration at the first step of the simulation. It changes rapidly in the first year. It also shows the fast response of the grounding line change. Although the change becomes moderate after that, it can continue for decades.

Since such rapid change is not desirable, another process is added before starting any runs. After the fixed topography spin-up, 20 years of ice sheet and ice shelf topography evolution was added. The first abrupt changes of ice sheet and ice shelf area were completed during this period. [Figure of ice shelf, sheet area in 20 years added]. In this experiment, sub-ice-shelf melting rates in the control run are doubled except for the outer ocean condition. The results of the new control run and M-series experiments are shown in Fig. 5.18. The initial abrupt change in floating ice area and grounded area is not found in this simulation. The new runs also consider marine ice melting.

The comparison of marine ice melting with no marine melting experiment shows the importance of this setting. Since this process was not included in the simulations, the Antarctic ice sheet does not lose enough mass by grounding line migration. The sea level equivalent ice volume change is almost 1.5 times larger (2.2 m SLE) than the experiment without marine ice melting (1.5 m SLE). This agrees with the spread of $0.6 \times 10^6 \text{ km}^3$ (1.5 m SLE) reported by Huybrechts and de Wolde [1999].

Changes in the area of grounded and floating ice are shown in Fig. 5.18. In the control run, the grounded ice area drops by $\sim 0.25 \times 10^6 \text{ km}^2$ ($\sim 2\%$) during the first 200 years, partly compensated by an increase in floating ice, and remains almost constant after that. In run M1 (2 m a^{-1} basal melting everywhere), grounded ice evolves very similarly due to the identical melting rates in the vicinity of the grounding line, whereas two thirds of the floating ice disappears over 500 years as a consequence of the 10 times higher melting rate over the continental shelf. For E1b most of it melts within 100 years, the remaining area stabilizing at $0.15 \times 10^6 \text{ km}^2$ (10% of today's value) due to a balance between inflow from the ice sheet and basal melting, and for E1c almost all floating ice disappears within a few years.

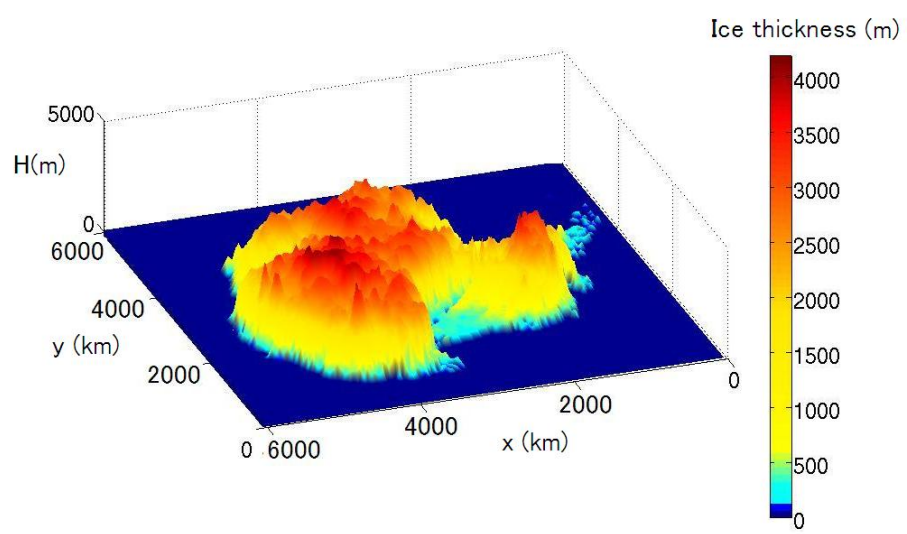


Figure 5.1: Ice thickness data used by the SeaRISE project.

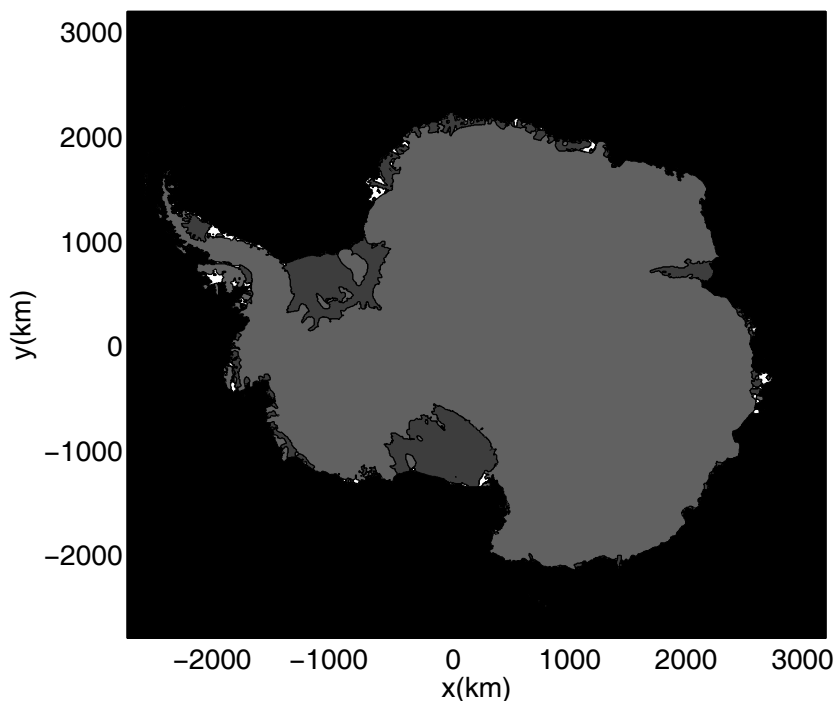


Figure 5.2: The distribution of ice shelf regions thinner than 200 m. The regions colored white are where the ice shelf is thinner than 200 m. The black color is sea, the light gray is the ice sheet and the dark gray is the ice shelf.

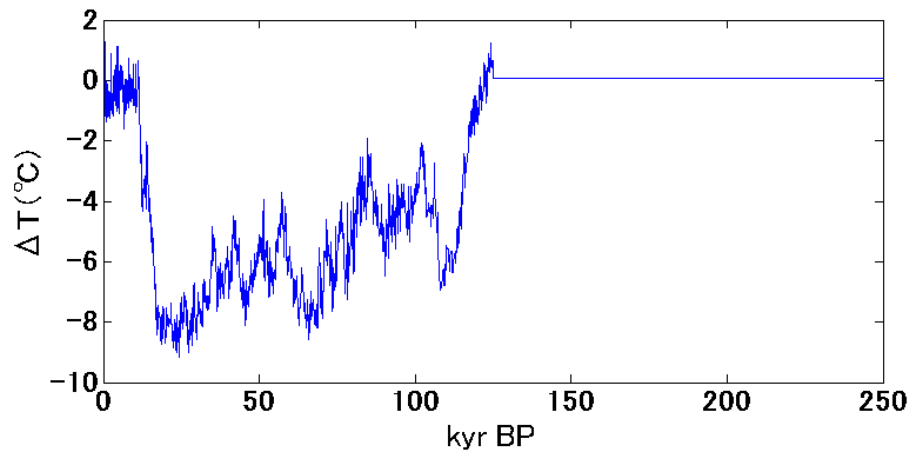


Figure 5.3: The temperature settings used in the paleoclimatic spin-up. The deviation of temperature from 2004 is applied with present surface climate data [Arthern et al., 2006] and geothermal heat flux [Shapiro and Ritzwoller, 2004].

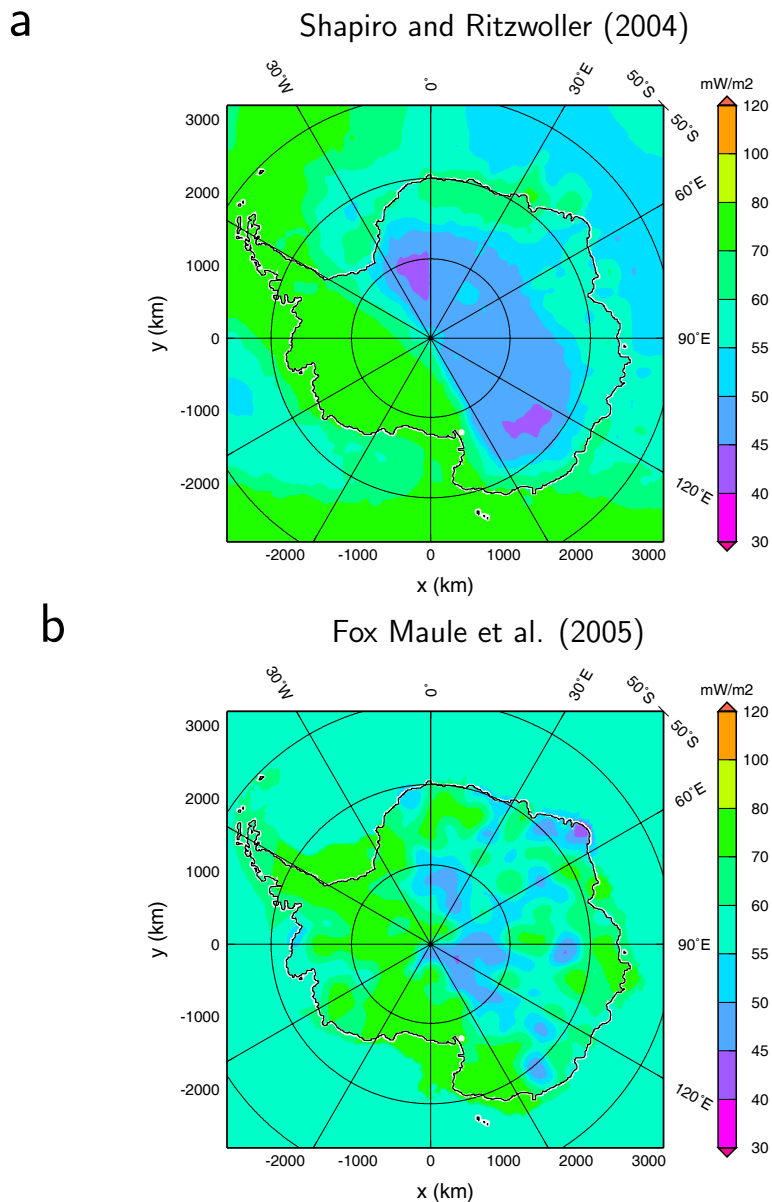


Figure 5.4: Two geothermal flux dataset by (a) Shapiro and Ritzwoller [2004] and (b) Fox Maule et al. [2005].

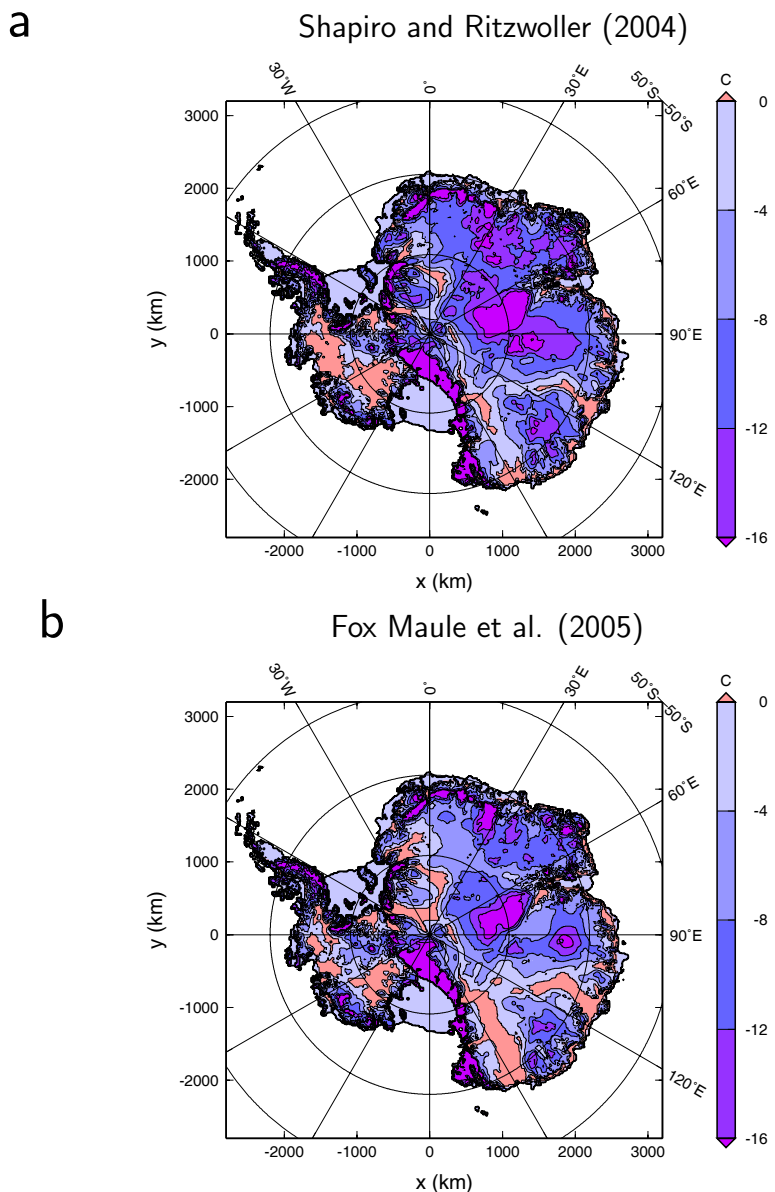


Figure 5.5: The results of paleoclimate spin-up using the two different geothermal heat flux datasets in 20 km resolution (a) Shapiro and Ritzwoller [2004], SR, (b) Fox Maule et al. [2005], SE.

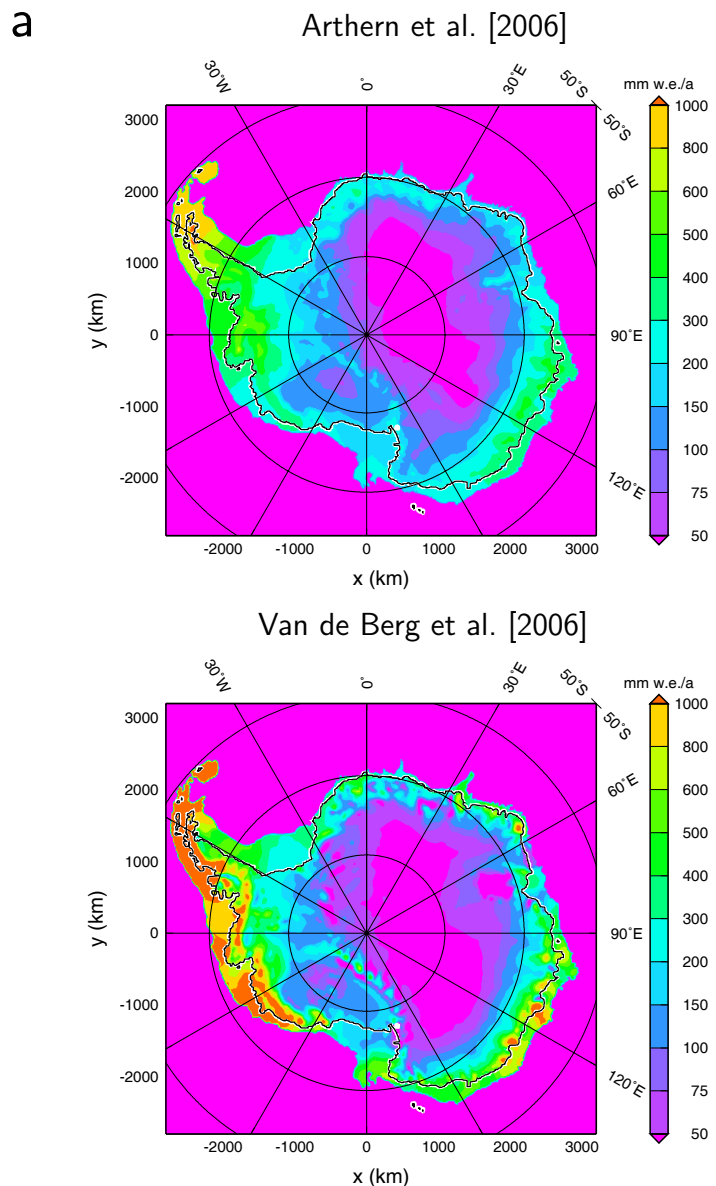


Figure 5.6: Two datasets of accumulation rates (a) Arthern et al. [2006] and (b) Van de Berg et al. [2006].

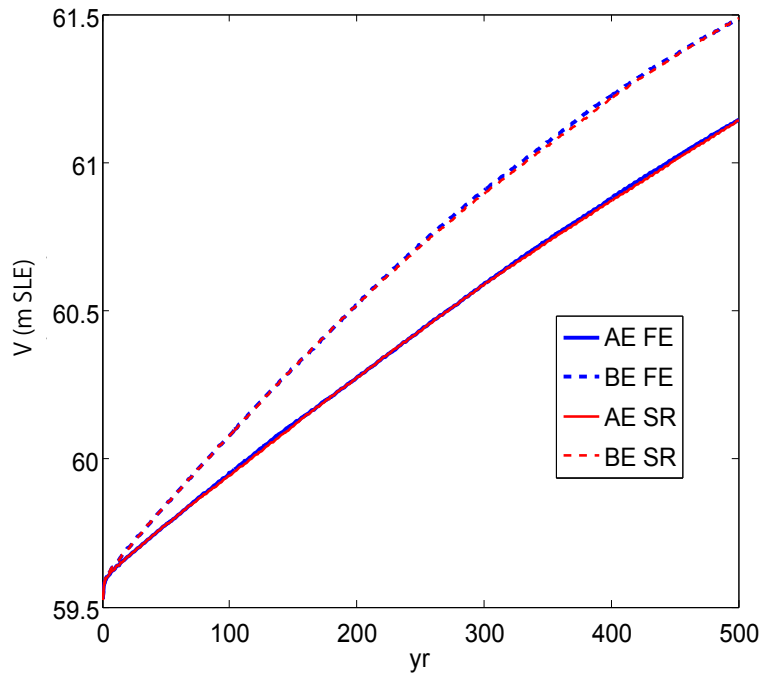


Figure 5.7: Simulated changes in grounded ice volume, V (expressed in m SLE) for experiment CTL (constant climate control run), carried out alternately with surface accumulation data by Arthern et al. [2006] (marked AE) and Van de Berg et al. [2006] (marked BE). The two geothermal datasets are also applied to the paleoclimatic spin-up; Fox Maule et al. [2005] (marked FE) and Shapiro and Ritzwoller [2004] (marked SR). Note that $t = 0$ corresponds to the year 2004. The resolution is 20 km.

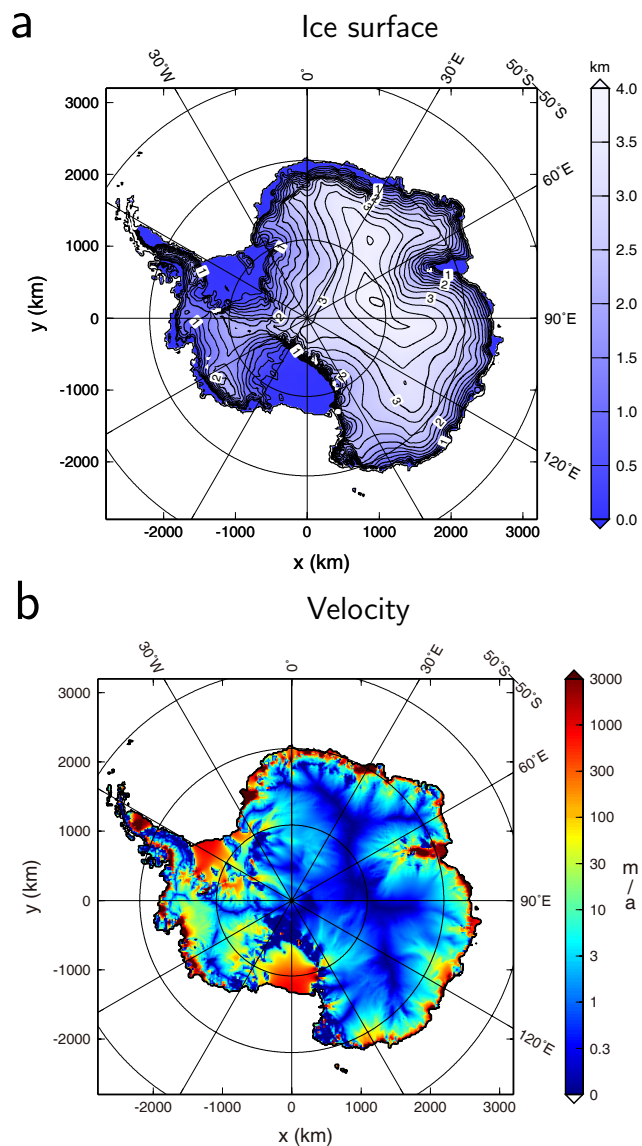


Figure 5.8: The result of the spin-up of the control run in 20 km resolution.
 (a) Ice surface topography, (b) ice surface velocity.

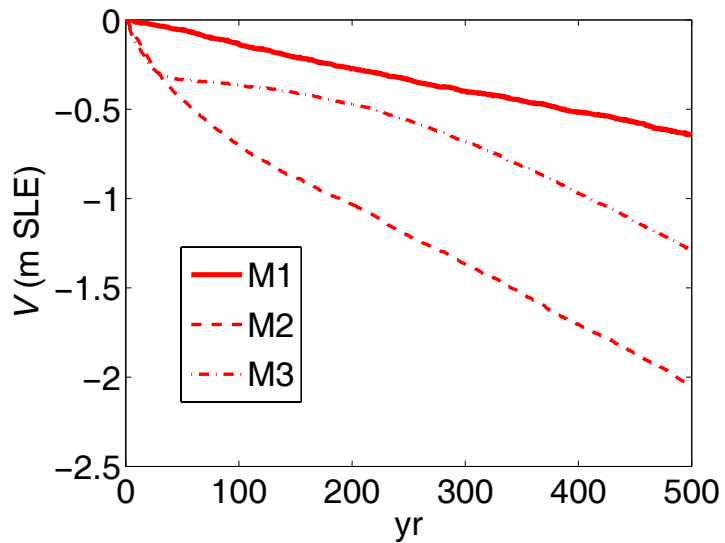


Figure 5.9: Simulated changes in ice volume relative to the control run CTL for experiments M1 (constant climate, sub-ice-shelf melting $2 \text{ m ice equiv. a}^{-1}$), M2 (constant climate, sub-ice-shelf melting $20 \text{ m ice equiv. a}^{-1}$), M3 (constant climate, sub-ice-shelf melting $200 \text{ m ice equiv. a}^{-1}$) The resolution is 40 km.

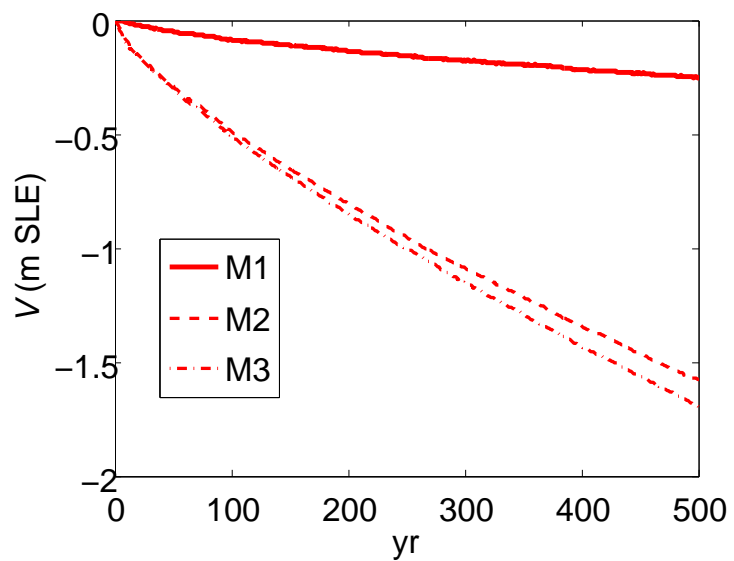


Figure 5.10: Simulated changes in grounded ice volume at 40 km resolution, V (expressed in m SLE), to the control run CTL for experiments M1 (constant climate, sub-ice-shelf melting 2 m ice equiv. a^{-1}), M2 (constant climate, sub-ice-shelf melting 20 m ice equiv. a^{-1}), M3 (constant climate, sub-ice-shelf melting 200 m ice equiv. a^{-1})

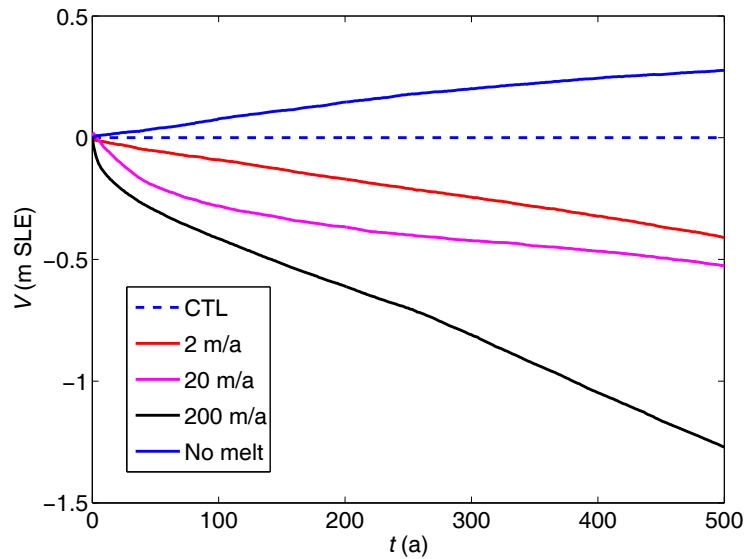


Figure 5.11: Simulated changes in grounded ice volume, V (expressed in m SLE), relative to the control run CTL for experiments M1 (constant climate, sub-ice-shelf melting $2 \text{ m ice equiv. a}^{-1}$), M2 (constant climate, sub-ice-shelf melting $20 \text{ m ice equiv. a}^{-1}$), M3 (constant climate, sub-ice-shelf melting $200 \text{ m ice equiv. a}^{-1}$) and M0 (constant climate, zero sub-ice-shelf melting). Note that $t = 0$ corresponds to the year 2004. The resolution is 20 km.

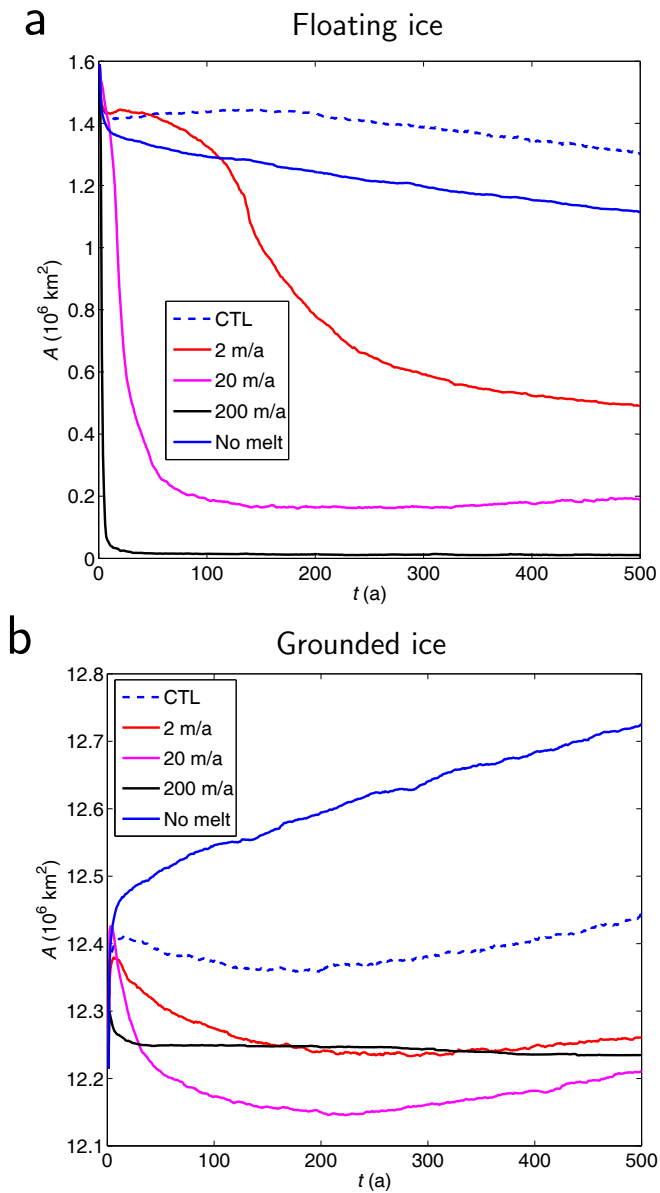


Figure 5.12: Simulated grounded and floating ice area, calculated in M1-M3 experiments. $t = 0$ corresponds to the year 2004.

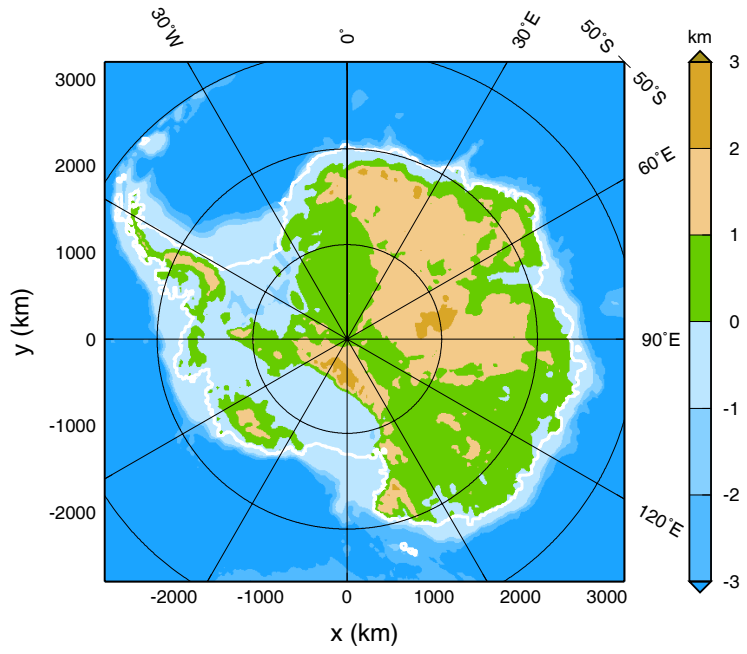


Figure 5.13: The bedrock topography of the ice base. The dataset is defined in the SeaRISE project with the improved BEDMAP1 dataset [Lythe et al., 2001].

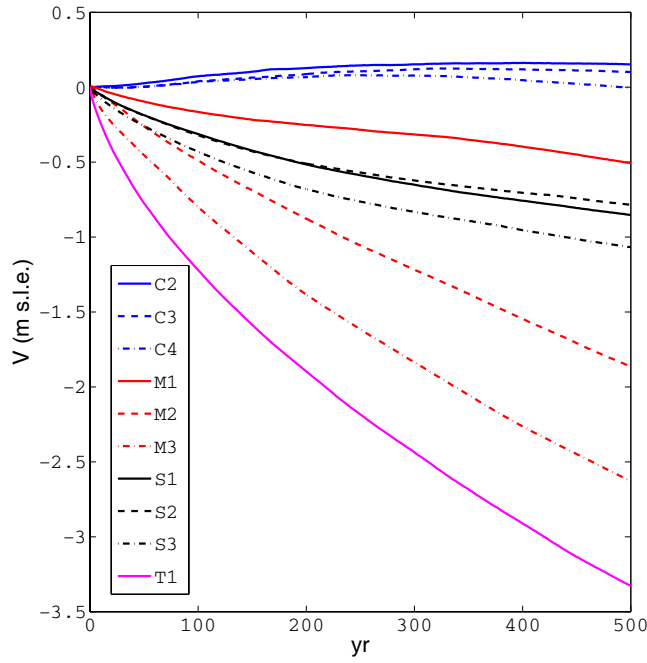


Figure 5.14: Simulated changes in grounded ice volume, V (expressed in m SLE), relative to the control run CTL for the experiments (1). Surface climate changes: Blue lines, C2 (solid line, AR4 climate applied from 2004 to 2098 and constant after that) C3 (broken line, $1.5 \times$ AR4 climate, C4 (chain line, $2 \times$ AR4 climate). (2). Ocean warming: Red lines, M1 (solid line, sub-ice-shelf melting, 2 m/a). M2 (broken line, sub-ice-shelf melting, 20 m/a). M3 (chain line, sub-ice-shelf melting, 200 m/a). (3). Sub-glacial change: Black lines, S1 (solid line, double basal sliding applied), S2 (broken line, $2.5 \times$ basal sliding applied) and S3 (solid line, $3 \times$ basal sliding applied). (4). T1 (magenta line, AR4 climate, double basal sliding and 20 m/a sub-ice-shelf melting is applied). The resolution is 10 km.

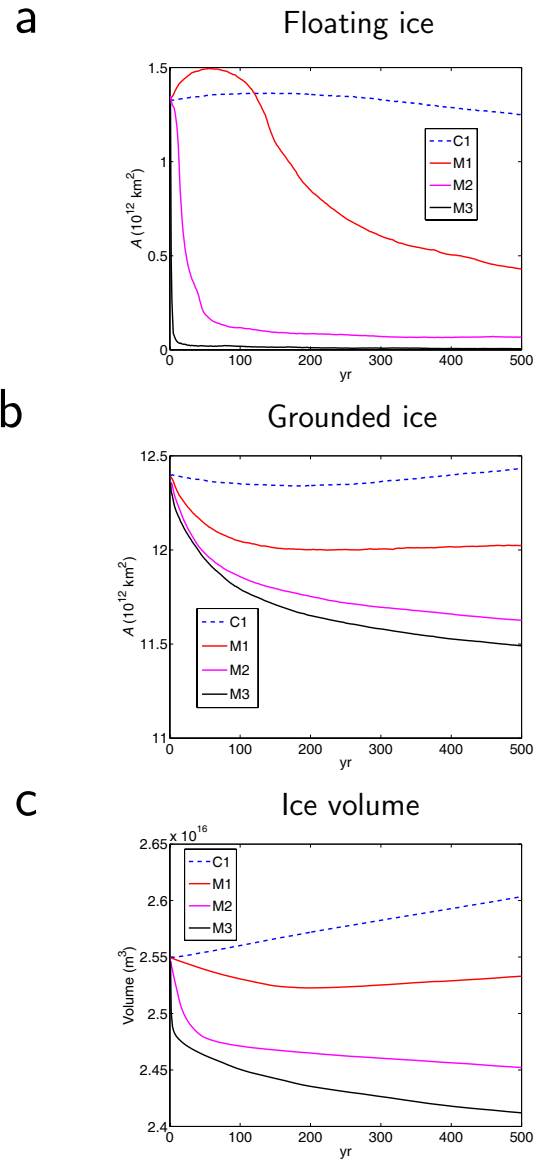


Figure 5.15: Results of enhanced sub-ice-shelf melt, M-series, experiments.
 (a) Floating ice area. (b) Grounded ice area. (c) Total ice volume. $t = 0$ corresponds to the year 2004. The resolution is 10 km.

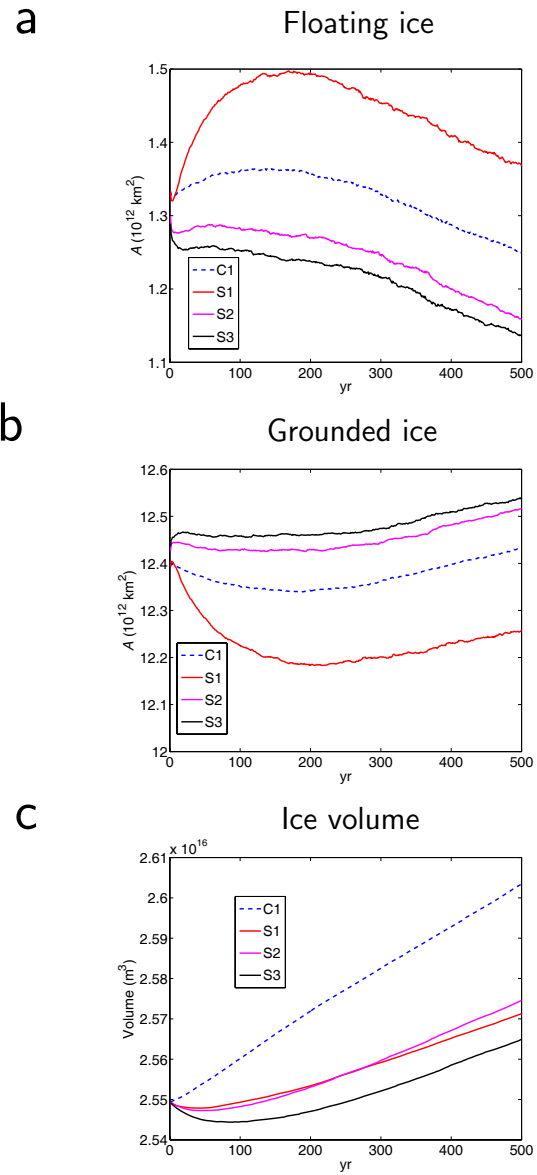


Figure 5.16: Results of enhanced basal sliding, S-series, experiments. (a) Floating ice area. (b) Grounded ice area. (c) Total ice volume. $t = 0$ corresponds to the year 2004. The resolution is 10 km.

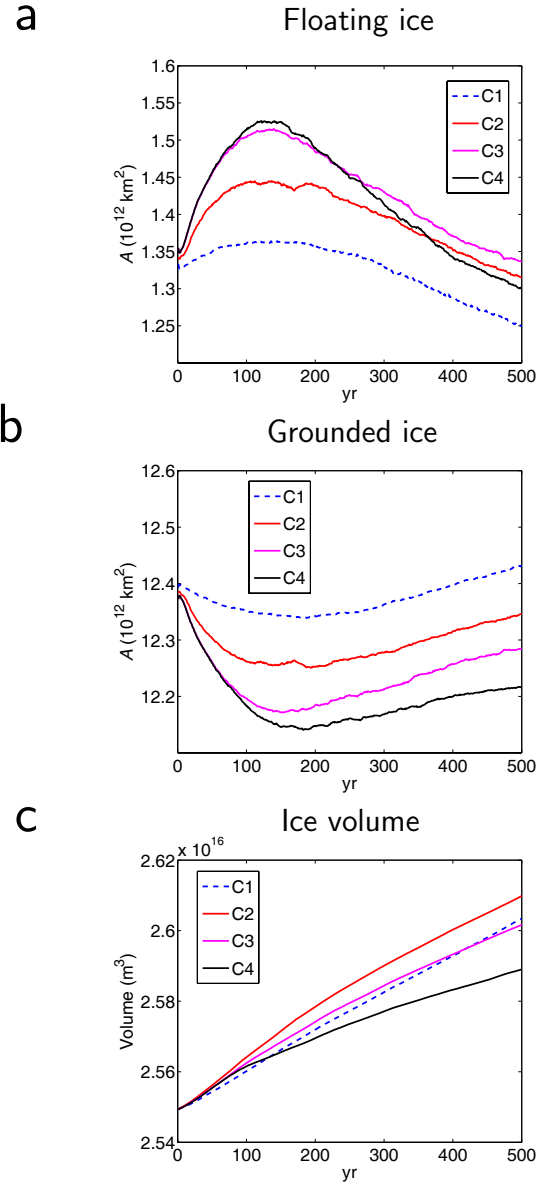


Figure 5.17: Results of surface climate change, C-series, experiments. (a) Floating ice area. (b) Grounded ice area. (c) Total ice volume. $t = 0$ corresponds to the year 2004. The resolution is 10 km.

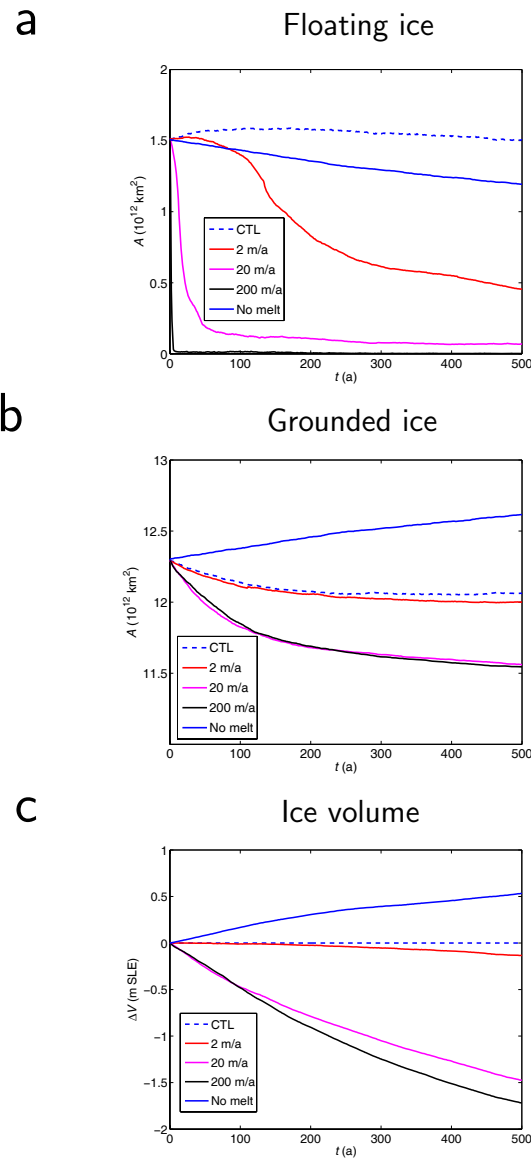


Figure 5.18: Results of sub-ice-shelf melting rates change with additional 20 year spin-up, M-series, experiments. (a) Floating ice area. (b) Grounded ice area. (c) Sea level equivalent ice volume. $t = 0$ corresponds to the year 2004. The resolution is 20 km.

Chapter 6

Discussion

6.1 Comparison to the present-day ice sheet

The result of fixed topography spin-up is compared with a observed record by Rignot et al. [2011a] (Fig. 6.1). The result shows that the simulated result can represent the features of the Antarctic ice sheet flow. However, the simulated velocities are slower than the observed velocities. Considering the fact that the present Antarctic ice sheet mass balance is negative [Rignot et al., 2011b], ice flux is not enough to reduce ice mass inland. It would be caused by the cold ice base due to low geothermal heat flux beneath the ice sheet as shown in Fig. 5.5. The geothermal heat flux might be warmer than estimated one. Another possibility is that the fixed topography treatment caused the cold ice base. Basal frictional heating depends on the basal stress. This basal stress also depends on the surface slope. The evolution of the ice surface may cause the additional heating.

The high sub-ice-shelf melting rate at the West Antarctic Ice sheet margin, particularly at Pine Island Bay, is considered to affect the upward glacier flow [Rignot and Jacobs, 2002]. Sub-ice-shelf melting rate influences grounding line migration directly, and the influx from grounded regions indirectly [Schoof, 2007a]. The great sensitivity of ice volume to sub-ice-shelf melting experiments is thought to be responsible for recent changes in the West Antarctic Ice Sheet [Rignot, 2006]. However, it is inappropriate to set the same sub-ice-shelf melting rate for the whole of the Antarctic ice shelves. The sub-ice-shelf melting rate around the grounding line can be 10 m/a [e.g., Wen et al., 2010]. Hellmer et al. [2011] estimated the sub-ice-shelf mass balance of ice shelves for 100 years in the future. In this estimation, although ice shelves of the Amundsen sea region, and some part of the Ronne ice shelves, have high sub-ice-shelf melting rates, that of the Ross ice shelf area did not

change significantly (melt rates were less than 1 m/a at the most of the shelf) over the next 100 years.

Figure 6.2 shows ice sheet and ice shelf mass and ice thickness changes in the C4 run. The ice shelves of the Antarctic peninsula were lost by surface melting due to the higher surface temperature (Fig. 6.3). A part of the Amery and the Ross ice shelf was also lost. It is suggested that the collapse of Larsen B ice shelf is caused by surface warming [van den Broeke, 2005]. These results suggest that the ice shelf is sensitive to surface warming in these regions. Ice shelf area did not decrease in the S3 experiment (Fig. 6.4). However, ice thickness in the East Antarctic Ice Sheet greatly decreased in this experiment. Decrease affected not only the margins but also the inland areas such as the upper part of the Shirase glacier. In both the experiments, ice thickness increased around Pine Island Glacier, Marie Byrd Land. The cause is probably low ice flux around these regions and low sub-ice-shelf melting around the transition zone. The Pine Island Glacier region lost its mass when ice shelf melt rates were high, such as in the M2 experiment (Fig. 6.5). Although the upper part of PIG increased in thickness even in this experiment, it may be due to low ice flux, their area lost ice mass compared with other experiments. Most of the ice shelves disappeared in the M2 and M3 experiments (Fig. 6.6). Especially in the M3 experiment, inland regions of the West Antarctic Ice Sheet lost mass due to extreme sub-ice-shelf melting. Although sub-ice-shelf melting rates in this experiment were much higher than the observed result, it indicated the instability of the WAIS to Antarctic Ocean warming.

6.2 The dynamics of ice sheet and ice shelves

A shallow ice approximation, shallow shelf approximation or coupling of the both dynamics was applied to most of the ice sheet models. The shallow shelf approximation was applied to ice shelves, the shallow ice approximation to ice sheets. The application of the shallow shelf approximation to the grounding zone is appropriate for representing the dynamic coupling between ice sheets and ice shelves. The coupling of the shallow ice approximation with the shallow shelf approximation would be better for the momentum balance. Huybrechts [1990] constructed an ice sheet model which included ice shelf dynamics. This model used the shallow ice approximation for the ice sheet and shallow shelf approximation for the ice shelf. A special treatment for the grounding line zone was also applied in the ice sheet model [Huybrechts, 1990]; the coupling of the shallow ice approximation with the shallow shelf approximation [Huybrechts, 1990]. The treatment resembles the dynamic

part of the Pennsylvania State University ice sheet model. The difference was that it was applied to the whole of the ice sheet. The boundary layer theory [Schoof, 2007b] has also been applied to the ice sheet model to estimate ice flux at the grounding line [Pollard and DeConto, 2009]. In the ice sheet model GRISLI [Ritz et al., 2001], shallow shelf approximation was applied to the ice stream and the ice shelf and the shallow ice approximation was applied to the ice sheet. The parallel ice sheet model (PISM) uses the shallow shelf approximation as a sliding law. The total horizontal velocity is a weighted sum of the solution of the ice shelf model with the solution of the ice sheet model. In PISM-PIK, the horizontal velocity is just the sum of the solution of the shallow shelf approximation and the shallow ice approximation. Weighting is not applied. Although implementation of these mechanism may improve the performance of the model, the increasing number of shallow shelf calculation points and the iterations are the computational approach. It is necessary to consider the balance between sophistication and computation time in each case.

The other possibility is applying higher order treatments. Elmer/Ice [Zwinger et al., 2007, Seddik et al., 2012] and ISSM [Ice Sheet System Model, Larour et al., 2012] use full stokes ice sheet dynamics. Higher order dynamics are applied to ISSM, Glimmer-CISM [Salinger et al., 2011] and IcIES [Saito et al., 2003]. The problem with this approach is that it takes much more computation time than do applying the shallow ice approximation or shallow shelf approximation [Larour et al., 2012]. Several iteration schemes have been proposed to reduce the computational effort required for higher order dynamics [cf. Baral et al., 2001, Soucek and Martinec, 2008]. Ahlkrona [2011] implements second order ice sheet dynamics [Baral et al., 2001] to the ice sheet model SICOPOLIS. Coupling these dynamics with the shallow shelf approximation for ice shelves will improve the treatment of ice streams and of the transition zone.

The other difficulty for the dynamics is the elasticity of ice [Jellinek and Brill, 1956]. On short time scales, ice behaves as an elastic material. This produces some interesting effects on glacier and ice sheet dynamics [Lingle et al., 1981, Bindschadler et al., 2003, Gudmundsson, 2006, Sugiyama et al., 2007]. One of these effects is that the ocean tide might modulate ice shelf flow [Brunt et al., 2010].

6.3 Grounding line migration

One of the most important controls on the ice volume change is grounding line migration. The results of the SearISE experiments shows that Antarctic

ice volume is sensitive to the change of ice shelf or ice sheet area. This implies that grounding line migration processes are enormously important for Antarctic ice sheet evolution. However, numerical representation of grounding line migration is difficult to incorporate in the large-scale ice sheet model. The dynamics changes greatly in the transition zone between ice sheet and ice shelf. This results in the strong dependency on resolution in simulations of grounding line migration in the fixed grid model [Vieli and Payne, 2005]. Very high resolution, several hundred metres or a kilometre, is required to represent grounding line migration [cf. Gladstone et al., 2012]. In SeaRISE experiments, however, the highest resolution is 10 km. Since this is ten times larger than the requirement, improved treatment of the grounding line is required. Two methods have been proposed to achieve this. One is the adaptive mesh treatment (AMR) around the grounding line [Gladstone et al., 2010]. This is a means of solving the numerical equation by discretizing the domains of interest into a grid of many individual elements. It is possible to discretize domains around the grounding zone with fine resolution. The other is the application of boundary layer theory [Pollard and DeConto, 2009] around the grounding zone. A two dimensional analytical solution of the flux at the grounding line [Schoof, 2007b] is applied around the grounding zone with several conditions. Docquier et al. [2011] shows that application of this theory increases the performance of grounding line migration. However, this flux at the grounding line is based merely on a two dimensional approach. It is considered that the horizontal gradient parallel to the grounding line is not so large in typical 2-D flow [Pollard and DeConto, 2009].

The ice sheet does not retreat from the glacial condition to the present condition in the non-fixed topography spin up experiment. There are several possible causes for this problem. As stated above, ice volume continuously increases over five hundreds years in the control run. [Pollard and DeConto, 2009] assumed steady state ice volume in both glacial and interglacial conditions. The outcome was that ice volume does not change when basal melt rate is fixed. In particular, the ice sheet does not shrink to the extreme interglacial condition as in the other cases. This implies that sub-ice-shelf melting is an important influence on the glacial-interglacial evolution of the ice sheet. Sub-ice-shelf melt rates are constant over the glacial cycle. This condition and the low ice flux of the ice sheet, prevented deglaciation during the termination and the Holocene.

Although the grounding line migration velocity depends directly on mass balance, it also depends greatly on ice dynamics and basal flow. Certainly, observations of the sub-ice-shelf conditions is not enough. However, there are several ways of estimating the sub-ice-shelf ocean conditions. The property of basal sliding is not known since it depends on many components (interaction

of the ice base with the lithosphere base, dynamics of the sub-glacial till, the basal water channels and presence of sub-glacial lakes). Observations of the basal flow are also unknown. The model experiment of ice stream/ice shelf/ocean coupling shows the importance of the basal flow law [Walker et al., 2008]. Even the basal flow law itself and the methodology to estimate these conditions have their limitations. The properties of the basal condition is one of the largest uncertainties in estimating grounding line migration. It would therefore be desirable to improve observations of ice base processes and provide validation of basal sliding theories.

6.4 Calving

Calving is the most important component of mass balance for the Antarctic ice sheet. However, the conditions for calving are still under discussion because of the complex mechanisms involved. A simple calving law is used in this study and a threshold thickness of 50 m is applied. This value was chosen to keep today's ice shelf as the initial condition. However, this is considerably thinner than the thickness of the major present-day Antarctic ice shelves. A calving event is a consequence of fracture (crevasse) penetration. Therefore, it is necessary consider the dynamic conditions of the ice. Moreover, there are difference between how crevasses behave when they ultimately break. Several types of calving law have been proposed to study the ice shelf or tidewater glacier calving. Nye [1957] considered that crevasse depth depends on the balance of hydrostatic pressure and the shear stresses. Such a crevasse depth model has been applied to tidewater glaciers. Nick et al. [2010] simulated the evolution of tidewater glaciers by using the crevasse depth model. The sub-ice-shelf crevasses are also considered in this model. Otero et al. [2010] included the crevasse depth model into a three dimensional glacier model. There are other types of calving laws for glaciers. Pralong and Funk [2005] proposed continuous damage mechanics as a theory on crevasse formation. The rheology of damaged ice and the evolution of damage is defined in this theory. The other difficulty of the calving study is that it does not depend only on the viscosity of ice but also on the elastic property of ice [e.g., Plate et al., 2012]. It is thus necessary to measure stress and strain rates around the calving front to validate these calving studies. Observations of seismic waves in glaciers could also help in understanding of the calving processes.

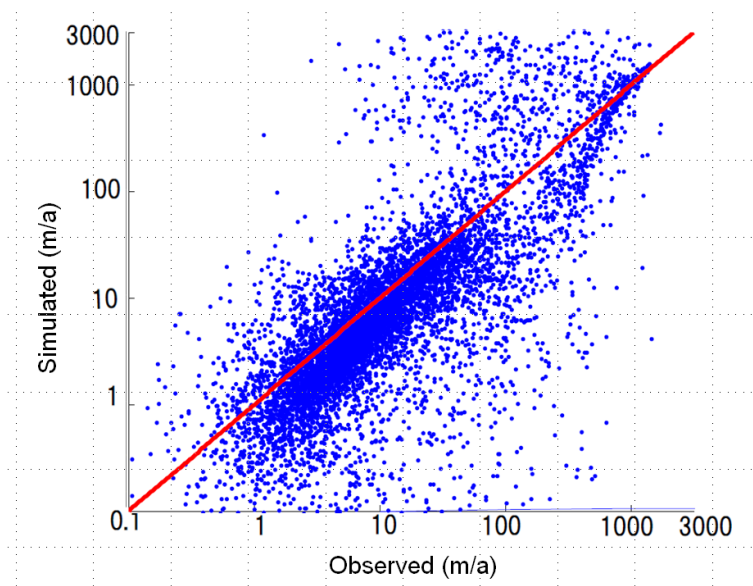


Figure 6.1: Scatter map comparing simulated ice velocity (10 km resolution) with the observed dataset [Rignot et al., 2011a].

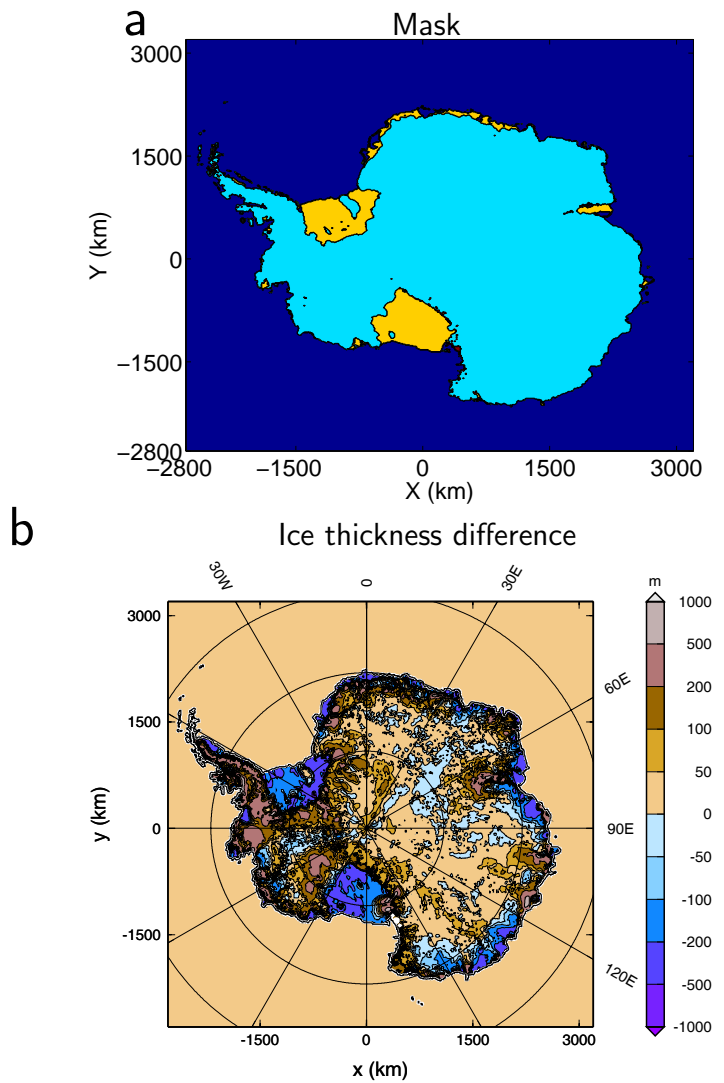


Figure 6.2: (a) Simulated ice sheet/ice shelf mask of the last time step and (b) ice thickness change from the initial condition to the last time step, calculated in C4 experiments. $t = 0$ corresponds to the year 2004.

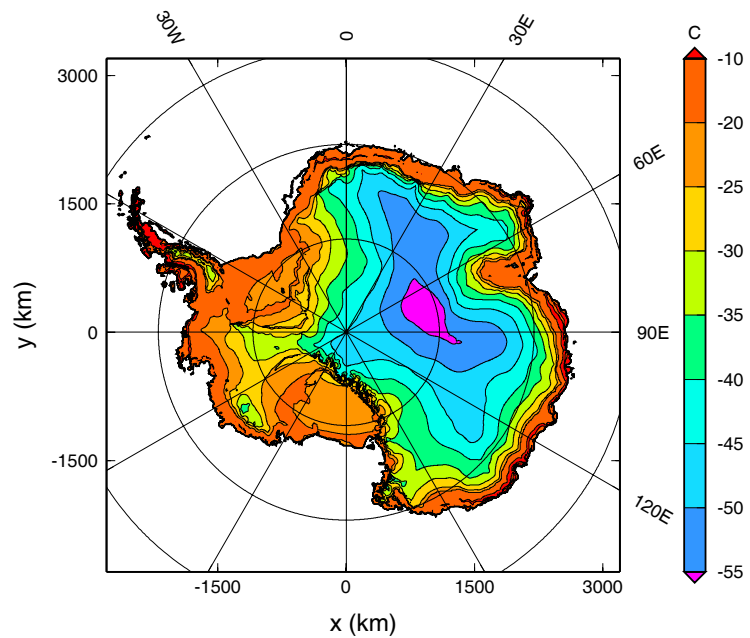


Figure 6.3: Annual surface temperature on the ice sheet at the last time step of C4 experiment.

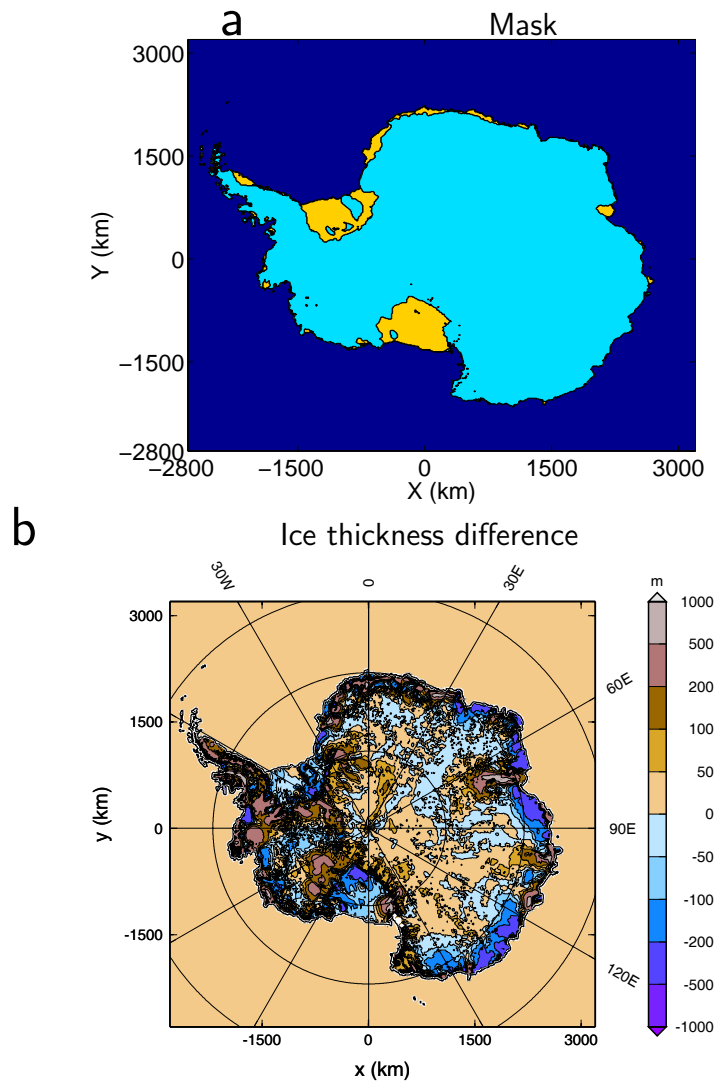


Figure 6.4: (a) Simulated ice sheet/ice shelf mask of the last time step and (b) ice thickness change from the initial condition to the last time step, calculated in S3 experiments. $t = 0$ corresponds to the year 2004.

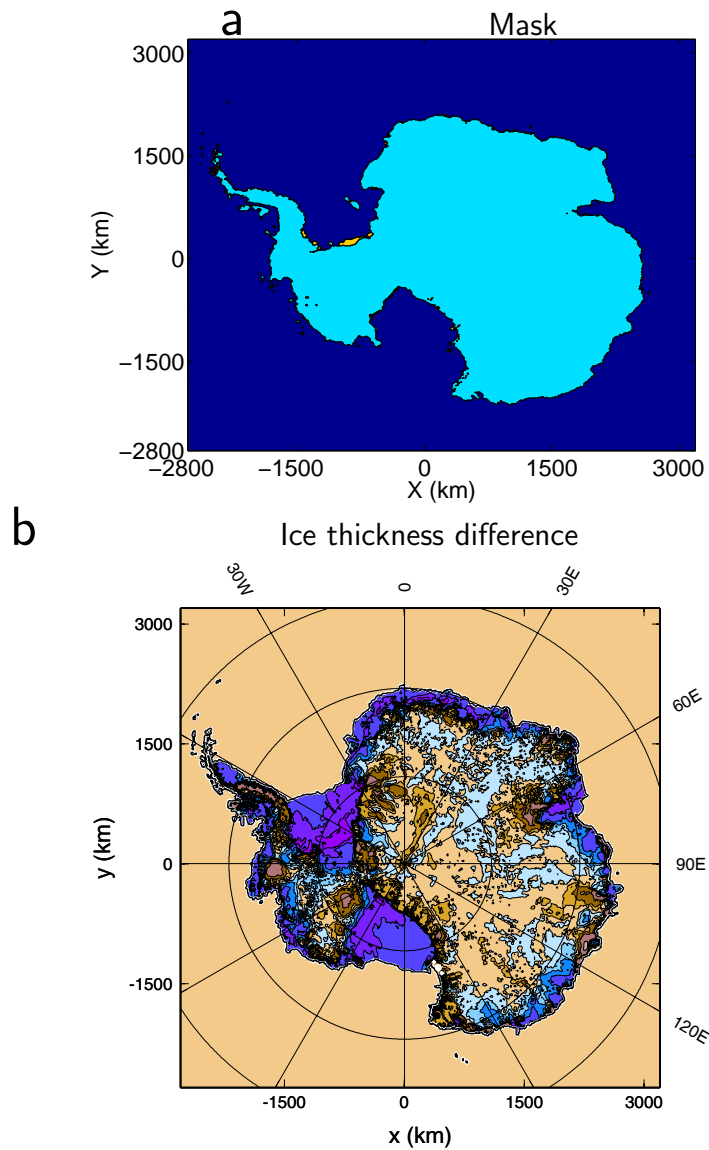


Figure 6.5: (a) Simulated ice sheet/ice shelf mask of the last time step and (b) ice thickness change from the initial condition to the last time step, calculated in M3 experiments. $t = 0$ corresponds to the year 2004.

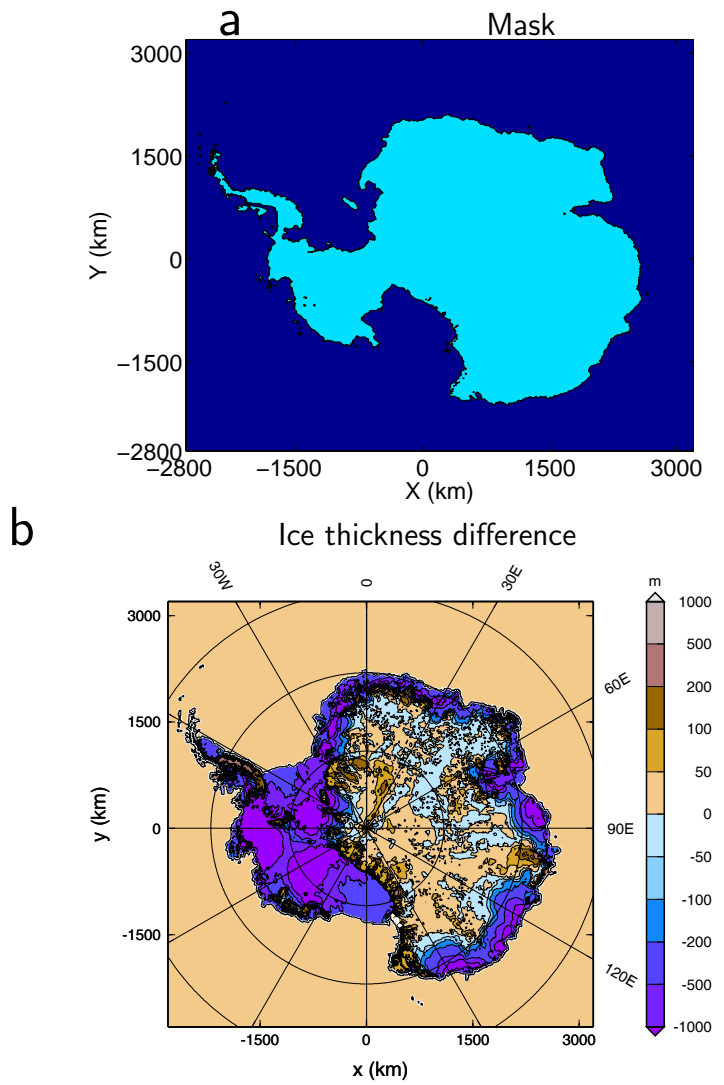


Figure 6.6: (a) Simulated ice sheet/ice shelf mask of the last time step and (b) ice thickness change from the initial condition to the last time step, calculated in M3 experiments. $t = 0$ corresponds to the year 2004.

Chapter 7

Summary

A theory of ice sheet dynamics on orthogonal curvilinear coordinates was considered and applied to shallow shelf approximation. The application of the theory and its coupling to the ice sheet was the next step. A module of ice shelf dynamics was therefore constructed and coupled to the dynamic/thermodynamic ice sheet model SICOPOLIS. The performance of the ice shelf model was validated against the analytical solution of the shallow shelf approximation, the ice shelf ramp. The results show that the model well represents the analytical solution.

The new version of the model is applied to the Antarctic ice sheet by using the SeaRISE dataset. A paleo-climatic spin-up over 250 kyr was applied to find today's condition of the ice sheet. The non-fixed topography spin-up produced the ice sheet conditions during the glacial period. However, there is a problem involved with deglaciation process that occurred between the last glacial maximum and the present condition. The reasons underlying this problem are low grounded ice flux and constant, low sub-ice shelf melting rates. A fixed topography spin-up was finally applied to future climate scenarios. The sensitivities were checked of different datasets of geothermal heat flux [Shapiro and Ritzwoller, 2004, Fox Maule et al., 2005] and accumulation rates [Arthern et al., 2006, Van de Berg et al., 2006]. The results showed that sea level equivalent ice volume are not very sensitive to geothermal heat flux difference but to accumulation rate differences. Sea level equivalent ice volume based on the Arthern et al. [2006] dataset is 0.4 m SLE lower than that with the Van de Berg et al. [2006] dataset. The difference is caused by the high accumulation rates around the ice sheet margin in Van de Berg et al. [2006] dataset.

Sensitivities to sub-ice-shelf melting rates was evaluated with SeaRISE M-series experiments, where surface climate forcing was kept steady at present-day conditions while the sub-ice-shelf melting rates were varied over 0 –

200 m/a. The range of grounded ice volume changed across the M-series being $\sim 0.5 - 0.7$ m SLE after 100 years and $\sim 1.5 - 2.0$ m SLE after 500 years in 40 km runs. In 20 km runs, it is ~ 1.3 m SLE after 100 years and ~ 2.25 m SLE after 500 years. The differences between the results of each experiment were caused not only by the settings but also by the resolution. This was because resolution affects the basal topography of the bedrock and the grounding line migration dynamics themselves. All of these simulations showed that ice sheet volume is greatly sensitive to sub-ice-shelf melting rate. Ice sheet volume correlated strongly with floating area in these experiments. These results indicate the factors likely to be responsible for recent changes in the West Antarctic Ice Sheet [e.g., Rignot, 2006] and agree with findings by Huybrechts [1990].

The range of outcomes of all of SeaRISE experiments in 10 km resolution was ~ 1.3 m SLE after 100 years and ~ 3.3 m SLE after 500 years. Although ice volume is sensitive to sub-ice-shelf melting, basal sliding is also important. The changes caused by surface climate experiments were small. The combination run, T1, is the worst case (the coupling of C2, S1 with M2). It implies that the combination of several forcing factors would cause additional ice loss. These experiments suggest the Antarctic ice sheet is sensitive to climate change. The sea level change caused by the Antarctic ice sheet may not be negligible in the future. Further studies of sub-ice-shelf melting and basal sliding processes are needed because outcomes are quite sensitive to these processes.

Bibliography

- J. Ahlkrona. Implementing higher order dynamics into the ice sheet model SICOPOLIS. Master’s thesis, Department of Information Technology, Uppsala University, Sweden, 2011.
- A. Arakawa and V. R. Lamb. Computational design of the basic dynamical processes of the UCLA general circulation model. In J. Chang, editor, *Methods in Computational Physics Vol. 17*, pages 173–265. Academic Press, New York, NY, USA, 1977.
- R. J. Arthern, D. P. Winebrenner, and D. G. Vaughan. Antarctic snow accumulation mapped using polarization of 4.3-cm wavelength microwave emission. *Journal of Geophysical Research*, 111(D6):D06107, 2006.
- L. Augustin, C. Barbante, P. R. F. Barnes, J. M. Barnola, M. Bigler, E. Castellano, O. Cattani, J. Chappellaz, D. Dahl-Jensen, B. Delmonte, et al. Eight glacial cycles from an Antarctic ice core. *Nature*, 429(6992):623–628, 2004.
- D. R. Baral, K. Hutter, and R. Greve. Asymptotic theories of large-scale motion, temperature, and moisture distribution in land-based polythermal ice sheets: a critical review and new developments. *Applied Mechanics Reviews*, 54:215, 2001.
- R. A. Bindschadler, M. A. King, R. B. Alley, S. Anandakrishnan, and L. Padman. Tidally controlled stick-slip discharge of a West Antarctic ice. *Science*, 301(5636):1087–1089, 2003.
- K. M. Brunt, M. A. King, H. A. Fricker, and D. R. MacAyeal. Flow of the Ross Ice Shelf, Antarctica, is modulated by the ocean tide. *Journal of Glaciology*, 56(195):157–161, 2010.
- E. Bueler and J. Brown. Shallow shelf approximation as a “sliding law” in a thermomechanically coupled ice sheet model. *Journal of Geophysical Research*, 114(F03008):F03008, 2009.

- R. Calov. *Das thermomechanische Verhalten des Grönländischen Eisschil-des unter der Wirkung verschiedener Klimaszenarien – Antworten eines theoretisch-numerischen Modells*. Doctoral thesis, Department of Mechanics, Darmstadt University of Technology, Germany, 1994.
- R. Calov, A. A. Savvin, R. Greve, I. Hansen, and K. Hutter. Simulation of the Antarctic ice sheet with a three-dimensional polythermal ice-sheet model, in support of the EPICA project. *Annals of Glaciology*, 27:201–206, 1998.
- J. C. Comiso. Variability and trends in Antarctic surface temperatures from in situ and satellite infrared measurements. *Journal of Climate*, 13(10):1674–1696, 2000.
- K. M. Cuffey and W. S. B. Paterson. *The Physics of Glaciers*. Elsevier, Amsterdam, The Netherlands etc., 4th edition, 2010. ISBN 978-0-12-369461-4.
- H. De Angelis and P. Skvarca. Glacier surge after ice shelf collapse. *Science*, 299(5612):1560, 2003.
- C. M. S. Doake. Ice-shelf stability. In D. G. Ainley, G. J. Divoky, J. Steele, S. Thorpe, and K. Turekian, editors, *Encyclopedia of Ocean Sciences*, pages 1282–1290. Academic Press, San Diego, CA, USA, 2001.
- D. Docquier, L. Perichon, and F. Pattyn. Representing grounding line dynamics in numerical ice sheet models: Recent advances and outlook. *Surveys in Geophysics*, 32(4-5):417–435, 2011.
- P. L. Forsström and R. Greve. Simulation of the Eurasian ice sheet dynamics during the last glaciation. *Global and Planetary Change*, 42(1-4):59–81, 2004.
- J. P. F. Fortuin and J. Oerlemans. Parameterization of the annual surface temperature and mass balance of Antarctica. *Annals of Glaciology*, 14:78–84, 1990.
- C. Fox Maule, M. E. Purucker, N. Olsen, and K. Mosegaard. Heat flux anomalies in Antarctica revealed by satellite magnetic data. *Science*, 309 (5733):464–467, 2005.
- R. M. Gladstone, V. Lee, A. Vieli, and A. J. Payne. Grounding line migration in an adaptive mesh ice sheet model. *Journal of Geophysical Research*, 115 (F4):F04014, 2010.

- R. M. Gladstone, A. J. Payne, and S. L. Cornford. Resolution requirements for grounding-line modelling: sensitivity to basal drag and ice-shelf buttressing. *Annals of Glaciology*, 53(60):97, 2012.
- K. Goto-Azuma. Millennial-scale climate variability during the past 720,000 years recorded in the Dome Fuji ice core. In *Geophysical Research Abstracts*, volume 10, 2008.
- R. Greve. *Thermomechanisches Verhalten polythermer Eisschilde – Theorie, Analytik, Numerik*. Doctoral thesis, Department of Mechanics, Darmstadt University of Technology, Germany, 1995. Berichte aus der Geowissenschaft, Shaker Verlag, Aachen, Germany.
- R. Greve. Application of a polythermal three-dimensional ice sheet model to the Greenland ice sheet: response to steady-state and transient climate scenarios. *Journal of Climate*, 10(5):901–918, 1997a.
- R. Greve. A continuum-mechanical formulation for shallow polythermal ice sheets. *Philosophical Transactions of the Royal Society of London. Series A: Mathematical, Physical and Engineering Sciences*, 355(1726):921–974, 1997b.
- R. Greve and H. Blatter. *Dynamics of Ice Sheets and Glaciers*. Springer, Berlin, Germany etc., 2009. ISBN 978-3-642-03414-5. doi: 10.1007/978-3-642-03415-2.
- G. H. Gudmundsson. Fortnightly variations in the flow velocity of Rutford Ice Stream, West Antarctica. *Nature*, 444(7122):1063–1064, 2006.
- H. Gudmundsson. Continuum mechanics. Karthaus Summer School Lecture Notes, 2007.
- H. Heinrich. Origin and consequences of cyclic ice rafting in the northeast atlantic ocean during the past 130,000 years. *Quaternary Research*, 29(2): 142–152, 1988.
- H. Hellmer, R. Timmermann, and F. Kauker. Will another ice shelf soon float in ‘hot’ water? In *International Symposium on “Interactions of Ice Sheets and Glaciers with the Ocean”, 610 June 2011, La Jolla, CA, USA*, 2011.
- T. Hondoh, editor. *Nature and behavior of dislocations in ice*, Sapporo, Japan, 2000. Hokkaido University Press.

- P. Huybrechts. A 3-D model for the Antarctic ice sheet: a sensitivity study on the glacial-interglacial contrast. *Climate Dynamics*, 5:79–92, 1990.
- P. Huybrechts and J. de Wolde. The dynamic response of the Greenland and Antarctic ice sheets to multiple-century climatic warming. *Journal of Climate*, 12(8):2169–2188, 1999.
- H. H. G. Jellinek and R. Brill. Viscoelastic properties of ice. *Journal of Applied Physics*, 27(10):1198–1209, 1956.
- A. Jenkins, D. G. Vaughan, S. S. Jacobs, H. H. Hellmer, and J. R. Keys. Glaciological and oceanographic evidence of high melt rates beneath Pine Island Glacier, West Antarctica. *Journal of Glaciology*, 43(143):114–121, 1997.
- D. Jenssen. A three-dimensional polar ice-sheet model. *Journal of Glaciology*, 18:373–389, 1977.
- I. Joughin and L. Padman. Melting and freezing beneath Filchner-Ronne ice shelf, Antarctica. *Geophysical Research Letters*, 30(9):1477, 2003.
- I. Joughin, E. Rignot, C. E. Rosanova, B. K. Lucchitta, and J. Bohlander. Timing of recent accelerations of Pine Island Glacier, Antarctica. *Geophysical Research Letters*, 30(13):1706, 2003.
- L. D. Landau and E. M. Lifshitz. *Course of Theoretical Physics – The classical theory of fields*. Butterworth-Heinemann, 1980.
- L. D. Landau and E. M. Lifshitz. *Course of Theoretical Physics – Fluid Mechanics*. Butterworth-Heinemann, 1987.
- E. Larour, H. Seroussi, M. Morlighem, and E. Rignot. Continental scale, high order, high spatial resolution, ice sheet modeling using the ice sheet system model (issm). *Journal of Geophysical Research*, 117: doi:10.1029/2011JF002140, 2012.
- C. S. Lingle, T. J. Hughes, and R. C. Kollmeyer. Tidal flexure of Jakobshavn Glacier, West Greenland. *Journal of Geophysical Research*, 86:3960, 1981.
- M. Llubes, C. Lanseau, and F. Rémy. Relations between basal condition, subglacial hydrological networks and geothermal flux in Antarctica. *Earth and Planetary Science Letters*, 241(3-4):655–662, 2006.

- M. B. Lythe, D. G. Vaughan, et al. BEDMAP: a new ice thickness and sub-glacial topographic model of Antarctica. *Journal of Geophysical Research*, 106(B6):11335–11, 2001.
- V. I. Morgan, T. H. Jacka, G. J. Akerman, and A. L. Clarke. Outlet glacier and mass-budget studies in Enderby, Kemp and MacRobertson lands, Antarctica. *Annals of Glaciology*, 3:204–210, 1982.
- F. M. Nick, C. J. Van der Veen, A. Vieli, and D. I. Benn. A physically based calving model applied to marine outlet glaciers and implications for the glacier dynamics. *Journal of Glaciology*, 56(199):781–794, 2010.
- J. F. Nye. The distribution of stress and velocity in glaciers and ice-sheets. *Proceedings of the Royal Society of London. Series A. Mathematical and Physical Sciences*, 239(1216):113–133, 1957.
- J. Otero, F. J. Navarro, C. Martin, M. L. Cuadrado, and M. I. Corcuera. A three-dimensional calving model: numerical experiments on Johnsons Glacier, Livingston Island, Antarctica. *Journal of Glaciology*, 56(196):200–214, 2010.
- F. Pattyn, A. Huyghe, S. De Brabander, and B. De Smedt. Role of transition zones in marine ice sheet dynamics. *Journal of Geophysical Research*, 111(F02004):F02004, 2006.
- A. J. Payne. A thermomechanical model of ice flow in West Antarctica. *Climate Dynamics*, 15(2):115–125, 1999.
- J. R. Petit, J. Jouzel, D. Raynaud, N. I. Barkov, J. M. Barnola, I. Basile, M. Bender, J. Chappellaz, M. Davis, G. Delaygue, M. Delmotte, V. M. Kotlyakov, M. Legrand, V. Y. Lipenkov, C. Lorius, L. Pepin, C. Ritz, E. Saltzman, and M. Stievenard. Climate and atmospheric history of the past 420,000 years from the Vostok ice core, Antarctica. *Nature*, 399(6735):429–436, 1999.
- C. Plate, R. Müller, A. Humbert, and D. Gross. Evaluation of the criticality of cracks in ice shelves using finite element simulations. *The Cryosphere Discuss.*, 6:469–503, 2012.
- D. Pollard and R. M. DeConto. Modelling West Antarctic ice sheet growth and collapse through the past five million years. *Nature*, 458(7236):329–332, 2009.

- A. Pralong and M. Funk. Dynamic damage model of crevasse opening and application to glacier calving. *Journal of Geophysical Research*, 110(B1):B01309, 2005.
- E. Rignot. Changes in ice dynamics and mass balance of the Antarctic ice sheet. *Philosophical Transactions of the Royal Society A: Mathematical, Physical and Engineering Sciences*, 364(1844):1637–1655, 2006.
- E. Rignot and S. S. Jacobs. Rapid bottom melting widespread near Antarctic ice sheet grounding lines. *Science*, 296(5575):2020, 2002.
- E. Rignot, D. G. Vaughan, M. Schmeltz, T. Dupont, and D. MacAyeal. Acceleration of Pine Island and Thwaites Glaciers, West Antarctica. *Annals of Glaciology*, 34(1):189–194, 2002.
- E. Rignot, J. Mouginot, and B. Scheuchl. Ice flow of the Antarctic ice sheet. *Science*, 333(6048):1427–1430, 2011a.
- E. Rignot, I. Velicogna, M. R. Van den Broeke, A. Monaghan, and J. Lenaerts. Acceleration of the contribution of the Greenland and Antarctic ice sheets to sea level rise. *Geophysical Research Letters*, 38(5):L05503, 2011b.
- C. Ritz, V. Rommelaere, and C. Dumas. Modeling the evolution of Antarctic ice sheet over the last 420,000 years: Implications for altitude changes in the Vostok region. *Journal of Geophysical Research*, 106(D23):31943–31964, 2001.
- H. Rott, W. Rack, P. Skvarca, and H. De Angelis. Northern Larsen ice shelf, Antarctica: further retreat after collapse. *Annals of Glaciology*, 34(1):277–282, 2002.
- F. Saito, A. Abe-Ouchi, and H. Blatter. Effects of first-order stress gradients in an ice sheet evaluated by a three-dimensional thermomechanical coupled model. *Annals of Glaciology*, 37(1):166–172, 2003.
- A. Salinger, K. J. Evans, J. F. Lemieux, D. Holland, T. Payne, S. Price, and D. Knoll. Implementation of the jacobian-free newton-krylov method for solving the for solving the first-order ice sheet momentum balance. *Journal of Computational Physics*, 230(17), 2011.
- T. A. Scambos, J. A. Bohlander, C. A. Shuman, P. Skvarca, et al. Glacier acceleration and thinning after ice shelf collapse in the Larsen B embayment, Antarctica. *Geophysical Research Letters*, 31, 2004.

- R. P. Scherer, A. Aldahan, S. Tulaczyk, G. Possnert, H. Engelhardt, and B. Kamb. Pleistocene collapse of the West Antarctic ice sheet. *Science*, 281(5373):82, 1998.
- C. Schoof. Ice sheet grounding line dynamics: Steady states, stability, and hysteresis. *Journal of Geophysical Research*, 112(F3):F03S28, 2007a.
- C. Schoof. Marine ice-sheet dynamics. Part 1. the case of rapid sliding. *Journal of Fluid Mechanics*, 573(1):27–55, 2007b.
- H. Seddik, R. Greve, T. Zwinger, and L. Placidi. A full Stokes ice flow model for the vicinity of Dome Fuji, Antarctica, with induced anisotropy and fabric evolution. *The Cryosphere*, 5(2):495–508, 2011. doi: 10.5194/tc-5-495-2011.
- H. Seddik, R. Greve, T. Zwinger, F. Gillet-Chaulet, and O. Gagliardini. Simulations of the Greenland ice sheet 100 years into the future with the full Stokes model Elmer/Ice. *Journal of Glaciology*, 58(209):427, 2012.
- N. M. Shapiro and M. H. Ritzwoller. Inferring surface heat flux distributions guided by a global seismic model: particular application to Antarctica. *Earth and Planetary Science Letters*, 223(1-2):213–224, 2004.
- S. Solomon, D. Qin, M. Manning, Z. Chen, M. Marquis, K. B. Averyt, M. Tignor, and H. L. Miller, editors. *Contribution of Working Group I to the Fourth Assessment Report of the Intergovernmental Panel on Climate Change, 2007*. Cambridge University Press, Cambridge, United Kingdom and New York, NY, USA, 2007.
- O. Soucek and Z. Martinec. Iterative improvement of the shallow-ice approximation. *Journal of Glaciology*, 54(188):812–822, 2008.
- S. Sugiyama, A. Bauder, P. Weiss, and M. Funk. Reversal of ice motion during the outburst of a glacier-dammed lake on gornergletscher, switzerland. *Journal of Glaciology*, 53(181):172–180, 2007.
- W. J. Van de Berg, M. R. Van den Broeke, C. H. Reijmer, and E. van Meijgaard. Reassessment of the Antarctic surface mass balance using calibrated output of a regional atmospheric climate model. *Journal of Geophysical Research*, 111(D11):D11104, 2006.
- M. van den Broeke. Strong surface melting preceded collapse of Antarctic Peninsula ice shelf. *Geophysical Research Letters*, 32(12):L12815, 2005.

- A. Vieli and A. J. Payne. Assessing the ability of numerical ice sheet models to simulate grounding line migration. *Journal of Geophysical Research*, 110:F01003, 2005.
- R. T. Walker, T. K. Dupont, B. R. Parizek, and R. B. Alley. Effects of basal-melting distribution on the retreat of ice-shelf grounding lines. *Geophysical Research Letters*, 35:L17503, 2008.
- J. Weertman. Stability of the junction of an ice sheet and an ice shelf. *Journal of Glaciology*, 13:3–13, 1994.
- J. Wen, Y. Wang, W. Wang, K. C. Jezek, H. Liu, and I. Allison. Basal melting and freezing under the Amery Ice Shelf, East Antarctica. *Journal of Glaciology*, 56(195):81–90, 2010.
- R. S. Williams, J. G. Ferrigno, and K. M. Foley. Coastal-change and glaciological maps of Antarctica. U.S. Geological Survey Fact Sheet 2005-3055, 2 p., 2005. URL <http://pubs.usgs.gov/fs/2005/3055>.
- T. Zwinger, R. Greve, O. Gagliardini, T. Shiraiwa, and M. Lylly. A full Stokes-flow thermo-mechanical model for firn and ice applied to the Gorshkov crater glacier, Kamchatka. *Annals of Glaciology*, 45(1):29–37, 2007.

Reference Papers

棚氷の縮小による南極氷床の流動変化

佐藤 建 (北海道大学大学院環境科学院), Ralf Greve (北海道大学低温科学研究所)

1. はじめに

近年の大気、海洋の温暖化による南極の棚氷が崩壊や、縮小が観測されている。このために棚氷が氷床を抑える効果が弱まり、上流部の氷の流出が促進されることが観測、理論の両面から示唆されている¹⁾。

棚氷と氷床の内陸部では流動メカニズムが大きく異なる。氷床内陸部では、底面の基盤との摩擦のため、鉛直シア応力が最も主要な応力である。一方、棚氷の底面は海洋であり底面摩擦が働かない。このため鉛直シア応力は無視できるほどで、水平方向の応力が主たる応力の成分となる。下部の底面摩擦がないために典型的な棚氷の流動速度は 1000 m/a であり、典型的な変動時間スケールは数百キロの大きな棚氷でも氷床内陸の 1/10 以下である。したがって棚氷は外部の環境変化に対して内陸部より速く反応する。

南極氷床の変動による将来の海水準変化への影響には大きな不確実性があり、その原因の一つが棚氷の変動によるものである。棚氷底面の融解量を変動させることで、棚氷の変動による氷床変動への影響を考察する。

2. 手法

本研究では氷床モデル SICOPOLIS に棚氷の流動モデルを結合させて氷床全体のシミュレーションを行った。熱力学結合氷床モデル SICOPOLIS²⁾はこれまでグリーンランド、南極、ローレンタイド氷床、火星の氷床等の様々な地域に適用されているが、棚氷への扱いがなされていなかった。筆者は棚氷の流動モデルを作成し、氷床モデルと結合してこれを南極氷床へと適用した。

筆者らは氷床による海面上昇を予測する国際プロジェクト SeaRISE に参画している。ここでは与えられた氷厚、地熱、涵養量、表面温度、棚氷-氷床分布を使用してシミュレーションを行った。モデルの水平分解能は 40km、鉛直方向は 90 層である。

棚氷底面の融解量については、海域により異なる扱いを行った。コントロール実験ではロス棚氷、ロンヌ棚氷、アメリー棚氷の融解量については、氷床との境界である接地線近辺では 2 m/a、それ以外の部分では 0.2m/a、深度 2000m 以下の外洋では 20m/a とした。陸氷に囲まれていない棚氷や南極半島の棚氷の領域では高い融解量が考えられるため、その 5 倍の融解量を設定した。次に海洋での融解量を 2 倍、5 倍、10 倍として融解量変動への鋭敏性を調べた。

3. 結果と考察

氷床の流動速度は図-1 のようになっており、棚氷や沿岸部で高い速度をもつこと、棚氷では沿岸部に向かってより速い速度を持つことが再現されている。次に棚氷の融解量変動実験を行った。棚氷の融解による内陸氷床の変動を見積るために海水準相当氷床変動を求めた。これにより、棚氷の融解による体積変化を除き、かつ将来の海

水準変化の影響を求める事ができる。実験の結果、融解量が大きいほど海水準相当の氷床体積が減少する効果を見積もることができた(図-2)。融解量を2倍とした実験と参照実験では500年間で海水準変動に70cm程度の差を引き起こす。参照実験と融解なしの場合でも同様である。また融解量5倍と10倍の差は500年間でも10cm程度である。これは融解量が5倍の状態でも十分に融解量が大きく、多くの棚氷が無くなり、融解量を上げても変動がないためだろう。

海洋温暖化の実験⁴⁾では21世紀後半でロンヌ棚氷下部における融解量が18m/aを超える事が示唆されており、温暖化に鋭敏な地域では数値実験で使用したような高い融解量を持つ可能性がある。一方ロス棚氷の融解量変動は大きくなく、海域による違いが重要になる。

4. 結論

海域による棚氷底部の融解量の差を考慮した氷床変動の数値実験を行った。融解量設定の変動により、海水準相当の氷床体積は100年で70cm、500年で2mとなった。底面での融解量の違いに対して、氷床鋭敏に変動する。今後は棚氷・氷床の面積変化を考える必要がある。

【参考・引用文献】

- 1) Rignot, E., (2006): Changes in ice dynamics and mass balance of the Antarctic ice sheet, Philosophical Transactions A, 364, 1844 1637-1655,
- 2) Greve, R., (1997): Application of a polythermal three-dimensional ice sheet model to the Greenland ice sheet: response to steady-state and transient climate scenarios. Journal of Climate, 10(5), 901-918,
- 3) Pollard, D. (2009): Response of the Antarctic Ice Sheet to increased ice-shelf oceanic melting, WAIS/FRISP Workshop, Washington, USA.
- 4) Hellmer,H.(2011): Will another ice shelf soon float in ‘hot’ water? International Glaciological Society Symposium on Interactions of Ice Sheets and Glaciers with the Ocean, La Jolla, USA.

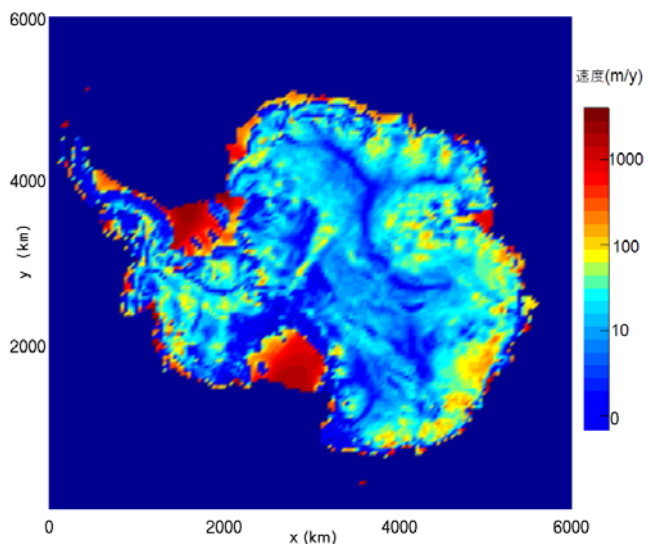


図-1. 南極氷床の速度分布の初期値

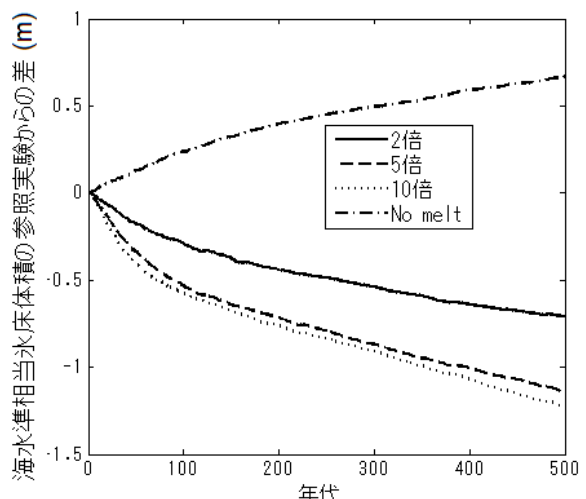


図-2. 融解量2倍, 5倍, 10倍, 融解なしの各実験の氷床体積変化の参考実験からの差

Sensitivity experiments for the Antarctic ice sheet with varied sub-ice-shelf melting rates

Tatsuru SATO,^{1,2} Ralf GREVE²

¹*Graduate School of Environmental Science, Hokkaido University,*

Kita-10, Nishi-5, Kita-ku, Sapporo 060-0810, Japan

²*Institute of Low Temperature Science, Hokkaido University,*

Kita-19, Nishi-8, Kita-ku, Sapporo 060-0819, Japan

ABSTRACT. Ice sheet modelling is an important tool for predicting the possible response of ice sheets to climate change in the past and future. An established ice sheet model is SICOPOLIS (SImulation COde for POLythermal Ice Sheets), and for this study the previously grounded-ice-only model was complemented by an ice shelf module. The new version of SICOPOLIS is applied to the Antarctic ice sheet, driven by standard forcings defined by the SeaRISE (Sea-level Response to Ice Sheet Evolution) community effort. A crucial point for simulations into the future is to obtain reasonable initial conditions by a paleoclimatic spin-up, which we carry out over 125,000 years from the Eemian until today. We then carry out a set of experiments for 500 years into the future, in which the surface temperature and precipitation are kept at their present-day distributions, while sub-ice-shelf melting rates between 0 and 200 m a^{-1} are applied. These simulations show a significant, but not catastrophic sensitivity of the ice sheet. Grounded ice volumes decrease with increasing melting rates, and the spread of the results from the zero to the maximum melting case is ~ 0.65 metres of sea level equivalent after 100 years and ~ 2.25 metres of sea level equivalent after 500 years.

1. INTRODUCTION

The Antarctic ice sheet is by far the largest land ice mass on the present-day Earth, and its volume amounts to approximatively 56.6 m SLE (metres of sea level equivalent) (Lemke and others, 2007). The current mass balance of the ice sheet is most likely

negative with an accelerating trend, even though the uncertainty is still significant (Lemke and others, 2007; Rignot and others, 2011; van den Broeke and others, 2011; Zwally and Giovinetto, 2011). Owing to the very low surface temperatures, the ice sheet is not very susceptible to surface melting even under moderate global warming scenarios. However, recent observations (e.g., Shepherd and others, 2001; Joughin and others, 2003; Rignot and others, 2004) have led to strong concerns that ice-dynamical processes (loss of buttressing from ice shelves, speed-up of ice streams and outlet glaciers) may boost the mass loss and thus lead to an additional contribution to sea level rise. The limited understanding of such processes was explicitly highlighted in the Fourth Assessment Report (AR4) of the United Nations Intergovernmental Panel on Climate Change (IPCC): “Dynamical processes related to ice flow not included in current models but suggested by recent observations could increase the vulnerability of the ice sheets to warming, increasing future sea level rise. Understanding of these processes is limited and there is no consensus on their magnitude.” (IPCC, 2007).

The scientific community has reacted to the need for an improved modelling of ice sheet dynamics, including their ice shelves, ice streams and outlet glaciers. Coordinated research projects have been launched, such as the European-led ice2sea programme funded by the European Union Framework-7 scheme (<http://www.ice2sea.eu/>), or the US-led SeaRISE effort (Sea-level Response to Ice Sheet Evolution; <http://tinyurl.com/srise-lanl>, <http://tinyurl.com/srise-umt>). The latter is an already well-advanced, community-organized effort to estimate the likely range of ice sheet contributions to sea level rise over the next few hundred years.

The Japanese ice sheet modelling community contributes to both ice2sea and SeaRISE as part of several funded research projects. In this study, we present results obtained with the model SICOPOLIS (SIimulation COde for POLythermal Ice Sheets) for the Antarctic ice sheet within the framework of the SeaRISE effort. To this end, SICOPOLIS was complemented by an ice-shelf module. We present a paleoclimatic spin-up that provides reasonable initial conditions for future climate runs. Based on that, we conduct a series of future climate scenarios specified by SeaRISE in which the climatic conditions at the ice surface are kept at their present-day conditions, but increased sub-ice-shelf melting as a consequence of increased ocean temperatures is assumed. The impact of these forcings on the mass balance of the ice sheet over the next 500 years is discussed.

48 2. ICE SHEET MODEL SICOPOLIS

SICOPOLIS simulates the large-scale dynamics and thermodynamics (ice extent, thickness, velocity, temperature, water content and age) of ice sheets three-dimensionally and as a function of time (Greve, 1997; for the latest version 3.0 used here see <http://sicopolis.greveweb.net/>). It is based on the shallow ice approximation (SIA) for grounded ice (Hutter, 1983; Morland, 1984), the shallow shelf approximation (SSA) for floating ice (Morland, 1987; MacAyeal, 1989; Weis and others, 1999) and the rheology of an incompressible, heat-conducting, power law fluid.

54 In this study, we use the regularized Glen flow law for the ice fluidity (inverse viscosity) $1/\eta$ in the form of Greve and Blatter
 55 (2009),

$$\frac{1}{\eta(T', \sigma_e)} = 2EA(T')f(\sigma_e), \quad (1)$$

56 where T' is the temperature relative to pressure melting¹, $A(T')$ the rate factor, $\sigma_e = \sqrt{\frac{1}{2} \text{tr}(\mathbf{t}^D)^2}$ the effective stress (square
 57 root of the second invariant of the deviatoric stress tensor \mathbf{t}^D), $f(\sigma_e)$ the creep function and E the flow enhancement factor.

58 The rate factor and creep function are expressed in the form of an Arrhenius law,

$$A(T') = A_0 e^{-Q/RT'} \quad (2)$$

59 (A_0 : pre-exponential constant, Q : activation energy, R : universal gas constant, T' in K), and a power law with additional
 60 constant term,

$$f(\sigma_e) = \sigma_e^{n-1} + \sigma_0^{n-1} \quad (3)$$

61 (n : stress exponent, σ_0 : residual stress), respectively. The values for the several parameters follow largely the recent recom-
 62 mendations by Cuffey and Paterson (2010) and are listed, among others, in Table 1.

63 A particular feature of the model thermodynamics is that it distinguishes between cold ice with a temperature below the
 64 pressure melting point and temperate ice with a temperature at the pressure melting point, the latter being considered as a
 65 binary mixture of ice and small amounts of water. In temperate ice, following Lliboutry and Duval (1985), the temperature-
 66 dependent rate factor $A(T')$ is replaced by a rate factor depending on the water content W ,

$$A_t(W) = A(T' = 0^\circ\text{C}) \times (1 + 1.8125 W[\%]). \quad (4)$$

67 The interface that separates cold and temperate ice is tracked through the use of Stefan-type energy flux and mass flux
 68 matching conditions (this procedure is referred to as the “polythermal mode”).

69 Basal sliding under grounded ice, v_b , is described by a Weertman-type sliding law with sub-melt sliding of the form applied
 70 to the Austfonna ice cap by Dunse and others (2011) (based on earlier work by, e.g., Weertman (1964), Lliboutry (1968),
 71 Bindschadler (1983), Hindmarsh and Le Meur (2001)),

$$v_b(T'_b) = -C_b e^{T'_b/\gamma} \frac{\tau_b^p}{N_b^q}, \quad (5)$$

72 where τ_b is the basal drag (shear stress), N_b the effective pressure and T'_b the basal temperature relative to pressure melting
 73 (in $^\circ\text{C}$, always $\leq 0^\circ\text{C}$). In the SIA, the effective pressure N_b is equal to the hydrostatic pressure $P_b = \rho g H$ (where ρ is the

¹More precisely, following Greve and Blatter (2009), $T' = T - T_m + T_0$, where T is the ice temperature (in either K or $^\circ\text{C}$), $T_m = T_0 - \beta p$ the pressure (p) dependent melting point and T_0 the melting temperature at standard atmospheric pressure (Table 1).

density of ice, g the gravitational acceleration and H the ice thickness) minus the water pressure P_w . The latter is assumed to be equal to the pressure of a sea water column of density ρ_{sw} and thickness $H_w = z_{sl} - b$, where z_{sl} is the mean sea level and b the ice base topography. This yields

$$N_b = P_b - P_w = \rho g H - \rho_{sw} g H_w. \quad (6)$$

In order to avoid the $N_b \rightarrow 0$ singularity when grounded ice becomes nearly floating close to the grounding line, N_b is constrained to be $\geq 0.2 \times P_b$. The basal drag τ_b is equal to the basal pressure times the surface slope,

$$\tau_b = \rho g H |\text{grad } h|, \quad (7)$$

where h is the surface elevation and grad the gradient operator in the horizontal plane (Greve and Blatter, 2009). The minus sign in Eq. (5) indicates that the direction of basal sliding is anti-parallel to the basal drag. The parameters have the values $C_b = 11.2 \text{ m a}^{-1} \text{ Pa}^{-1}$ (sliding coefficient), $p = 3$, $q = 2$ (sliding exponents) and $\gamma = 1^\circ\text{C}$ (sub-melt-sliding parameter).

Isostatic depression and rebound of the lithosphere due to changing ice load is modelled by the elastic lithosphere/relaxing asthenosphere (ELRA) approach (Le Meur and Huybrechts, 1996; Greve, 2001).

The shallow shelf module is a new feature of version 3.0 of SICOPOLIS. Its core is the solver for the non-linear elliptical differential equations for the horizontal velocities v_x and v_y (Greve and Blatter, 2009, Eq. (6.55); note that in the SSA v_x and v_y are constant over depth). This is done by discretizing the equations by central differences on the regular grid of SICOPOLIS, solving the resulting system of linear equations by the biconjugate gradient method with the Library of Iterative Solvers for Linear Systems (Lis, <http://www.ssisc.org/lis/>), and non-linear iterations between the horizontal velocities and the depth-integrated viscosity with a relaxation scheme. The position of the grounding line is determined by checking the floating condition,

$$\begin{aligned} H &\leq \frac{\rho_{sw}}{\rho} (z_{sl} - z_l) : \text{ floating ice,} \\ H &> \frac{\rho_{sw}}{\rho} (z_{sl} - z_l) : \text{ grounded ice} \end{aligned} \quad (8)$$

(where z_l is the topography of the lithosphere surface), and the inflow into regions of floating ice results from the SIA solution for the horizontal velocity field of adjacent grounded ice. A more sophisticated treatment of the sheet/shelf transition zone (e.g., Pollard and DeConto, 2007, 2009) will be implemented in future work. The calving front is exposed to the hydrostatic pressure of the adjacent sea water, and its position is determined by the simple, implicit calving criterion that floating ice calves if its thickness is smaller than a threshold value of 50 m. This is considerably thinner than the thickness of the major present-day Antarctic ice shelves; however, with a larger threshold of 200–250 m many of the smaller ice shelves (e.g., Riiser-Larsen, Shackleton) tend to erode during a simulation, and new ice shelves are largely prevented from forming. Sub-ice-shelf

98 melting, M , is parameterized by a method adopted from the GRISLI model (Ritz and others, 2001):

$$M = \begin{cases} M_{\text{gl}} & \text{in the vicinity of the grounding line (see below),} \\ M_{\text{cs}} & \text{over the continental shelf, } z_l > -1600 \text{ m,} \\ M_{\text{ao}} & \text{over the abyssal ocean, } z_l \leq -1600 \text{ m.} \end{cases} \quad (9)$$

99 For the three parameters, we use the standard values $M_{\text{gl}} = 2 \text{ m ice equiv. a}^{-1}$, $M_{\text{cs}} = 0.2 \text{ m ice equiv. a}^{-1}$ and $M_{\text{ao}} =$
100 $10 \text{ m ice equiv. a}^{-1}$. For M_{gl} and M_{cs} , this is 2/3 of the values suggested in GRISLI (A. Quiquet, personal communication
101 2010). The high value of M_{ao} prevents ice shelves from extending over the abyssal ocean, where they are unstable due to the
102 absence of embayments or islands/shoals that can serve as pinning points.

103 The model domain covers the entire area of Antarctica and the surrounding oceans, projected on a polar stereographic
104 grid with standard parallel 71°S and central meridian 0°E . Distortions due to this projection are accounted for as metric
105 coefficients in all model equations except for the above-mentioned SSA equations for the horizontal velocities. The present
106 geometry (surface and basal topographies, ice thickness, equilibrated bedrock elevation, grounded vs. floating ice) is derived
107 from the “Antarctica Developmental Data Set” (Antarctica_5km_dev1.0.nc) provided on the SeaRISE website, resampled to
108 a horizontal resolution of 20 km. In the vertical direction, sigma coordinates are used; the cold ice column, the temperate
109 ice layer (if present) and the thermal boundary layer of the lithosphere are mapped separately to $[0, 1]$ intervals. The cold
110 ice column is discretized by 81 grid points (concentrated towards the base), and the temperate ice and lithosphere layers are
111 discretized each by 11 equidistant grid points. Time steps are 0.05–0.5 a for the topography and velocity, and 0.25–2 a for the
112 thermodynamics.

113 The “vicinity of the grounding line” in Eq. (9) refers to floating-ice grid points that have a grounded-ice neighbour. In
114 addition, grounded-ice grid points with a floating-ice or ocean neighbour are assigned a basal melting rate M averaged over
115 the grid point itself and the four neighbours,

$$M = r_{\text{gr}} M_{\text{gr}} + (1 - r_{\text{gr}}) M_{\text{gl}} \quad (10)$$

116 where r_{gr} is the ratio of grounded-ice points among the five points ($r_{\text{gr}} = \#(\text{grounded-ice points})/5$) and M_{gr} is the computed
117 basal melting rate of the central grounded-ice point. Consequently, the “vicinity of the grounding line” (influence of the
118 prescribed parameter M_{gl}) extends over twice the horizontal resolution, that is, 40 km. Due to this rather large, resolution-
119 dependent zone of influence, we refrain from choosing a value of the order of tens of metres per year for M_{gl} , even though such
120 melting rates were measured near deep grounding lines (Rignot and Jacobs, 2002).

121 **3. SEARISE EXPERIMENTS**

122 **3.1. Paleoclimatic spin-up**

123 In order to obtain a suitable present-day configuration of the Antarctic ice sheet, it is desirable to carry out a paleoclimatic
 124 spin-up over at least a full glacial cycle. However, initial testing revealed that it is very difficult to reproduce the observed
 125 geometry (in particular the distribution of grounded vs. floating ice) by an unconstrained, freely evolving simulation. For this
 126 reason, we carry out the spin-up simulation in four steps:

127 (i) An initial relaxation run with freely evolving grounded ice topography over 100 a, starting from the present-day geometry
 128 and isothermal conditions at -10°C everywhere, in order to avoid spurious noise in the computed velocity field (Calov,
 129 1994). The grounding lines and floating ice topographies are kept fixed. The surface temperature and the sea level are
 130 those of today (see below), the surface mass balance is set to zero.

131 (ii) A steady-state run from 250 ka BP² until 125 ka BP with the entire topography kept fixed over time. The surface
 132 temperature is that of 125 ka BP, the surface mass balance is unspecified (due to the fixed topography).

133 (iii) A transient run from 125 ka BP until today with the entire topography kept fixed over time in order to enforce a good fit
 134 between the simulated and observed present-day topographies. The surface temperature varies over time (see below), the
 135 surface mass balance is unspecified.

136 (iv) A transient run over 20 a with unconstrained evolution of the ice topography in order to avoid transition shocks in the
 137 beginning of the subsequent future climate experiments. The climatic forcing (surface temperature, surface mass balance)
 138 and the sea level are kept steady at today's conditions.

139 Apart from the “frozen” geometry of the ice sheet in runs (ii) and (iii), the runs are conducted with the forcings suggested
 140 by SeaRISE. The mean annual and mean summer surface temperatures (T_{ma} and T_{ms} , respectively) are decomposed into
 141 present-day spatial distributions plus a purely time-dependent anomaly $\Delta T(t)$,

$$\begin{aligned} T_{\text{ma}}(h, \phi, t) &= T_{\text{ma}}^{\text{present}}(h, \phi) + \Delta T(t), \\ T_{\text{ms}}(h, \phi, t) &= T_{\text{ms}}^{\text{present}}(h, \phi) + \Delta T(t), \end{aligned} \quad (11)$$

²Here, the notation ka BP means thousand *calendar* years before present.

where t is time and ϕ geographical latitude. The present-day parameterizations are taken from Fortuin and Oerlemans (1990),

$$T_{\text{ma}} = \begin{cases} 7.405 - 0.014285 h - 0.180 \phi, & \text{for } h > 1500 \text{ m}, \\ 36.689 - 0.005102 h - 0.725 \phi, & \text{for } 200 \text{ m} < h \leq 1500 \text{ m}, \\ 49.642 - 0.943 \phi, & \text{for } h \leq 200 \text{ m}, \end{cases} \quad (12)$$

$$T_{\text{ms}} = 16.81 - 0.00692 h - 0.27937 \phi, \quad (13)$$

142 where temperatures are in $^{\circ}\text{C}$, surface elevations in m AMSL and latitudes in $^{\circ}\text{S}$ (counted positive). The time-dependent
 143 anomaly $\Delta T(t)$ results from the Vostok δD record converted to temperature with the relation by Petit and others (1999).

144 Precipitation, surface melting and sea level forcings are not required for runs (ii) and (iii) due to the “frozen” geometry
 145 approach. In fact, in these runs the net surface mass balance (precipitation minus surface melting) is *determined* by the
 146 dynamical ice flow via the continuity equation, as a consequence of requiring the geometry to be unchanged. For run (iv),
 147 precipitation is equated to the surface accumulation data by Arthern and others (2006), and surface melting is parameterized by
 148 Reeh’s (1991) positive degree day (PDD) method, supplemented by the semi-analytical solution for the PDD integral by Calov
 149 and Greve (2005). The PDD factors are (in ice equivalents) $\beta_{\text{ice}} = 8 \text{ mm d}^{-1} ^{\circ}\text{C}^{-1}$ for ice melt and $\beta_{\text{snow}} = 3 \text{ mm d}^{-1} ^{\circ}\text{C}^{-1}$ for
 150 snow melt (Ritz and others, 2001). Furthermore, the standard deviation of short-term, statistical air temperature fluctuations
 151 is $\sigma = 5 ^{\circ}\text{C}$, and the saturation factor for the formation of superimposed ice is chosen as $P_{\text{max}} = 0.6$ (Reeh, 1991).

152 As for the geothermal heat flux, the SeaRISE “Antarctica Developmental Data Set” provides two different distributions by
 153 Shapiro and Ritzwoller (2004) and Fox Maule and others (2005). We conduct the spin-up run with the one by Shapiro and
 154 Ritzwoller (2004), and, following a recommendation from the SeaRISE website, heat flux values are capped at 70 mW m^{-2} .

155 The simulated present-day configuration of the ice sheet (result of run (iv)) is used as initial condition for the future climate
 156 experiments described in the following.

157 3.2. Future climate experiments

158 For the future climate experiments, we use the following set of SeaRISE experiments:

159 Experiment CTL: Constant climate control run; beginning at present (more precisely, the epoch 2004-1-1 0:00, correspond-
 160 ing to $t = 0$) and running for 500 a holding the climate steady to the present climate. We carry out this run twice, with
 161 the surface accumulation data by (i) Arthern and others (2006) and (ii) van de Berg and others (2006) (both provided in
 162 the “Antarctica Developmental Data Set” by SeaRISE).

163 Experiment E1a: Constant climate forcing running for 500 a, surface accumulation by Arthern and others (2006), uniform
 164 sub-ice-shelf melting rate of $M_{\text{gl}} = M_{\text{cs}} = M_{\text{ao}} = 2 \text{ m ice equiv. a}^{-1}$ (instead of the parameters given after Eq. (9)).

165 Experiment E1b: Constant climate forcing running for 500 a, surface accumulation by Arthern and others (2006), uniform
 166 sub-ice-shelf melting rate of $M_{gl} = M_{cs} = M_{ao} = 20 \text{ m ice equiv. a}^{-1}$ (instead of the parameters given after Eq. (9)).

167 Experiment E1c: Constant climate forcing running for 500 a, surface accumulation by Arthern and others (2006), uniform
 168 sub-ice-shelf melting rate of $M_{gl} = M_{cs} = M_{ao} = 200 \text{ m ice equiv. a}^{-1}$ (instead of the parameters given after Eq. (9)).

169 Experiment E1z: Constant climate forcing running for 500 a, surface accumulation by Arthern and others (2006), zero
 170 sub-ice-shelf melting rate $M_{gl} = M_{cs} = M_{ao} = 0$ (instead of the parameters given after Eq. (9)).

171 For all experiments, surface melting is parameterized by the PDD method (see Sect. 3.1), basal melting at grounded-ice grid
 172 points with a floating-ice or ocean neighbour is computed by the averaging scheme of Eq. (10), and the geothermal heat flux
 173 is that by Shapiro and Ritzwoller (2004), capped at 70 mW m^{-2} (same as used for the paleoclimatic spin-up, see above).

174 The more recently defined “2011 Sensitivity Experiments” of the SeaRISE group, including investigations on changes of the
 175 climate at the upper surface and changes of sliding at the subglacial interface, will be considered in future work.

176 4. RESULTS AND DISCUSSION

177 The results of the paleoclimatic spin-up run (see Section 3.1) for the present are shown in Fig. 1. Due to the fixed-topography
 178 approach, the surface topography (Fig. 1a) is of course very similar to the observed one (not shown). Small differences of the
 179 order of tens of meters arise as a consequence of the initial 100-year relaxation and the final 20-year run with freely evolving
 180 topography. The surface velocity (Fig. 1b) shows the expected distribution with small velocities ($< 10 \text{ m a}^{-1}$) in the interior, a
 181 general speed-up towards the coast and the largest velocities of 1000 m a^{-1} and more for the ice shelves, while the limitations
 182 of our approach (20-km resolution, fixed-topography spin-up with short transient run at the end) do not allow capturing all
 183 fine structures adequately.

184 Basal temperatures (Fig. 1c) are at the pressure melting point in large areas in West Antarctica, while limited temperate
 185 base areas are found in East Antarctica in George V Land, Wilkes Land and several other places near the coast. At the deep
 186 ice core sites Vostok, Dome C, Dome F, Kohnen and Byrd, the spin-up run produces basal temperatures of -11.5°C , -11.6°C ,
 187 -18.5°C , -11.4°C and -2.0°C (pressure melting point), respectively. Except for Byrd, these temperatures are significantly
 188 below the pressure melting point, while the observed temperatures all reach the pressure melting point (Petit and others, 1999;
 189 Motoyama, 2007; Parrenin and others, 2007; Wilhelms and others, 2007).

190 This discrepancy is probably due to shortcomings of the applied geothermal heat flux distribution by Shapiro and Ritzwoller
 191 (2004), which gives values in the range of $45\text{--}50 \text{ mW m}^{-2}$ at Dome C, Dome F and Vostok. This is probably not sufficient
 192 to form a temperate base (Llubes and others, 2006, Fig. 3a). Seddik and others (2011) used a higher geothermal heat flux of

193 60 mW m⁻² to produce a realistic borehole temperature in the vicinity of Dome F. Therefore, larger geothermal heat fluxes
 194 would be needed to reproduce these observed melting conditions in East Antarctica. By contrast, the base of the West-Antarctic
 195 Byrd ice core, which receives a geothermal heat flux of 70 mW m⁻² in our simulation, reaches the melting point. A second
 196 possible reason for the underprediction of basal temperatures is the fixed-topography approach of the spin-up run. Compared
 197 to the real, evolving Antarctic ice sheet, our simplified approach certainly influences the englacial heat transport (by both
 198 advection and conduction) to some extent, which affects basal temperatures.

199 Figure 2 shows the evolution of the grounded ice volume for the future climate control run with the two different accumula-
 200 tion data mentioned in Section 3.2. In both cases, the ice volume increases by more than 1 m SLE over 500 years, and the
 201 accumulation data by van de Berg and others (2006) produce ~ 0.32 m SLE more ice than those by Arthern and others (2006).
 202 The reason is that the former accumulation rates are relatively larger than the latter, particularly around the margin of the ice
 203 sheet. By contrast, different geothermal flux settings [Shapiro and Ritzwoller (2004) vs. Fox Maule and others (2005)] cause
 204 only slight changes (not shown). In order to minimize the imbalance of the ice sheet in the future climate control run, we
 205 discard the accumulation data by van de Berg and others (2006) and use only those by Arthern and others (2006) for the future
 206 climate simulations with varied sub-ice-shelf melting rates (see Sect. 3.2). The imbalance for the initial time ($t = 0$ in Fig. 2,
 207 corresponding to the year 2004) is ~ 2.5 mm SLE a⁻¹, which indicates that the drainage of the ice sheet is underpredicted
 208 (probably related to the underpredicted basal temperatures, see above).

209 The results of the future climate simulations with varied sub-ice-shelf melting rates are shown in Figs. 3 and 4. As expected,
 210 the grounded ice volume (Fig. 3, shown relative to the control run because of the imbalance discussed above) becomes smaller
 211 when the basal melting rates are larger. However, the effect is strongly non-linear and diminishes with increasing melting
 212 rates. This agrees with the findings by Huybrechts and de Wolde (1999) for a similar series of simulations with smaller basal
 213 melting rates of 0, 1, 3, 5 and 10 m a⁻¹. The spread of ice volumes across all experiments (from the zero to the maximum
 214 melting case) is ~ 0.65 m SLE after 100 years and ~ 2.25 m SLE after 500 years. Excluding the most extreme experiment E1c
 215 with 200 m a⁻¹ basal melting and thus considering only the range from 0 to 20 m a⁻¹ yields a spread of ~ 2.0 m SLE after 500
 216 years. This agrees well with the spread of $\sim 0.6 \times 10^6$ km³ (~ 1.5 m SLE) reported by Huybrechts and de Wolde (1999) (their
 217 Fig. 14) for the range from 0 to 10 m a⁻¹. So we see a significant, but not catastrophic impact of increased basal melting on
 218 ice sheet decay.

219 Changes of the area of grounded and floating ice are shown in Fig. 4. In the control run (basal melting according to Eq. (9)),
 220 the grounded ice area drops by $\sim 0.25 \times 10^6$ km² ($\sim 2\%$) during the first 200 years, partly compensated by an increase of
 221 floating ice, and remains almost constant after that. In run E1a (2 m a⁻¹ basal melting everywhere), grounded ice evolves
 222 very similarly due to the identical melting rates in the vicinity of the grounding line, whereas two thirds of the floating ice

223 disappear over 500 years as a consequence of the 10 times larger melting rate over the continental shelf. In the more extreme
 224 runs E1b and E1c (20 and 200 m a^{-1} basal melting everywhere, respectively), today's floating ice disappears even stronger:
 225 For E1b most of it melts within 100 years, the remaining area stabilizing at $\sim 0.15 \times 10^6 \text{ km}^2$ ($\sim 10\%$ of today's value) due
 226 to a balance between inflow from the ice sheet and basal melting, and for E1c almost all floating ice disappears within a few
 227 years. This has a significant impact on the grounded ice area, which, for both E1b and E1c, shrinks continuously over the
 228 entire period of 500 years, by when the loss amounts to $\sim 0.5 \times 10^6 \text{ km}^2$ ($\sim 4\%$) relative to the control run.

229 In general, under the influence of high basal melting, the Ross and Antarctic Peninsula ice shelves decay faster than the
 230 Filchner-Rønne and Amery ice shelves. In the E1a experiment (2 m a^{-1} basal melting), the Ross ice shelf loses more than 50%
 231 of its area by $t = 250 \text{ a}$ and has almost disappeared by $t = 500 \text{ a}$, while the Amery ice shelf does not lose much of its area.
 232 The vulnerability of the Ross ice shelf results from the fact that it is surrounded by the Transantarctic Mountains, so that
 233 the incoming flux from the ice sheet is smaller than for other ice shelves. By contrast, the Amery ice shelf is largely stabilized
 234 against increased basal melting by the large inflow from Lambert Glacier, which is the world's largest glacier.

235 The grounded ice area is largest in run E1z (no basal melting), while the floating ice area is largest in the control run (basal
 236 melting according to Eq. (9)). This is related to grounding line migration. Since there is no basal melting in run E1z, the
 237 grounding lines can advance freely all around the ice sheet, so that the grounded ice grows at the expense of the floating ice. By
 238 contrast, basal melting favours grounding line retreat, so that in the control run floating ice grows at the expense of grounded
 239 ice. Even the floating ice area of run E1a (2 m a^{-1} basal melting) is larger than that of run E1z (no basal melting) during
 240 the first ~ 80 years. However, later the retreat of the calving fronts due to basal-melt-induced thinning outweighs this effect,
 241 so that finally the floating ice area of run E1a becomes smaller than that of run E1z. For runs E1b and E1c ($20 / 200 \text{ m a}^{-1}$
 242 basal melting) basal melting is so large that the loss due to thinning-induced calving rapidly overcompensates the gain due to
 243 grounding line retreat, and thus no initial increase of the floating ice area is observed in the results.

244 5. CONCLUSION

245 A module for floating ice was added to the dynamic/thermodynamic ice sheet model SICOPOLIS. We have applied the new
 246 version of the model to the Antarctic ice sheet and carried out a paleoclimatic spin-up as well as a set of future climate runs
 247 specified by the SeaRISE group. In the latter, the surface climate forcing was kept steady at present-day conditions, while
 248 the sub-ice-shelf melting rate was varied over a wide range. The simulations have revealed a significant, but not catastrophic
 249 sensitivity of the ice sheet, the grounded ice volume showing a spread from the zero to the maximum melting case of \sim
 250 0.65 m SLE after 100 years and $\sim 2.25 \text{ m SLE}$ after 500 years.

251 Some shortcomings of this study must be noted. Due to computing time limitations, we did the simulations of this study at
 252 a horizontal resolution of 20 km. This resolution does not resolve well many fine structures in the vicinity of ice streams that

are important for the dynamics of the ice sheet as a whole. It is thus desirable to improve the resolution to at least 10 km.
This is already on the way and will be the basis for the authors' contribution to the SeaRISE community effort (publication
in preparation). A second aspect is the current treatment of grounding line dynamics. As explained in Section 2, the inflow
into regions of floating ice results from the SIA solution for the horizontal flow field of adjacent grounded ice. A smoother way
of dealing with this change of flow regimes would be to consider a transitional zone with shelfy stream dynamics (SSA with
additional basal drag; MacAyeal (1989)). Following findings by Schoof (2007) and Pollard and DeConto (2009), for the rather
coarse resolutions typically applied in large-scale ice sheet models the inflow should be corrected by imposing a mass flux
constraint across the grounding line, which parameterizes ice velocities there as a function of local ice thickness and stresses.
Further, the simplified parameterization of basal melting (Eq. (9)) that does not distinguish between different regions and
types of ice shelves, as well as the calving criterion in the form of a simple threshold value for the ice thickness, leave room
for improvements. These points will be considered in future work.

ACKNOWLEDGEMENTS

We thank R.A. Bindschadler, S. Nowicki and others for their efforts in the management of the SeaRISE project, J.V. Johnson
and others for compiling and maintaining the SeaRISE datasets, A. Quiquet for information about the parameterization of
sub-ice-shelf melting in the model GRISLI, and D. Pollard for discussions about the grounding line treatment. Comments of
two anonymous reviewers and scientific editor D.M. Holland helped considerably to improve the manuscript. This study was
supported by a Grant-in-Aid for Scientific Research A (No. 22244058) from the Japan Society for the Promotion of Science
(JSPS).

REFERENCES

- Arthern, R. J., D. P. Winebrenner and D. G. Vaughan, 2006. Antarctic snow accumulation mapped using polarization of 4.3-cm wavelength
microwave emission, *J. Geophys. Res.*, **111**(D6), D06107.
- van de Berg, W. J., M. R. van den Broeke, C. H. Reijmer and E. van Meijgaard, 2006. Reassessment of the Antarctic surface mass balance
using calibrated output of a regional atmospheric climate model, *J. Geophys. Res.*, **111**(D11), D11104.
- Bindschadler, R., 1983. The importance of pressurized subglacial water in separation and sliding at the glacier bed, *J. Glaciol.*, **29**(101),
3–19.
- van den Broeke, M. R., J. Bamber, J. Lenaerts and E. Rignot, 2011. Ice sheets and sea level: Thinking outside the box, *Surv. Geophys.*,
32(4-5), 495–505.

- 280 Calov, R., 1994. Das thermomechanische Verhalten des Grönlandischen Eisschildes unter der Wirkung verschiedener Klimaszenarien –
281 Antworten eines theoretisch-numerischen Modells, Doctoral thesis, Department of Mechanics, Darmstadt University of Technology,
282 Germany.
- 283 Calov, R. and R. Greve, 2005. A semi-analytical solution for the positive degree-day model with stochastic temperature variations, *J.
284 Glaciol.*, **51**(172), 173–175.
- 285 Cuffey, K. M. and W. S. B. Paterson, 2010. The Physics of Glaciers, Elsevier, Amsterdam, The Netherlands etc., 4th ed.
- 286 Dunse, T., R. Greve, T. V. Schuler and J. O. Hagen, 2011. Permanent fast flow versus cyclic surge behaviour: numerical simulations of
287 the Austfonna ice cap, Svalbard, *J. Glaciol.*, **57**(202), 247–259.
- 288 Fortuin, J. P. F. and J. Oerlemans, 1990. Parameterization of the annual surface temperature and mass balance of Antarctica, *Ann.
289 Glaciol.*, **14**, 78–84.
- 290 Fox Maule, C., M. E. Purucker, N. Olsen and K. Mosegaard, 2005. Heat flux anomalies in Antarctica revealed by satellite magnetic data,
291 *Science*, **309**(5733), 464–467.
- 292 Greve, R., 1997. Application of a polythermal three-dimensional ice sheet model to the Greenland ice sheet: Response to steady-state
293 and transient climate scenarios, *J. Climate*, **10**(5), 901–918.
- 294 Greve, R., 2001. Glacial isostasy: Models for the response of the Earth to varying ice loads, Straughan, B., R. Greve, H. Ehrentraut and
295 Y. Wang, eds., Continuum Mechanics and Applications in Geophysics and the Environment, Springer, Berlin, Germany etc., 307–325.
- 296 Greve, R. and H. Blatter, 2009. Dynamics of Ice Sheets and Glaciers, Springer, Berlin, Germany etc.
- 297 Hindmarsh, R. C. A. and E. Le Meur, 2001. Dynamical processes involved in the retreat of marine ice sheets, *J. Glaciol.*, **47**(157),
298 271–282.
- 299 Hutter, K., 1983. Theoretical Glaciology; Material Science of Ice and the Mechanics of Glaciers and Ice Sheets, D. Reidel Publishing
300 Company, Dordrecht, The Netherlands.
- 301 Huybrechts, P. and J. de Wolde, 1999. The dynamic response of the Antarctic and Greenland ice sheets to multiple-century climatic
302 warming, *J. Climate*, **12**(8), 2169–2188.
- 303 IPCC, 2007. Summary for policymakers, Solomon, S., D. Qin, M. Manning, Z. Chen, M. Marquis, K. B. Averyt, M. Tignor and H. L.
304 Miller, eds., Climate Change 2007: The Physical Science Basis. Contribution of Working Group I to the Fourth Assessment Report of
305 the Intergovernmental Panel on Climate Change, Cambridge University Press, Cambridge, UK and New York, NY, USA, 1–18.
- 306 Joughin, I., E. Rignot, C. E. Rosanova, B. K. Lucchitta, J. Bohlander, J. L. Bamber and S. P. Gogenini, 2003. Timing of recent accelerations
307 of Pine Island Glacier, Antarctica, *Geophys. Res. Lett.*, **30**(13), 1706.
- 308 Le Meur, E. and P. Huybrechts, 1996. A comparison of different ways of dealing with isostasy: examples from modelling the Antarctic ice
309 sheet during the last glacial cycle, *Ann. Glaciol.*, **23**, 309–317.
- 310 Lemke, P., J. Ren, R. B. Alley, I. Allison, J. Carrasco, G. Flato, Y. Fujii, G. Kaser, P. Mote, R. H. Thomas and T. Zhang, 2007.
311 Observations: Changes in snow, ice and frozen ground, Solomon, S., D. Qin, M. Manning, Z. Chen, M. Marquis, K. B. Averyt,
312 M. Tignor and H. L. Miller, eds., Climate Change 2007: The Physical Science Basis. Contribution of Working Group I to the Fourth

- 313 Assessment Report of the Intergovernmental Panel on Climate Change, Cambridge University Press, Cambridge, UK, and New York,
314 NY, USA, 337–383.
- 315 Lliboutry, L., 1968. General theory of subglacial cavitation and sliding of temperate glaciers, *J. Glaciol.*, **7**(49), 21–58.
- 316 Lliboutry, L. and P. Duval, 1985. Various isotropic and anisotropic ices found in glaciers and polar ice caps and their corresponding
317 rheologies, *Ann. Geophys.*, **3**(2), 207–224.
- 318 Llubes, M., C. Lanseau and F. Rémy, 2006. Relations between basal condition, subglacial hydrological networks and geothermal flux in
319 Antarctica, *Earth Planet. Sci. Lett.*, **241**(3-4), 655–662.
- 320 MacAyeal, D. R., 1989. Large-scale ice flow over a viscous basal sediment: theory and application to ice stream B, Antarctica, *J. Geophys.
321 Res.*, **94**(B4), 4071–4087.
- 322 Morland, L. W., 1984. Thermomechanical balances of ice sheet flows, *Geophys. Astrophys. Fluid Dyn.*, **29**, 237–266.
- 323 Morland, L. W., 1987. Unconfined ice-shelf flow, van der Veen, C. J. and J. Oerlemans, eds., Dynamics of the West Antarctic Ice Sheet,
324 D. Reidel Publishing Company, Dordrecht, The Netherlands, 99–116.
- 325 Motoyama, H., 2007. The second deep ice coring project at Dome Fuji, Antarctica, *Sci. Drill.*, **5**, 41–43.
- 326 Parrenin, F., G. Dreyfus, G. Durand, S. Fujita, O. Gagliardini, F. Gillet, J. Jouzel, K. Kawamura, N. Lhomme, V. Masson-Delmotte,
327 C. Ritz, J. Schwander, H. Shoji, R. Uemura, O. Watanabe and N. Yoshida, 2007. 1-D-ice flow modelling at EPICA Dome C and Dome
328 Fuji, East Antarctica, *Clim. Past*, **3**(2), 243–259.
- 329 Petit, J. R., J. Jouzel, D. Raynaud, N. I. Barkov, J. M. Barnola, I. Basile, M. Bender, J. Chappellaz, M. Davis, G. Delaygue, M. Delmotte,
330 V. M. Kotlyakov, M. Legrand, V. Y. Lipenkov, C. Lorius, L. Pepin, C. Ritz, E. Saltzman and M. Stievenard, 1999. Climate and
331 atmospheric history of the past 420,000 years from the Vostok ice core, Antarctica, *Nature*, **399**(6735), 429–436.
- 332 Pollard, D. and R. M. DeConto, 2007. A coupled ice-sheet/ice-shelf/sediment model applied to a marine-margin flowline: forced and
333 unforced variations, Hambrey, M. J., P. Christoffersen, N. F. Glasser and B. Hubbard, eds., *Glacial Sedimentary Processes and
334 Products*, Blackwell Publ., International Association of Sedimentologists Special Publication No. 39, 37–52.
- 335 Pollard, D. and R. M. DeConto, 2009. Modelling West Antarctic ice sheet growth and collapse through the past five million years, *Nature*,
336 **458**(7236), 329–332.
- 337 Reeh, N., 1991. Parameterization of melt rate and surface temperature on the Greenland ice sheet, *Polarforsch.*, **59**(3), 113–128.
- 338 Rignot, E., G. Casassa, P. Gogineni, W. Krabill, A. Rivera and R. Thomas, 2004. Accelerated ice discharge from the Antarctic Peninsula
339 following the collapse of Larsen B ice shelf, *Geophys. Res. Lett.*, **31**(18), L18401.
- 340 Rignot, E. and S. S. Jacobs, 2002. Rapid bottom melting widespread near Antarctic ice sheet grounding lines, *Science*, **296**(5575),
341 2020–2023.
- 342 Rignot, E., I. Velicogna, M. R. van den Broeke, A. Monaghan and J. Lenaerts, 2011. Acceleration of the contribution of the Greenland
343 and Antarctic ice sheets to sea level rise, *Geophys. Res. Lett.*, **38**, L05503.
- 344 Ritz, C., V. Rommelaere and C. Dumas, 2001. Modeling the evolution of Antarctic ice sheet over the last 420,000 years: Implications for
345 altitude changes in the Vostok region, *J. Geophys. Res.*, **106**(D23), 31943–31964.

- 346 Schoof, C., 2007. Ice sheet grounding line dynamics: Steady states, stability, and hysteresis, *J. Geophys. Res.*, **112**(F3), F03S28.
- 347 Seddik, H., R. Greve, T. Zwinger and L. Placidi, 2011. A full Stokes ice flow model for the vicinity of Dome Fuji, Antarctica, with induced
348 anisotropy and fabric evolution, *The Cryosphere*, **5**(2), 495–508.
- 349 Shapiro, N. M. and M. H. Ritzwoller, 2004. Inferring surface heat flux distributions guided by a global seismic model: particular application
350 to Antarctica, *Earth Planet. Sci. Lett.*, **223**(1-2), 213–224.
- 351 Shepherd, A., D. J. Wingham, J. A. D. Mansley and H. F. J. Corr, 2001. Inland thinning of Pine Island Glacier, West Antarctica, *Science*,
352 **291**(5505), 862–864.
- 353 Weertman, J., 1964. The theory of glacier sliding, *J. Glaciol.*, **5**(39), 287–303.
- 354 Weis, M., R. Greve and K. Hutter, 1999. Theory of shallow ice shelves, *Cont. Mech. Thermodyn.*, **11**(1), 15–50.
- 355 Wilhelms, F., S. G. Sheldon, I. Hamann and S. Kipfstuhl, 2007. Implications for and findings from deep ice core drillings – an example: the
356 ultimate tensile strength of ice at high strain rates, Kuhs, W. F., ed., Physics and Chemistry of Ice, The Royal Society of Chemistry,
357 Cambridge, UK, Special Publication No. 311, 635–639.
- 358 Zwally, H. J. and M. B. Giovinetto, 2011. Overview and assessment of Antarctic ice-sheet mass balance estimates: 1992–2009, *Surv.
359 Geophys.*, **32**(4-5), 351–376.

Quantity	Value
Gravitational acceleration, g	9.81 m s^{-2}
Density of ice, ρ	910 kg m^{-3}
Density of sea water, ρ_{sw}	1028 kg m^{-3}
Power law exponent, n	3
Residual stress, σ_0	10 kPa
Pre-exponential constant, A_0	$2.847 \times 10^{-13} \text{ s}^{-1} \text{ Pa}^{-3}$ ($T' \leq -10^\circ\text{C}$) $2.356 \times 10^{-2} \text{ s}^{-1} \text{ Pa}^{-3}$ ($T' \geq -10^\circ\text{C}$)
Activation energy, Q	60 kJ mol^{-1} ($T' \leq -10^\circ\text{C}$) 115 kJ mol^{-1} ($T' \geq -10^\circ\text{C}$)
Flow enhancement factor, E	5 / 1*
Melting point at atmospheric pressure, T_0	$273.15 \text{ K} = 0^\circ\text{C}$
Heat conductivity of ice, κ	$9.828 e^{-0.0057 T[\text{K}]} \text{ W m}^{-1} \text{ K}^{-1}$
Specific heat of ice, c	$(146.3 + 7.253 T[\text{K}]) \text{ J kg}^{-1} \text{ K}^{-1}$
Latent heat of ice, L	335 kJ kg^{-1}
Clausius-Clapeyron gradient, β	$8.7 \times 10^{-4} \text{ K m}^{-1}$
Universal gas constant, R	$8.314 \text{ J mol}^{-1} \text{ K}^{-1}$
Isostatic time lag, τ_{iso}	3000 a
Asthenosphere density, ρ_a	3300 kg m^{-3}
Flexural stiffness of the lithosphere, K_1	10^{25} N m
Density × specific heat of the lithosphere, $\rho_r c_r$	$2000 \text{ kJ m}^{-3} \text{ K}^{-1}$
Heat conductivity of the lithosphere, κ_r	$3 \text{ W m}^{-1} \text{ K}^{-1}$
Thickness of the thermal boundary layer of the lithosphere, H_r	5 km

Table 1. Physical parameters used for the simulations of this study. *: $E = 5$ for grounded ice, $E = 1$ for floating ice.

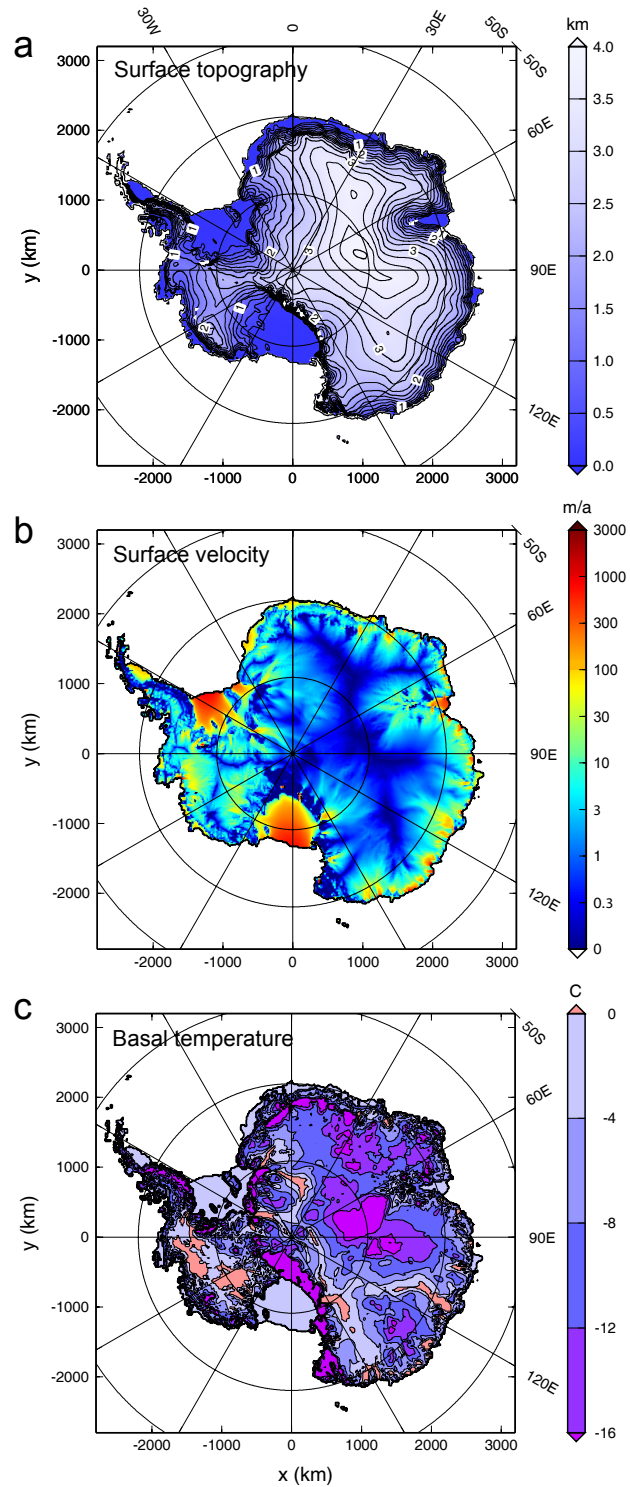


Fig. 1. Present-day configuration of the Antarctic ice sheet computed by the paleoclimatic spin-up. (a) Surface topography (in km AMSL, contour spacing is 250 m), (b) surface velocity (in m a^{-1}), (c) basal temperature (in $^{\circ}\text{C}$ relative to the pressure melting point).

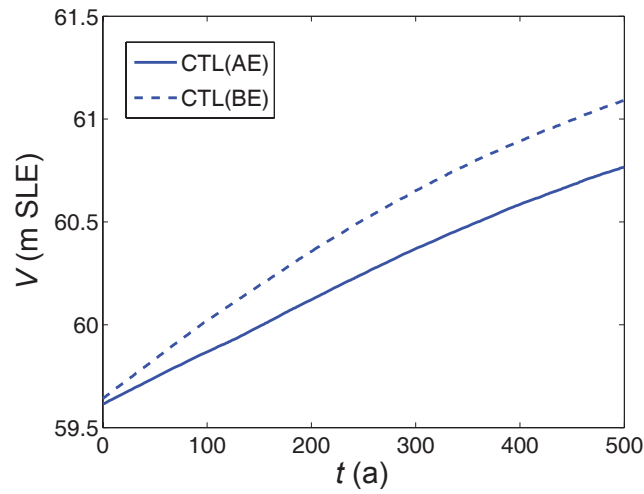


Fig. 2. Simulated grounded ice volume, V (expressed as SLE), for experiment CTL (constant climate control run), carried out alternatively with the surface accumulation data by Arthern and others (2006) (marked AE) and van de Berg and others (2006) (marked BE). Note that $t = 0$ corresponds to the year 2004.

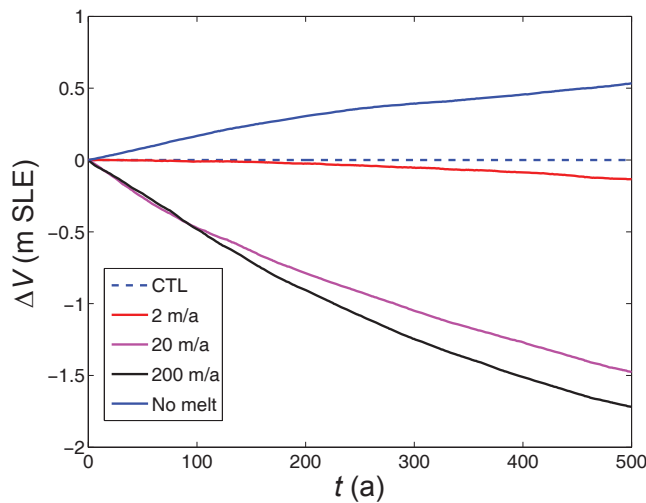


Fig. 3. Simulated changes in grounded ice volume, ΔV , relative to the control run CTL (expressed as SLE), for experiments E1a (constant climate, sub-ice-shelf melting $2 \text{ m ice equiv. a}^{-1}$), E1b (constant climate, sub-ice-shelf melting $20 \text{ m ice equiv. a}^{-1}$), E1c (constant climate, sub-ice-shelf melting $200 \text{ m ice equiv. a}^{-1}$) and E1z (constant climate, zero sub-ice-shelf melting). Surface accumulation by Arthern and others (2006). Note that $t = 0$ corresponds to the year 2004.

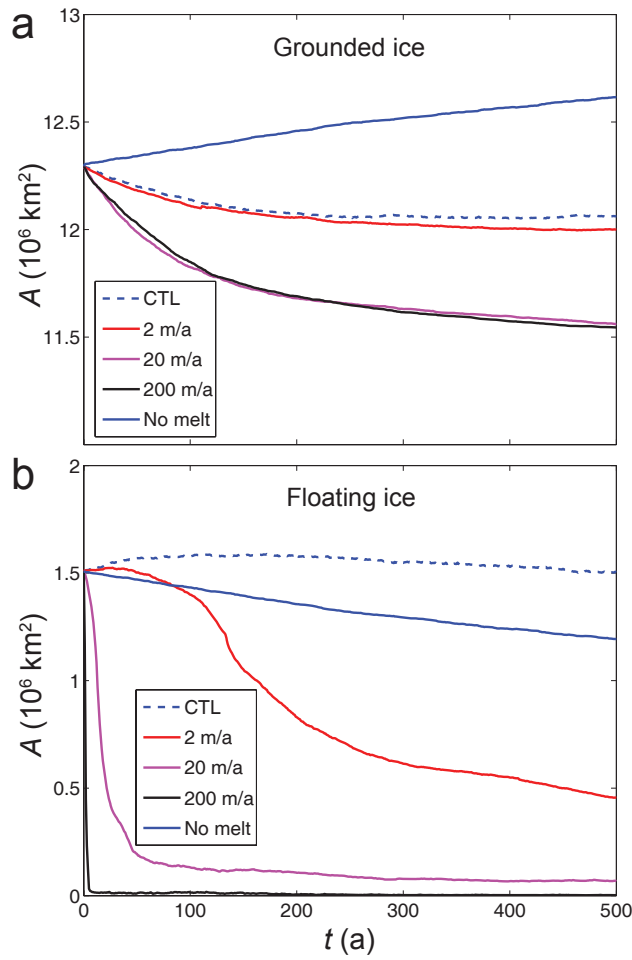


Fig. 4. Simulated ice area, A , for experiments E1a (constant climate, sub-ice-shelf melting $2 \text{ m ice equiv. a}^{-1}$), E1b (constant climate, sub-ice-shelf melting $20 \text{ m ice equiv. a}^{-1}$), E1c (constant climate, sub-ice-shelf melting $200 \text{ m ice equiv. a}^{-1}$) and E1z (constant climate, zero sub-ice-shelf melting). Panel (a): grounded ice area, panel (b): floating ice area. Note that $t = 0$ corresponds to the year 2004.

